Synthesis, characterization and physical properties of metal borides

Dissertation

zur Erlangung des Doktorgrades

des Fachbereichs Chemie

der Universität Hamburg

vorgelegt von Denis Fofanov

aus Russland

Hamburg

2006

Erklärung über frühere Promotionsversuche

Hiermit erkläre ich, *Folanov Denis* , dass vorher keine weiteren Promotionsversuche unternommen worden sind, oder an einer anderen Stelle vorgelegt wurden.

Hamburg, den 22. Juni   ....*Folanov*........
                                           - Unterschrift -

Eidesstattliche Versicherung

Hiermit erkläre ich an Eides Statt, dass die vorliegende Dissertationsschrift selbstständig und allein von mir unter den angegebenen Hilfsmitteln angefertigt wurde.

Hamburg, ...*Folanov*........
                                 - Unterschrift -

Kurzzusammenfassung

Im ersten Teil dieser Arbeit wurden die Hexaboride CaB_6 and SrB_6 untersucht. Die elektronischen Verhältnisse in bivalenten Hexaboriden sind bis heute nicht vollständig verstanden. Es wird jedoch angenommen, daß sich Bandlücke und Leitfähigkeit leicht von Konzentration und Art der Verunreinigungen beeinflussen lassen.

Hochreine Proben von CaB_6 und SrB_6 wurden hergestellt. Die Synthesen wurden mit Hilfe einer in der Arbeitsgruppe aufgebauten Metalldestillationsanlage optimiert. Die Hexaboride wurden charakterisiert.

Die Leitfähigkeit von CaB_6 wurde bei tiefen Temperaturen mittels Gleichstrom-Vierpunktkontaktmethode, bei hohen Temperaturen durch Niederfrequenzwechselstrom-Vierpunktkontaktmethode bestimmt. Für diese Messungen wurde die Meßanlage entworfen und aufgebaut. Alle untersuchten CaB_6-Proben zeigten halbleitendes Verhalten.

Die Verunreinigungen im Spurenmaßstab in den SrB_6-Proben wurden mit ICP-OES bestimmt. Nach Optimierung der Synthese konnten der Gewichtsanteil der Verunreinigungen (ohne Ca und Ba) auf 0,1 - 0,01 % gesenkt werden. Die elektrischen Eigenschaften von SrB_6 wurden mittels Hochtemperatur-Niederfrequenzwechselstrom-Vierpunktkontaktmethode untersucht. Sämtliche Proben erwiesen sich als Halbleiter, wobei die Größe der Bandlücke von Konzentration und Art der Verunreinigungen abhängig ist. Die Bandlücke von absolut reinem SrB_6 kann auf etwa 0,073 eV extrapoliert werden.

Im zweiten Teil wurden Nanoteilchen von Eisenboriden, die für potentielle Anwendungen in der Medizin und als magnetische Speichermaterialien besonders interessant sind, synthetisiert und charakterisiert. Nanoteilchen von Eisenboriden sind für potentielle Anwendungen in der Medizin und als magnetische Speichermaterialien besonders interessant.Auf verschiedenen Syntheserouten wurden unterschiedliche Arten von Nanoteilchen hergestellt:
- agglomerierte Eisenboride mit aktiver Oberfläche für Katalyseexperimente,
- amorphe, isolierte Eisenboridnanoteilchen mit Durchmessern von 5 bis 20 nm,
- kristalline, isolierte Eisenboridnanoteilchen mit Durchmessern von 3 bis 12 nm.
Die Proben wurden charakterisiert.

Alle Arten von Nanoteilchen erwiesen sich als luftempfindlich, wobei der Oxidationsprozeß für die isolierten Teilchen aufgrund der die Oberfläche bedeckenden Ligandenhülle wesentlich langsamer ablief.

Die magnetischen Eigenschaften kristalliner, oxidierter und nicht oxidierter Nanoteilchen verschiedener Durchmesser wurden untersucht. Abhängig von der Größe sind die Teilchen entweder superparamagnetisch oder ferromagnetisch. Nicht oxidierte Eisenboridnanoteilchen dürften gegenüber Eisenborat- oder Eisenoxidteilchen aufgrund höherer magnetischer Momente und „Blocking temperature" noch vielversprechender für mögliche Anwendungen sein. Oxidierte, bei Raumtemperatur superparamagnetische Nanoteilchen werden in der Medizin bereits angewandt.

Abstract

In the first part of this thesis, the hexaborides CaB_6 and SrB_6 were investigated. Till today, the electronic situation of divalent hexaborides is not properly understood. It is assumed, that these compounds are semiconductors with a small band gap, but with a conductivity behaviour easily affected by nature and concentration of impurities.

CaB_6 and SrB_6 samples of high purity were prepared. The synthesis was optimised using a metal distillation plant specifically constructed for this purpose. Both compounds were characterised. The conductivity of CaB_6 was studied at low temperatures by direct current four-point-probe method and at high temperatures by low-frequent alternating current four-point-probe method. For these measurements the instrument was constructed. All the investigated CaB_6 samples exhibited semiconducting behaviour.

The traces of impurities in SrB_6 samples were characterised using the ICP-OES method. After synthesis optimisation the amount of impurities (except Ca and Ba) was reduced to 0.1 - 0.01 weight percent. The electronic properties of SrB_6 were investigated by low-frequent alternating current four-point-probe method. All the samples show semiconducting behaviour, but the magnitude of band gap depends on the dopant state. The band gap of pure SrB_6 can be estimated to be about 0.073 eV.

In the second part nanoscale iron borides, which are interesting for magnetic storage and applications in medicine, were synthesised and characterised.

Using different synthesis routes, the following kinds of particles were obtained:

- agglomerated iron borides with free active surface, suitable for catalytic experiments,
- separate amorphous iron boride nanoparticles sized from 5 to 20 nm,
- separate crystalline iron boride nanoparticles sized from 3 to 12 nm.

The nanoparticles were characterized. All boride nanoparticles were found to be air-sensitive, in case of the separate nanoparticles the oxidation is slower due to a protecting shell of organic ligands on the surface remaining from synthesis.

The magnetic properties of crystalline nanoparticles both oxidised and not oxidised, were investigated. They were found to be either superparamagnetic or ferromagnetic, depending from size. The non-oxidised iron boride particles look much more perspective for possible technical applications than oxidised particles, i. e. iron borates, or even usually used iron oxides because of higher blocking temperatures and magnetic moments. The oxidised

particles are superparamagnetic at room temperature and could be applied in medicine where similar materials are already in use.

Abbreviation list

XRD	X-ray Diffraction
XPS	X-ray Photoelectron Spectroscopy
XAS	X-ray Absorption Spectroscopy
XANES	X-ray Absorption Near Edge Structure
EXAFS	Extended X-ray Absorption Fine Structure
TEM	Transmission Electron Microscopy
HRTEM	High Resolution Transmission Electron Microscopy
EELS	Electron Energy Loss Spectroscopy
SEM	Scanning Electron Microscopy
EDX	Energy Dispersive X-ray spectroscopy
SAED	Selected Area Electron Diffraction
IR	Infrared spectroscopy
TGA	Thermogravimetric Analysis
ESCA	Electron Spectroscopy for Chemical Analysis
UPS	Ultraviolet Photoelectron Spectroscopy
AES	Auger electron spectroscopy
HASYLAB	Hamburger Synchrotron Radiation Laboratory
DESY	Deutsches Synchrotron
LC	Least squares linear combination fitting
PCA	Principal component analysis
FT	Fourier transformation
AC	Alternative Current
DC	Direct Current
FLAPW	Full-potential Linearized Augmented Plane Wave
ICP-OES	Inductively-Coupled Plasma Optical Emission Spectrometry
LMTO	Linear Muffin-Tin Orbital
SRO	Short Range Order
TOP	trioctylphosphine
TOPO	trioctylphosphine oxide
HDA	hexadecylamine
THF	tetrahydrofuran
AOT	bis(2-ethylhexyl)sulfosuccinate

acac   acetylacetonate

AN   atomic number

EE   energy edge

CN   coordination number

RT   room temperature

Content

1 Introduction

1.1 Solid state chemistry of boron and borides

Boron is an interesting element owing to its particular properties. It is a challenge to practically working chemists as well as to theorists, technologists and material scientists. According to its place in the periodic table of elements, boron is the only non-metal of the third main group, and it shows similarities with the neighboring carbon and the diagonally adjoining silicon. The valence shell i.e. the 2s and 2p orbitals are occupied by three electrons. This lack of electrons is the reason for the particular and characteristic chemistry of boron. Boron was first synthesized by Davy in 1808 and also by Gay-Lussac and Thenard by reduction of borax [1]. Borax was already used in the ancient world for the production of glazes and glasses. The name "boron", which was introduced by Davy, is derived from borax, the source of boron and carbon, the most similar element known that time.

More reactive than most elements of the periodic system, boron forms a lot of compounds with almost all elements. By a cautious choice of different reaction partners and aimed synthesis, materials with a wide range of mechanical, thermal, chemical and electrical properties can be synthesized. The extremely hard and at the same time good thermal and electrical conductors TiB_2, ZrB_2 and CrB_2, as well as boron carbide $B_{13}C_2$, the third hardest material after diamond and cubic boron nitride, are only a few examples of this interesting group of compounds.

1.2 Hexaborides

The system of alkaline earth metals/boron has been investigated for more than a hundred years. Outstanding properties of these compounds are, for example: hardness, temperature stability, electrical conductivity, and its dependence on structural parameters. The precise nature of the electronic situation and its dependence of the concentration of impurities are not yet completely clear and hence still of great interest to solid state chemistry.

Moissan and Williams were the first, in 1897, to synthesize Ca, Sr and Ba borides, by thermite reduction of Ca, Sr and Ba borates in an electric arc [35]. Geelmuyden obtained CaB_6 by melting together of CaC_2 and B_2O_3 [36], Juengst and Mewes managed to synthesize it from $CaCl_2$ or CaF_2 and boron [37], Stock and Holle described a synthesis from Ca-metal and B_2O_3 [38]. Andrieux electrolyzed alkaline earth borate/fluoride melts as well

oxide/carbonate melts and observed a cathodic separation of boride. He was also the first, who had found that the chemical composition was MB_6 [39]. The crystal shape was already described as cubic by Moissan and Andrieux.

The first X-ray examinations were carried out by Allard on ThB_6 [40]. The Th-atoms have a cubic primitive structure. For the B-atoms besides the heavy Th-atoms it was impossible to determine the position. Finally, von Stackelberg and Neumann solved the crystal structures of CaB_6, SrB_6, BaB_6, LaB_6, CeB_6, PrB_6, NdB_6 and ErB_6 based on powder data [41]. First explorations of the conductivity were carried out on CaB_6 and CeB_6 and were verified later by Pauling and Weinbaum [42].

In order to obtain exact structure data it was necessary to grow single crystals of these substances. In 1974 Muranaka and Kawai succeeded to synthesize CaB_6 single crystals in an aluminum flux [43]. Ito and Higashi published data from investigations of CaB_6 single crystals with synchrotron radiation in 1993 [44]. Otani was able to obtain CaB_6 single crystals by pressing isostatic CaB_6 powder and heating it to 1700 ºC. The crystals thus obtained were purified via zone melting [45]. Ott et al. synthesized SrB_6 single crystals from SrB_6 crystalline powder in an aluminum flux and explored crystal structure, thermal and photo semiconductor properties and the electrical conductivity at low temperatures [46]. Calculated and experimental data about the thermodynamic properties of CaB_6 at a wide temperature range (198 - 673ºC) were published by Blinder et al. [47]. IR spectra of CaB_6 are available from Tsebulya et al. [48]. Theoretical investigations of the electronic situation for alkaline earth metal borides are available from the first works of Longuet-Higgins and de Roberts (1954) till and Massidda et al. (1997) [49 - 52].

The doping of alkaline earth metal borides with other elements is well known and reported, e.g. Naslain and Etourneau have synthesized $Na_xBa_{1-x}B_6$ [53], Nichols and Mar have introduced 20% Ca in ErB_6 single crystals [54], and Young et al. investigated $Ca_{1-x}La_xB_6$ [55]. The electronic situation of trivalent hexaborides, such as LaB_6 and YB_6, which are known as metallic conductors, is more or less understood, while that of divalent hexaborides is not clear. Theoretical and practical experiments [46-62] resulted in contradictions. For example CaB_6, SrB_6 and BaB_6 were described as semiconductors [49, 57, 60, 61, 62], metals [41] or semimetals [56].

1.3 Iron borides

In the context of their properties and applications, iron borides have been investigated quite thoroughly [72]. For example, the technology of doping steels and cast irons with boron relies on the formation of iron borides like FeB and Fe_2B because of their extreme hardness and chemical inertness. The wear and chemical resistance of the surface of tools is increased by transition metal borides, which are refractory and corrosion-resisting. Micro-alloying with ferro-boron is used to increase the hardenability of steel. In 1929, Bjurström and Arnfeld investigated the crystal structures of FeB and Fe_2B, obtained by high-temperature synthesis [73]. More recently, the ferromagnetism of iron borides has been investigated [74]. Amorphous Fe-B alloys are used as catalysts for many chemical reactions and have been found to be active and selective for the hydrogenation of olefins and organic functional groups. Also they can be used as ferrofluids and magnetic recording materials [66].
The reduction of metal ions with alkali metal borohydride has been used extensively for the production of fine powders of metals and metal borides. Furthermore, other works carried out for cobalt ions report the possibility to synthesize borate particles this way [66, 67].

1.3 Aims of investigation

It is particularly challenging for chemists to be able to influence and vary the properties of synthesized compounds by a suitable choice of starting materials and reaction conditions and to synthesize completely new materials with hitherto unknown interesting properties.
Our main interest is to obtain compounds of metals and boron (borides). In this work iron boride (in nanoscale size range) and bulk earth alkali metal borides were synthesized, characterized and investigated.
As mentioned above, the electronic situation of divalent hexaborides is not properly understood. The working hypothesis is that divalent hexaborides are semiconductors, with a conductivity behavior easily affectable by nature and concentrations of impurities.
The aim of this work is to synthesize CaB_6 and SrB_6 of a controllable purity/dopant status, to characterize them and investigate their conductivity properties as a function of nature and concentrations of impurities/dopants.
Separate magnetic nanoparticles are of interest because of their wide range of potential applications as high density magnetic recording media, ceramics, catalysts, drug delivery systems, ferrofluids, pigments in paints, and medical diagnostics [87, 88].

The project aims at synthesizing nanoscale iron borides in order to analyze their composition, structural and physical properties, in particular the magnetism, as well as the character of the particle surface and the influence of impurities.

2. Research methods and experimental equipment

2.1 Vacuum and inert gas equipment

2.1.1 Vacuum-argon line

Quite often, in inorganic chemistry, starting materials or products of a synthesis are instable in the presence of moisture or air. We therefore applied special equipment for working under argon atmosphere (Linde or Westfalia 4.6) or vacuum. This includes a vacuum-argon line, Schlenk-tubes and a glove-box.

The vacuum-argon line was made of duran glass in the glass-blowers' workshop of the Chemical Institutes at University of Hamburg and is shown in Fig. 2.1.1.1 [3]
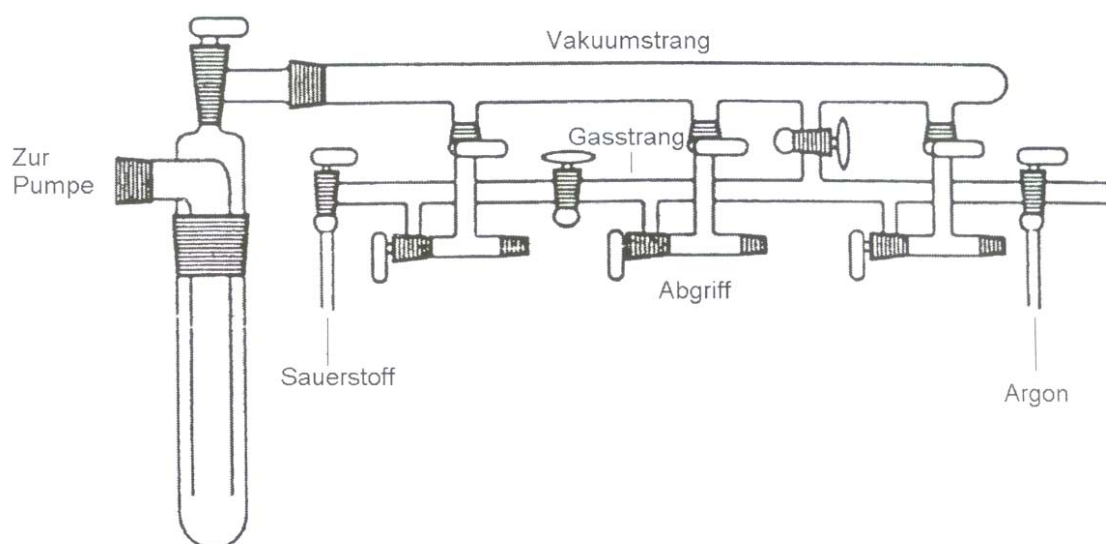
Fig. 2.1.1.1 Vacuum-argon line [3]

It is built firmly on the working place and consists of vacuum and argon parts which are connected to three distributors. Via these distributors the working vessels (schlenk-tubes, pour-tubes, etc.) can be connected to the vacuum-argon line and either evacuated or flooded with argon.

Between the Schlenk-tubes and the vacuum-argon line distributors, glass spirals were inserted in order to facilitate snatching and surging while working with them.

To prevent air penetration into the vacuum-argon line, an argon counter flow was applied at any open connection of the line or the Schlenk-tube.

The argon was purified by passing it through blue gel, potassium hydroxide, a molecular sieve (3 angstrom), and phosphorus pentoxide (Merck, Darmstadt) in order to remove any traces of water. After that it was passed over a quartz tube filled with a titanium sponge (Deutsche Titan GmbH, Essen), which was kept at a constant temperature of 700 °C in a tube oven, in order to remove any traces of oxygen and nitrogen.

The vacuum line is connected to a vacuum pump (Type RV3, Edwards, suction property 3.3 m^3h^{-1}) via a metal bellows tube and a liquid nitrogen trap . Vacuum of 10^{-3} mbar could be achieved. The vacuum is measured with an ionization-warm cathode-vacuum meter (Pirani). The glass contacts are sealed with vacuum ramsay-grease (Leybold, Köln). Compared with a glove-box, the vacuum-argon line provides noticeably better inert gas conditions, due to the argon purification. All work where is required to work under protective gas should whenever possible be carried out using the vacuum-argon line.

2.1.2 Schlenk-tubes and pour-tubes

Examples of schlenk-tubes and pour-tubes are demonstrated in Fig. 2.1.2.1 [3].

Fig. 2.1.2.1 a) schlenk-tube b) pour-tube [3]

Both were made from duran-glass in the glass-blowers' workshop mentioned above.
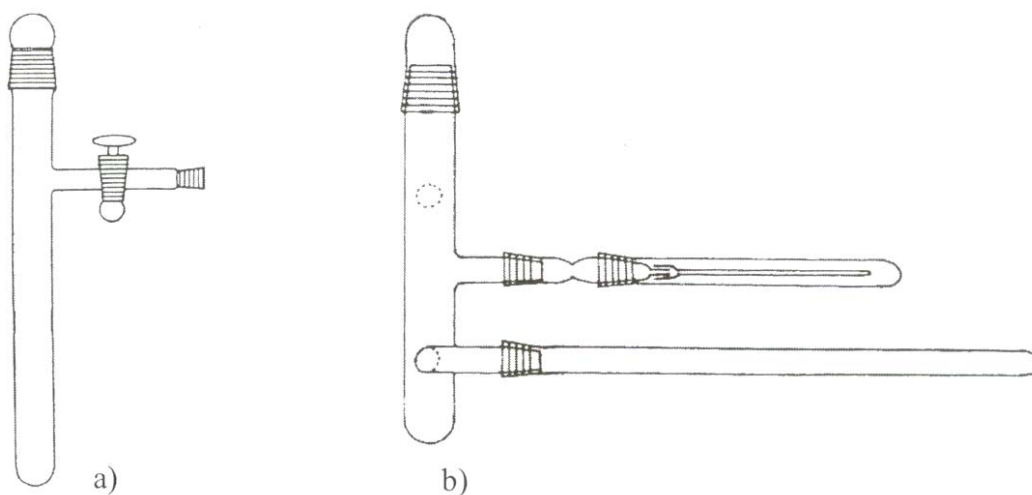The schlenk-tubes serve to keep substances under argon atmosphere. They could also be used for drying substances (e.g. boron powder) at a maximum temperature of 550 °C.
They consist of a tube closed at one end (about 200 mm long, 30 mm internal diameter)

with an NS 29 grinding and a suitable grinding cap, an offshoot (angle to the main tube 90°) with a valve and NS 14.5 grinding which can be connected to the vacuum-argon line.

With the help of the pour-tube, samples can be ground and welded in portions in duran glass ampoules (offshoot below) and filled into a Mark-capillary (offshoot above, a special Mark-capillary article is required).

The pour-tube consists of a tube closed at one end (about 200 mm long, 30 mm internal diameter) with an NS 29 grinding and a suitable grinding cap, two offshoots with NS 14.5 grindings, at an angle of 90° to the main tube, and with an angle of 20° between them, one more offshoot serves to connect it to the vacuum-argon line.

2.2 Ovens and crucibles

Solid state reactions at temperatures below 1050 ° C can be carried out in electric resistance ovens with kanthal wire winding, which were built in the technical workshops of the Chemical Institutes at University of Giessen.

For reactions up to 1450 ° C there was a silicium carbide resistance oven. A gas-tight corundum internal tube can be driven in and out of the oven with the help of a special rail system. It is connected to the vacuum-argon line by way of a metal flange and sealed with vacuum rubber rings.

For some solid state reactions at high temperatures and with strongly corrosive educts special crucible materials and working methods are required. The materials which were used are listed in table 2.2.1 [3].

Crucible material	Crucible size
Iron tube, closed welded at one end, carbon poor iron STG1, carbon<0.01 %	Length: 100 mm External diameter: 12 mm Internal diameter: 8 mm Thickness of walls: 1mm
Tantalum tube, closed welded at one end, ASTM-B-521-92, Plansee	Length: 100 mm External diameter: 10 mm Internal diameter: 8 mm Thickness of walls: 1mm

Table 2.2.1 Crucible materials [3]

The iron crucibles were made in the technical workshop of Chemical Institutes of University of Hamburg.

The tantalum crucibles were cut from the tantalum tubes, then one end was tightly pressed in a grip vice and welded with arc welding. Than tantalum crucibles were cleaned with an acid mixture (three parts concentrated HF, two parts concentrated HNO_3 and one part H_2SO_4), then with distilled water, and vacuum dried. Before synthesis, the tantalum crucibles were filled with boron and heated in high vacuum overnight at 1000 °C. The result is a protective coating of tantalum tubes by tantalum borides without which impurities of tantalum borides (mainly TaB_2) are possible.

Then the metal crucibles were filled with starting materials in the glove-box, closed tightly again with the grip vice, and immediately after the glove-box welded hermetically with arc welding. After that the crucibles were melted in quartz ampoules under vacuum at the vacuum-argon line. A quartz tube (external diameter: 20 mm, internal diameter: 18 mm) is closed by welding at one end with an oxygen-hydrogen burner (Arnold, Weilburg). A metal crucible is placed in it, at the other end a quickfit nozzle (a tube closed at one end with an offshoot for connection to the vacuum-argon line and a threading with ring-seal for connecting to a quartz tube) is fitted, and the whole system is connected to the vacuum-argon line. The quartz ampoule is welded in vacuum an earth gas burner. The procedure is needed to avoid crucible material oxidation at the high reaction temperatures.

2.3 Arc melting

Arc melting is a common procedure when reaction temperatures higher than 1500 °C are needed.

In industry this method is used for the synthesis of permanent magnets, intermetallic compounds (e.g. $SmCo_5$ or Sm_2Co_{17}), calcium carbide from lime and coke under 2000-2200 °C, to produce phosphor from calcium phosphate through reduction with coke at 1400 °C or to synthesize high melting hard materials such as boron carbide and borides of transition metals directly from the elements under a protective gas atmosphere.

In laboratory conditions, arc melting with a water-cooled copper crucible can be used to synthesize low melting germanides and stannides (ScAuGe [6] and Er_2Au_2Sn [7]) or high melting binary carbides (YC_2 [8]), phase pure, in amounts of about one gram, from the elements.

The educts are carefully ground together and pressed with a hydraulic press; then a pellet is put in an arc melting device connected to the vacuum-argon line (Fig. 2.3.1 [5]).
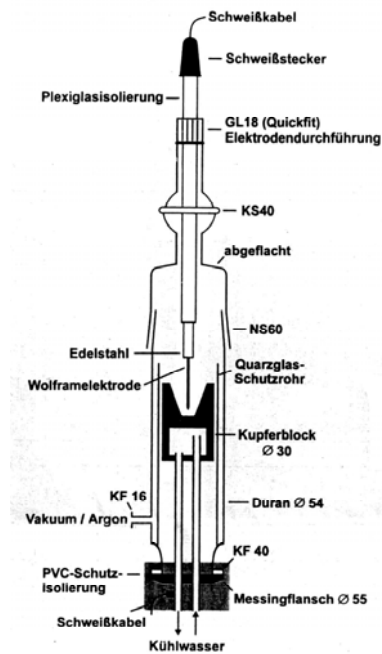
Fig. 2.3.1 Arc melting device with water cooling for melting substances [5]

The sample is evacuated, and the melting under argon atmosphere (under reduced pressure) can take place. Alternating voltage is applied between a tungsten needle and the copper crucible which holds a sample. An electrical transformer provides the voltage. During the melting there should not be any direct contact between the tungsten needle and the sample, otherwise tungsten impurities could appear in the sample or the tungsten needle could be damaged.

2.4 X-ray Powder Diffraction

2.4.1 Radiation

X-rays are electromagnetic radiation of a wavelength around 1 Å. They are usually produced via an interaction of high energy charged particles, e. g. electrons accelerated through 30 kV, with solid matter. The electrons are excited to strike a metal cathode. They are slowed down or stopped upon collision and some of their lost energy is converted to electromagnetic radiation (white radiation). But some of the incident electrons ionize the metal 1s (K shell) electrons. An outer (2p or 3p) electron immediately falls into the vacant 1s orbital by losing energy and the energy difference between these levels appears as X-radiation. The transition 2p→1s is called Kα, 3p→1s Kβ. Kα is actually consisting of a doublet, $K\alpha_1$ and $K\alpha_2$, because the energy of the two possible spin states of 2p electrons is slightly different from the spin of the vacant 1s state. As a rule, Kα transition happens much more frequently than the Kβ one, and it is the more intense Kα radiation which is used in diffraction experiments. A general X-ray metal emission spectrum is shown in Fig. 2.4.1.1 [9].
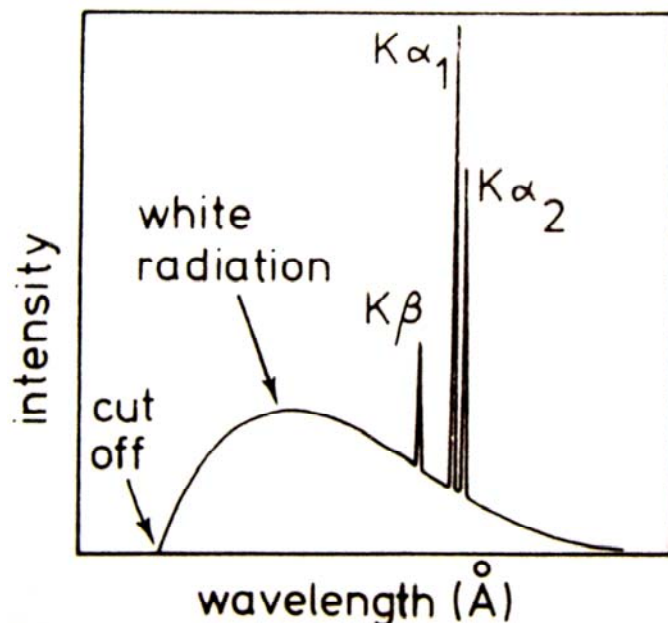

Fig. 2.4.1.1 X-ray emission spectrum of a metal (e.g. copper) [9]

For diffraction experiments a monochromatic beam is needed (Kα only). The elements with an atomic number one less than the atomic number of cathode element effectively absorb Kβ radiation allowing Kα radiation to go through. The separation of $K\alpha_1$ and $K\alpha_2$ is possible

only when using a monochromator (crystals). Table 2.4.1.1 gives the wavelengths of the $K\alpha_1$ lines commonly used for X-ray generation and materials suitable for filters.

Cathode	$K\alpha_1$, Å	Filter
Cr	2.2896	V
Fe	1.9360	Mn
Co	1.7889	Fe
Cu	1.5405	Ni
Mo	0.7093	Nb
Ag	0.5594	Pd

Table 2.4.1.1 X-ray wavelengths of commonly used cathode materials [9]

When an element is able to absorb the intensive $K\alpha$ radiation, it becomes a source of a second kind of radiation: fluorescence. This happens when the wavelength corresponding to the ionization potential of 1s electrons is longer than the wavelength of the primary beam. For example, for Cu $K\alpha$ radiation this is the case for Co and Fe. It is not recommended to measure samples with a big content of cobalt and iron using Cu cathode X-rays.

2.4.2 Measurement principle

If the wavelength of the X-ray radiation and of the ionization potentials of the irradiated elements differ distinctly, the interaction of the x-ray beam with atoms can be regarded as an interaction with solid spheres. The nearest approximation would be to consider atom layers in a crystal as partially transparent mirrors. Part of the X-rays are reflected at an angle of reflection equal to the angle of incidence, the rest are transmitted to be reflected by the next plane. The derivation of Bragg's Law is shown in Fig. 2.4.2.1 [9]. Two X-rays, 1 and 2, are reflected from planes A and B within the crystal. Beam 22' has to go the extra distance xyz as compared with beam 11', and for 1' and 2' to be in phase, xyz must equal a whole number of wavelengths.

$$xy=yz=d \sin \theta$$
$$xyz=2d \sin \theta=n\lambda$$
$$2d \sin \theta=n\lambda$$

When Bragg's Law is satisfied the reflected beams are in phase and interfere constructively, otherwise destructive interference occurs.
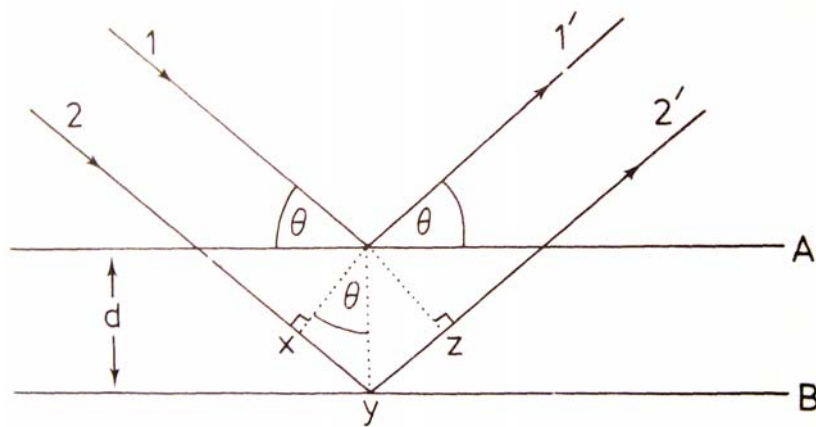

Fig. 2.4.2.1 Derivation of Bragg's Law for X-ray diffraction [9]

Nowadays, usually crystal monochromators are used instead of filters in order to obtain highly monochromatic radiation and to produce an intense, convergent X-ray beam.
A crystal monochromator consists of a large single crystal of, for example, quartz, oriented in such a way that one set of planes which diffracts strongly (1, 0, -1,1 for quartz) is at the Bragg angle to the incident beam. This Bragg angle is calculated for wavelength $K\alpha_1$ and so only $K\alpha_1$ rays are diffracted, giving monochromatic radiation.
In the powder method, a monochromatic beam of X-rays after monochromator strikes a powdered sample that, ideally, has crystals randomly arranged in every possible orientation. Usually, to ensure this, the powder sample is rotated. In such a sample, various lattice planes are also present in every possible orientation. For each set of planes, therefore, there exist some crystals which are oriented at the Bragg angle to the incident beam and these crystals are diffracted. The possible arrangement of a measurement (Guinier principle) is shown in Fig. 2.4.2.2 [12]. The diffracted beams can be detected using a movable detector connected to a digital recorder (diffractometer).
Ways to increase the quality of the diffraction pattern are to decrease the step size (resolution) and to increase the measurement time pro measurement point (signal/noise ratio). Madsen and Hill [10], however, found that after a certain point further decreasing the step size and increasing the measurement time pro measurement point does not improve the quality of the diffraction pattern.
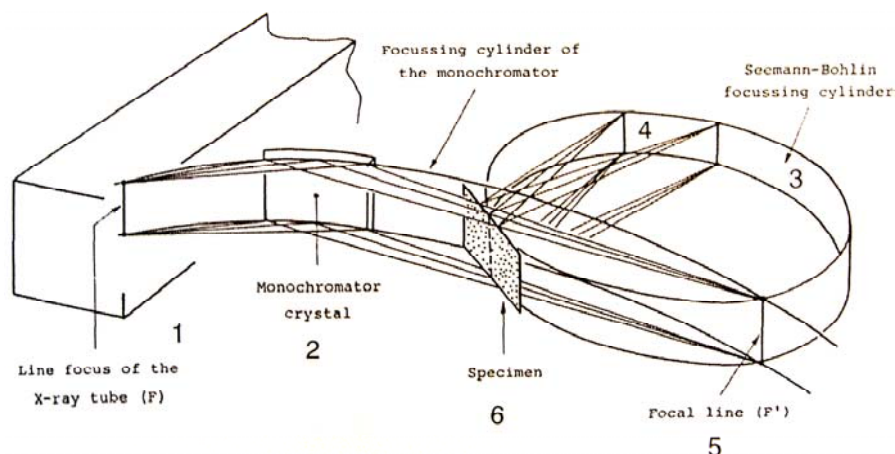
Fig. 2.4.2.2 Guinier measurement principle [12]

Modern powder diffractometers are microprocessor controlled programmed devices which can store measured data digitally. Measured data can be processed on a computer with a number of different programs (here used "STOE WinXPoW", 1.10, STOE & Cie GmbH).

2.4.3 Phase analysis

The powder pattern is defined manly by two parameters: the angular position of the reflections and their intensities. These are determined by size and shape of the unit cell, and atomic number and position of the various atoms in the cell. So if materials have the same crystal structure, their powder patterns can differ in the diffraction angles of reflections due to variations of the unit call extent for different sized elements, and in intensities due to different scattering powers for different elements.

While the reflection positions are fixed and characteristic of each measured sample, the intensities can vary a little from one sample to another, depending on the sample preparation and device conditions. For the identification of a given sample, the reflection positions are more important than the intensities which can be considered as secondary. So for a substance the diffraction pattern can be used as a fingerprint. The measured pattern can be compared to standard patterns, which are given in the Powder Diffraction File (known also as the PDF). The data base contains both inorganic and organic compounds, which are indexed either by the Hanawalt index (which uses the eight most intense reflections) or by the Fink index (which uses the first eight reflections).

Naturally, a mixture of substances can be identified also, if patterns of the component phases are available for comparison.

The X-ray powder method can also be used as a rough test of sample purity, if impurities are present as separate crystalline phases. The limit of impurities detectable that can be detected is in the region of 1 to 5 per cent. When looking for a specific impurity (measuring the specific short range) the detection limit can be decreased considerably by increasing the sensitivity (decreasing the step size (resolution) and increasing the measurement time pro measurement point (signal/noise ratio)).

After identification, the amount of several crystalline phases in a mixture may be determined by a simple method for "quantitative" X-ray powder diffraction. The internal standard (well crystallized phase) is added to the sample in a strictly controlled amount (for example, 10 weight per cent). The sample is measured again, the procedure is repeated, and so a calibration graph of intensity against composition is constructed. Then the reflection of the phase of interest is selected and its intensity is compared with that of a suitable internal standard reflection. The amount can be calculated by interpolation from the previously made calibration graph.

This method has a lot of further useful applications, such as:

- determination of accurate unit cell parameters
- investigation of solid solution lattice parameters
- crystal structure determination
- particle size measurements,

which were not used in this work.

2.4.4 Experimental

In this work, samples were measured at a powder diffractometer with Debye-Scherrer geometry (Stoe, Stadi P, Cu radiation, Ge monochromator, PSD) and at a powder diffractometer with reflection geometry (Philips, PW 1050/25, Co radiation, Fe filter, scintillation counter).

2.5 X-ray Photoelectron Spectroscopy (XPS)

2.5.1 Photoelectron Spectroscopy

Electron spectroscopy methods measure the kinetic energy of electrons that are emitted from a sample after bombardment with high-energy particles or radiation. Electron Energy Loss Spectroscopy (EELS) will be considered in chapter 6, we are here considering another kind of electron spectroscopy, XPS (X-ray Photoelectron Spectroscopy). XPS is also known as ESCA (Electron Spectroscopy for Chemical Analysis), but under this name it includes UPS (Ultraviolet Photoelectron Spectroscopy).

XPS is a very useful semi-quantitative technique that was developed by Siegbahn and coworkers in Uppsala (1967). He was awarded the Nobel Prize for Physics for his work in 1981.

In a first step it is necessary to prepare the sample. The size may vary from a few millimeters to a few centimeters, depending partly on the instrument but mainly on the technology being used.

The sample is then set in the first chamber (sample preparation chamber). This chamber is then pumped by high vacuum pumps (also called secondary vacuum pumps) down to a vacuum below 10^{-7} mbar. When the proper vacuum has been achieved, the sample is transferred into the analysis chamber and the XPS experiment may begin. The analysis chamber vacuum ranges from 10^{-8} mbar to 10^{-11} mbar.

The ionizing X-ray is either Mg Kα, 1254 eV or Al Kα, 1487 eV. During ionization various processes take place [13].

The simplest one is ionization of electrons. The energy of incident radiation hν is the sum of a kinetic energy and a binding energy or ionization potential.

$$h\nu = E_{\text{Kinetic}} + E_{\text{Binding}}$$

where

hν: X-ray beam incident energy

E_{Kinetic}: kinetic energy of the electron when leaving the specimen

E_{Binding}: binding energy of the electron inside the atom

An electron carrying enough energy can leave the material. In order to determine its binding energy within the matter we must first measure its kinetic energy when it has left the matter. A lens system focuses the electron beam into a hemispherical analyzer (Fig. 2.5.1.1 [14]).
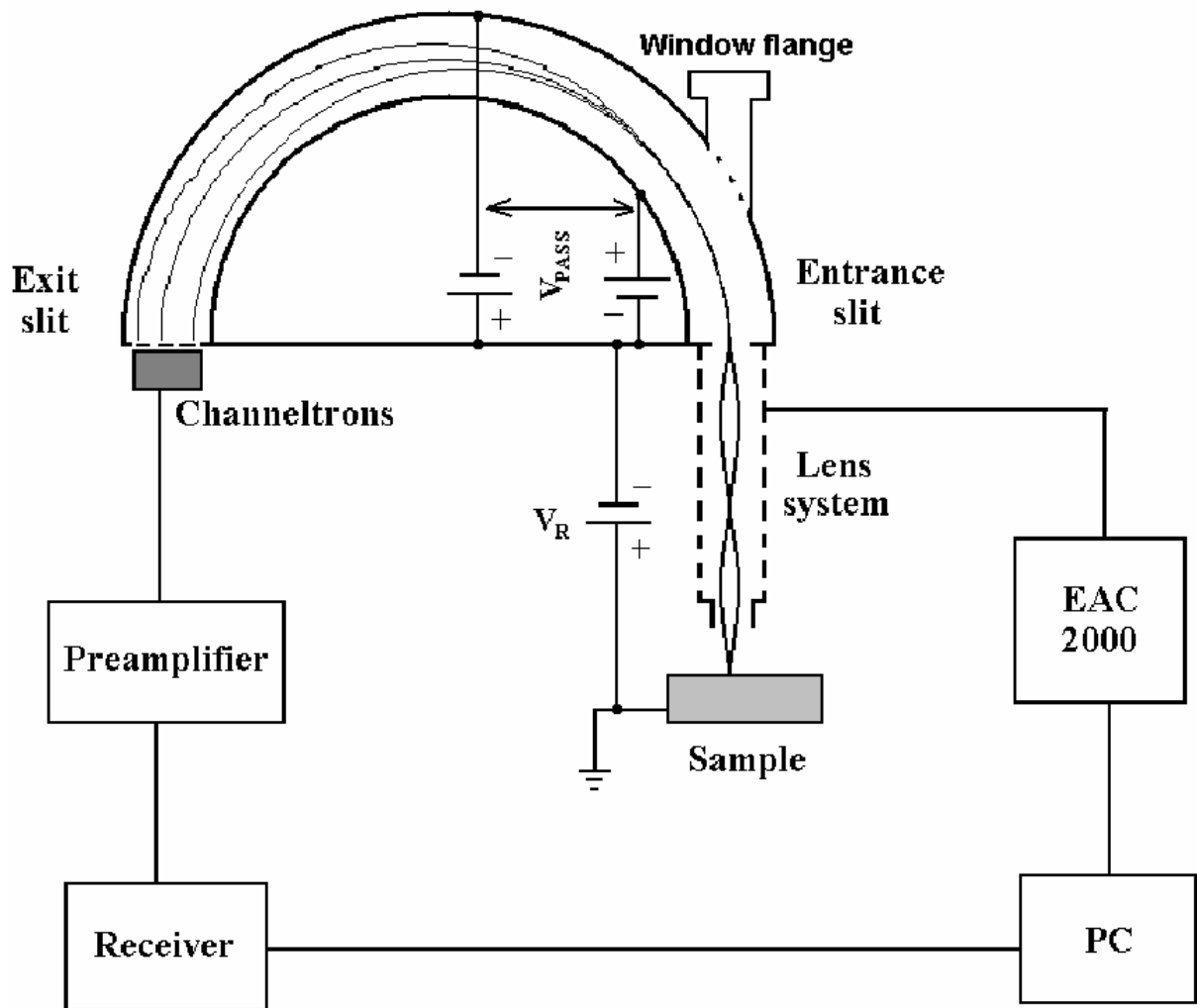
Fig. 2.5.1.1 Schematic diagram of the kinetic energy determination [14]

This analyzer consists of two plates carrying a potential. When the electron is entering the analyzer it passes through an electrical field which forces it to travel along a trajectory as defined by the following equation:

$$F= qE =m(V^2/R)$$

- F - force
- V - speed
- R - trajectory radius
- E - electrical fields established by U potential
- m - electron mass
- q - electron charge

According to this equation, a given electrical field or a given U potential corresponds to a given kinetic energy. It means that the hemispherical analyzer behaves like an energy filter. Knowing a photon and kinetic energies the binding energies can be easily calculated

The whole set of binding energies is possible for each atom, corresponding to the electron ionization from different shells, and this set of energies is characteristic of each element. The measurement of kinetic energies, followed by the calculation of the binding energy, is a basis for the identification of atoms (ESCA).

2.5.2 Application of XPS

XPS, on the contrary, is a powerful method of determining energy levels in atoms and molecules. It is especially useful for studying surfaces of bulk materials because the escaped electrons do not have high energy (usually it is less as 1 keV), they are rapidly absorbed by solid matter. Also they can be emitted only from 2 to 5 nm of the surface. The method is also suitable for the investigation of nanoparticles. As was mentioned, XPS is good for elemental determination.

The way it is usually done, a recording of the "wide SCAN" is generally the first step in the sample characterization. Using two radiation sources allows us to highlight the Auger transitions.

The photoelectron kinetic energy depends on the nature of the source. The aluminum source, for example, is sending hν at 1486.6 eV. The carbon electron is pulled out of its orbit and leaves the matter with a kinetic energy calculated by 1486.6 – 284.6, i.e. 1202 eV. This photoelectron loss will cause several Auger transitions.

In the case of the KLL carbon Auger transition, the Auger electron is ejected with a constant energy independently of the excitation source. The reason for that is that the Auger electron is generated by the internal atom de-excitation (the atom recovers from a higher energy state caused by the loss of the photoelectron).

The computer calculates the electron binding energy simply by subtracting the kinetic energy from the excitation source energy. This difference remains constant for the photoelectron, which implies a fixed core peak in a binding energy co-ordinate system. In the case of the Auger electron, the constant kinetic energy causes the subtraction result to change according to the source excitation energy. By overlapping Al and Mg source spectra we can see that changing from the Mg to the Al source causes Auger peaks to shift by +233 eV.

For the other lines, one should start with the most intense. Each line corresponds to a given

binding energy and tables have been set up to show which orbital is associated with each energy. In some cases there are several solutions.

In such a case, for each solution the positions and ratios of the secondary lines must be checked. The possibility of the presence of "ghost peaks" should be also checked.

If we use an aluminum cathode and suppose that this cathode is, for example, slightly oxidized, oxygen atoms of this cathode will be excited by the electron bombardment exactly in the same way as aluminum atoms. Aluminum hν photons will be supplemented by those from oxygen. The specimen is then excited by two sets of photons and it will in response generate two superimposed spectra. The final spectrum then contains ghost peaks which must be identified so that they are not mixed up with other energy levels or chemical contributions. Oxygen is usually not the only contamination source in an X-ray source. X-ray sources are frequently twin anode sources, as a consequence there may be a cross contamination between anodes or if the Al/Mg coating is not thick and homogeneous enough there could be copper atoms present. The following table (Table 2.5.2.1 [14]) summarizes the main contamination types that may be encountered.

Contamination	Al	Mg
Mg	+233	--
Al	--	-233
O	+961.7	+728.7
Cu	+556.9	+323.9

Table 2.5.2.1 Possible cathode impurities and their influences [14]

In the case of oxygen contamination on a Mg source, each spectrum line will be duplicated at a +961.7 eV distance. The ghost line intensities will be proportional to the contamination intensity. Using a second source is a very valuable method for ghost line identification.

It is also possible to use XPS to probe the local structure of solid materials. The binding energies of electrons can vary depending on the immediate atom environment and its oxidation state. The idea is to find, using standards, a correlation between local structure and "shift" or "splitting" of spectra peaks. An example is shown in Fig. 2.5.2.1 [13]
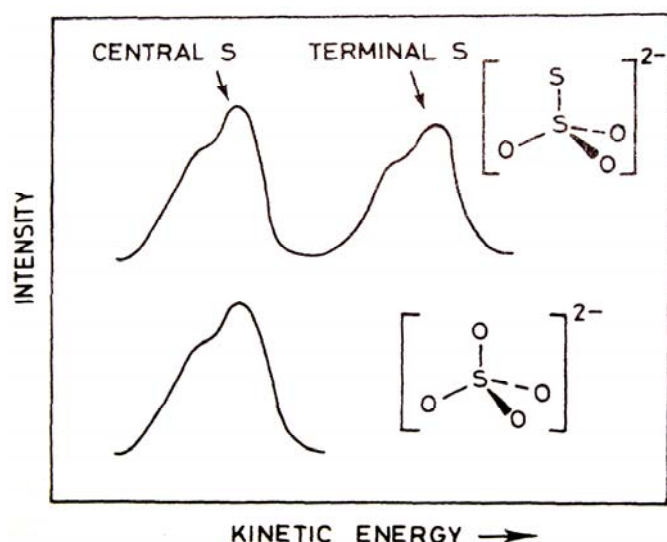
Fig. 2.5.2.1 Schematic XPS 2p spectra of $Na_2S_2O_3$ and Na_2SO_4. A doublet of each peak exists because of the two spin-orbit states, 1/2 and 3/2, of the 2p electron [13]

In $Na_2S_2O_3$, the two types of S atom may be distinguished. Their peaks are almost of the same height, so the numbers of each kind of atom should be equal. The peaks of higher kinetic energy are assigned to the terminal S atom, because this atom carries more negative charge than the central one and is , as a consequence, easier to ionize. Hence binding energy is less and kinetic energy ($h\nu - E_{binding}$) greater for the terminal S atom than for the central S atom. Na_2SO_4, on the contrary, has only a single S 2p peak at the same position as that for the central S atom in $Na_2S_2O_3$.

Another good example is a mixed valence compound KCr_3O_8 or better $KCr^{III}(Cr^{VI}O_4)_2$. Its XPS spectra (Fig. 2.5.2.2 [13]) demonstrate doublets for both Cr 3s and 3p electron peaks. The intensity ratio in doublets is about 2:1, the peaks are assigned to the oxidation states Cr^{VI} and Cr^{III}. This fits in well with expectation that $E_{binding}$ is greater for Cr^{VI} than for Cr^{III} and with the chemical formula ($KCr^{III}(Cr^{VI}O_4)_2$).
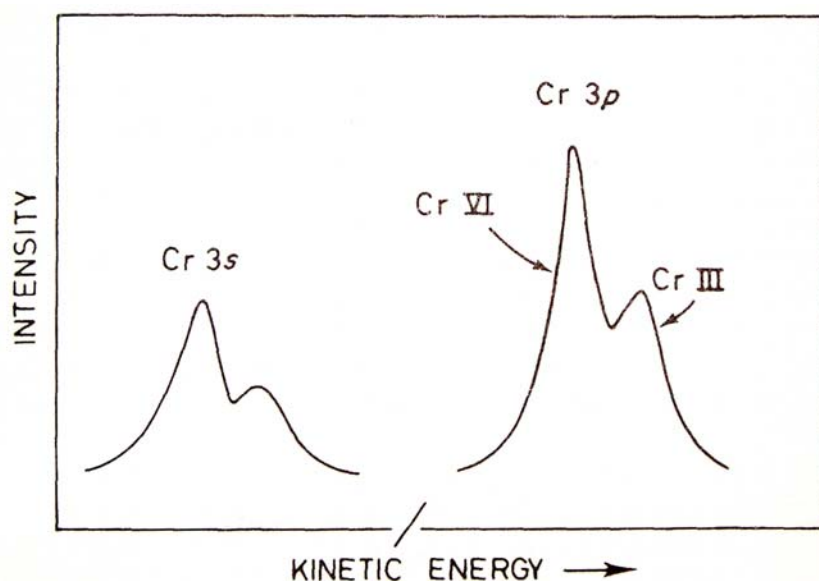
Fig. 2.5.2.2 XPS spectra of Cr 3s, 3p electrons in KCr_3O_8 [13]

The examples demonstrate the influence of local structure and oxidation state on the XPS spectra. In a lot of other compounds, the chemical shifts associated with different oxidation states or local environments are too small to interpret.

There is also a possibility for quantitative analysis (sensitivity 0.3 % [15]). The ratio of elements in the sample can be found comparing the ratio of their peak areas with suitable sensitivity coefficients but it is useful to check these coefficients first with reference compounds.

In the case of boron containing samples they should be phosphorous free, because boron and phosphor electrons have the same binding energy and their peaks cannot be distinguished in XPS spectra.

2.5.3 Experimental

The samples were fixed on sampleholders with especial two side gluing film.

The XPS spectra were measured with an ESCA-Lab 5 Spectrometer from „Perkin Elmer" with the aluminum source in high vacuum (10^{-7} torr) with an acceleration voltage of 12 kV and a current of 5 mA (for the measurement of the wide spectra) or 20 mA (for the measurement of the high resolved spectra).

2.6 X-ray absorption spectroscopy

2.6.1 General background

The atoms of each compound give characteristic X-ray absorption spectra. This is because of their different ionization energies and possibly different inter shell transitions and interactions. The absorption can be quantified by measuring the intensity of the X-rays before and after passing through a sample (Fig. 2.6.1.1 [16]).
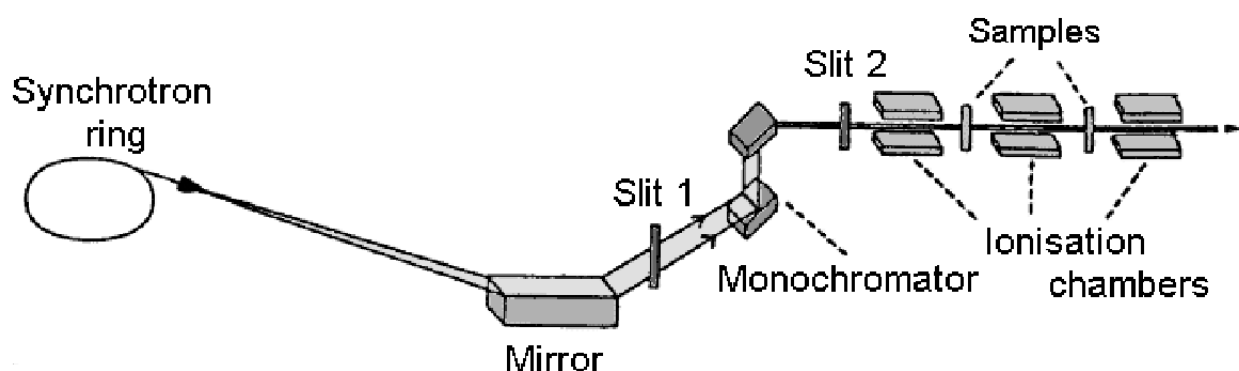
Fig. 2.6.1.1 Schematic view of A1 X-ray beamline at Hamburger Synchrotron Radiation Laboratory (HASYLAB) at DESY in Hamburg [16]

The absorption is usually described by an absorption coefficient μ equal the logarithm from a ratio of intensities measured before and after passing through a sample Fig. 2.6.1.2 [16].

$$I = I_0 e^{-\mu d}$$
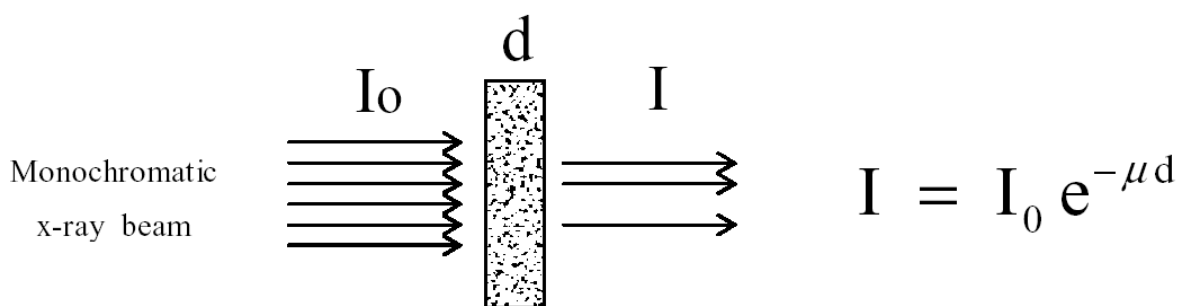
Fig. 2.6.1.2 Schematic representation of x-ray absorption spectroscopic measurements in transmission mode (absorption coefficient μ) [16]

The energy necessary for the ionization of 1s electrons is much higher than for the ionization of electrons of the L shell (2s, 2p). This is why, when we consider the absorption coefficient as a function of ionization energy, the K-absorption edge and the L-absorption edge are considered separately Fig. 2.6.1.2 [16].
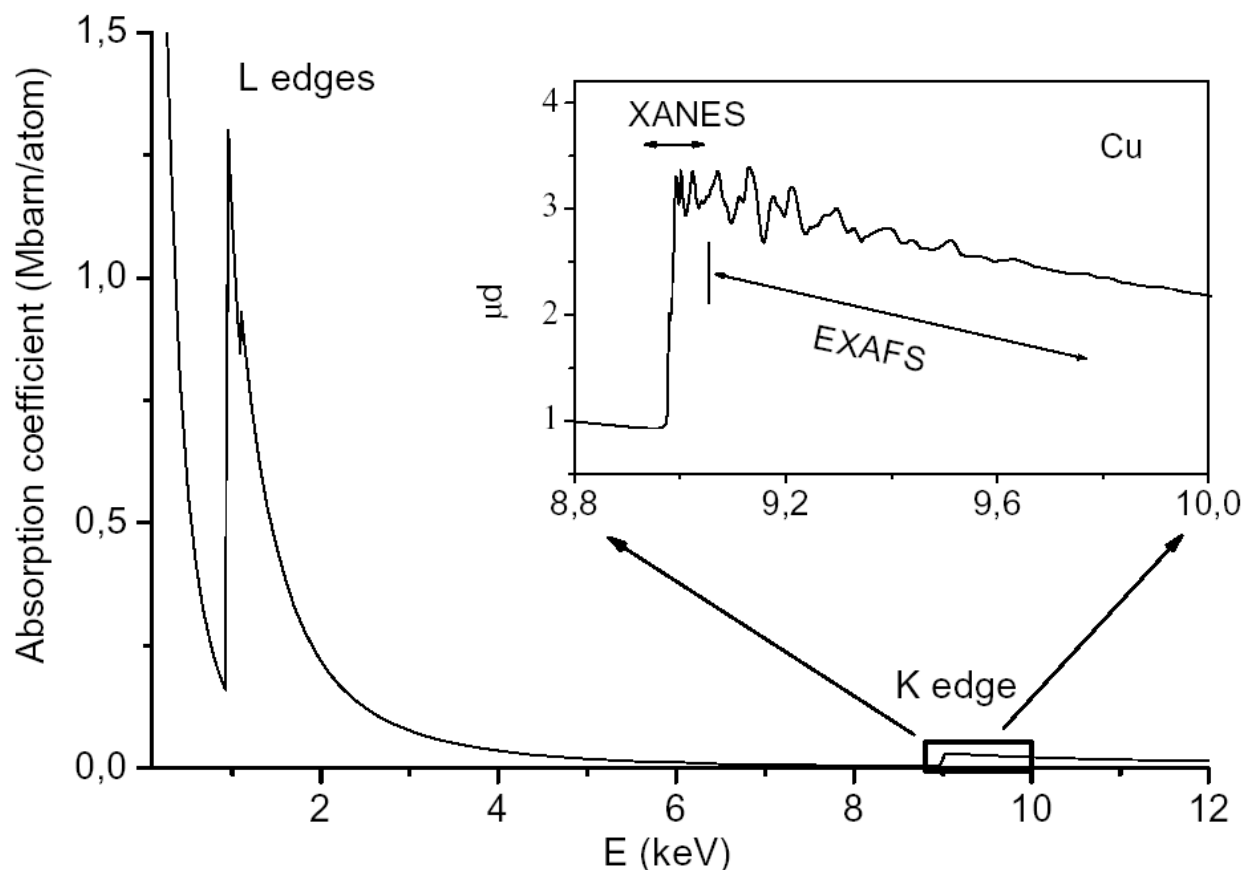
Fig. 2.6.1.2 X-ray absorption coefficient of copper in the region of L and K edges. The box area is expanded in the inset to show EXAFS and XANES signal [16]

The energies at which absorption edges occur depend on the relative separation of the atomic energy levels in atoms, which, in turn, depend on their atomic number in the periodic table (Moseley's Law). That is why absorption edges are characteristic of each element and may be used for their identification. Each edge also has its fine structure which can be used for investigating the local environment of absorption atoms.

In the present work all investigations were made on the K-edge. The typical K-absorption edge is shown in Fig. 2.6.1.2 [16].

A before and after edge area can be divided into two parts: XANES (X-ray Absorption Near Edge Structure), where the multiple scattering of electrons plays the main role , and EXAFS (Extended X-ray Absorption Fine Structure),where a single electron scattering takes place. In

the XANES area, mainly qualitative information can be obtained. For the EXAFS area a mathematical model exists which allows us to obtain some quantitative information as well.

2.6.2 XANES (X-ray Absorption Near Edge Structure)

XANES is very useful for estimating the oxidation state of absorbing atoms. The position of the K-edge depends almost linearly on the oxidation state, as shown in Fig. 2.6.2.1 [17].
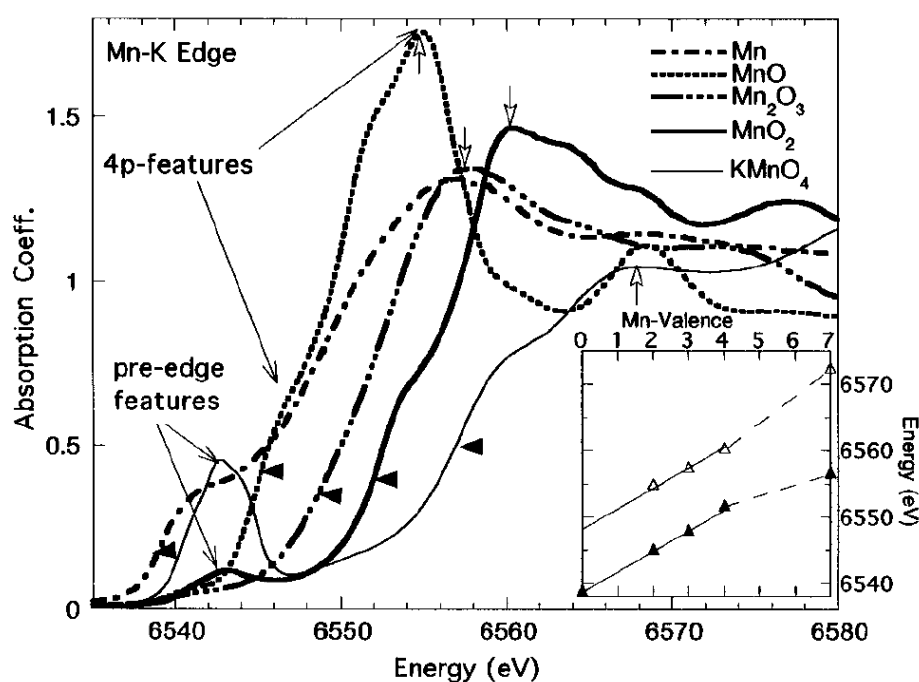
Fig. 2.6.2.1 Mn K-edge spectra for the series of Mn^{n+} (n = 0, 2, 3, 4 and 7) standards. The dark arrow heads indicate the first inflection point at the main edge traditionally used to define the chemical shift. The open arrows indicate the energy of the peak at the edges of the oxide standards. Selected $4p$ features for MnO and the pre-edge (Mn d related) features of MnO_2 and $KMnO_4$ are indicated (inset). The chemical shift of the standard Mn compounds (solid triangles) versus the formal Mn valence. Also plotted in the inset are the energies of the peaks (open triangles) of the oxide standards [17].

When comparing samples of different chemical composition, one should be careful because the position of the K-edge depends not only on the oxidation state of the absorbing atoms but on the type (atomic numbers) of the scattering atoms also; the positions of the K-edges of MnO and $MnCl_2$ would not be exactly the same, in spite of their oxidation states being identical. One could say that the ionization energy increases with the atomic number of the scattering atoms.

36

Another interesting possibility is to investigate pre-edge features, corresponding to the 1s =>3d electronic transition, dipole forbidden but quadrupole allowed, which is very big for some transition metals such as V or Ti and sometimes (e.g. for Ti-system) correlates with a coordination number as shown in Fig. 2.6.2.2, where selected Ti K-edge XANES spectra collected for oxide-type model compounds with Ti^{4+} is located in fourfold-, fivefold- and sixfold-coordination sites are depicted. The area and normalized height of the pre-edge peak A is inversely proportional to coordination number [128].
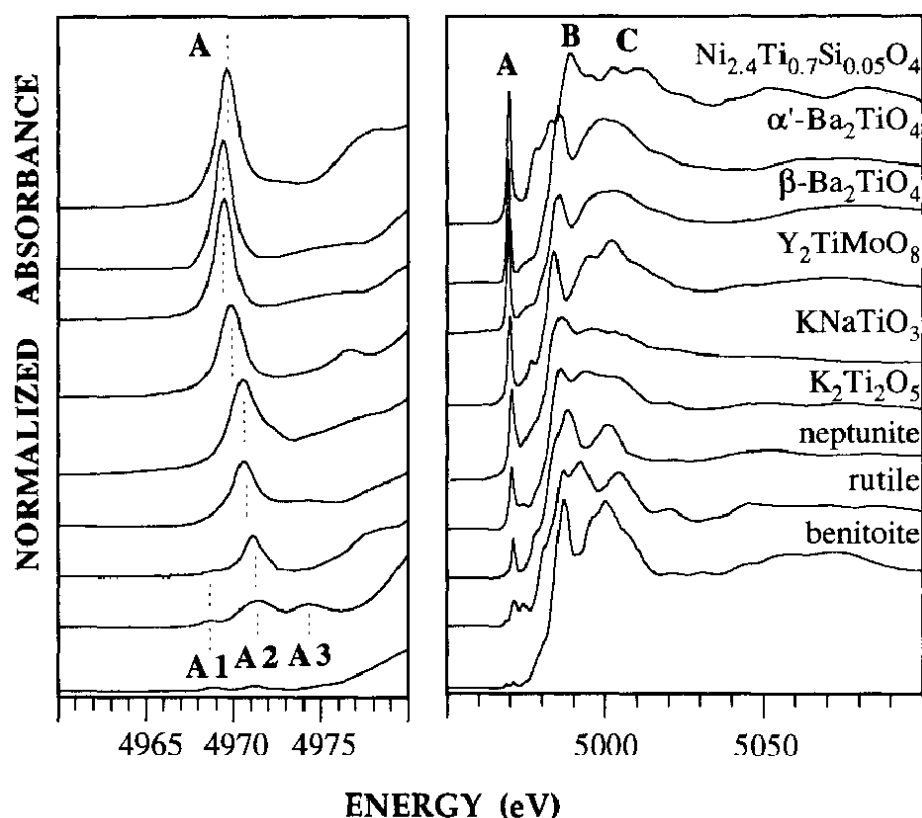
Fig. 2.6.2.2 (right) Normalized Ti K-edge XANES spectra for selected Ti-bearing model compounds containing [4]Ti, [5]Ti and [6]Ti. (left) Details of the normalized pre-edge feature. [134]

For some systems this feature also contains structural information, it could indicate a non-centrosymmetric environment of the absorbing atom. So sometimes it is possible to distinguish tetrahedral and octahedral coordination of an ion as shown in Fig. 2.6.2.3 [18].
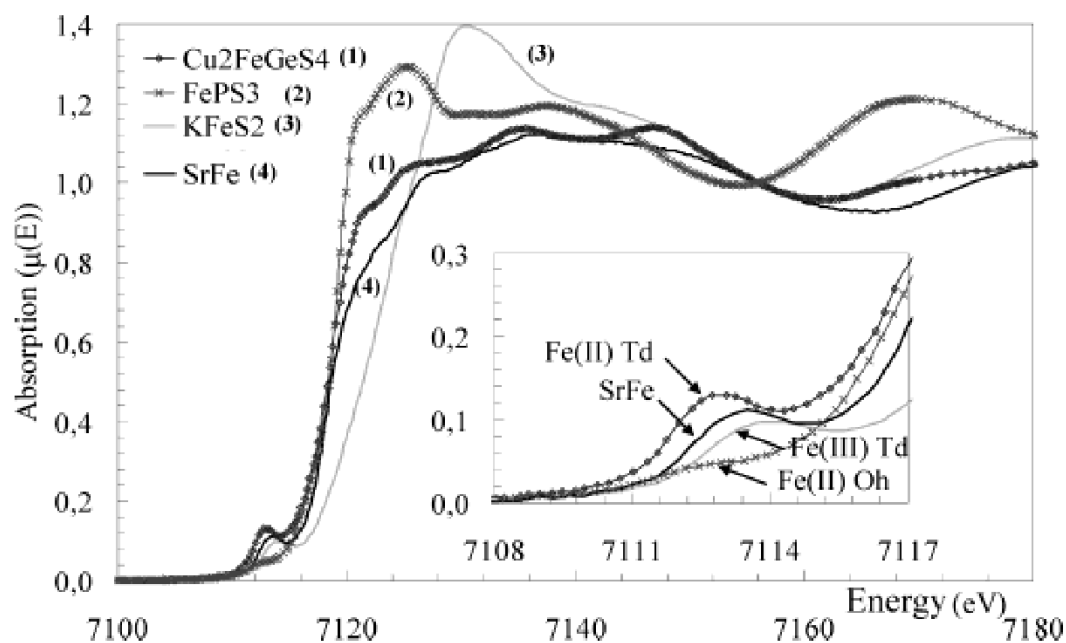
Fig. 2.6.2.3 XANES spectra at Fe K-edge for some reference materials and $[Sr(Fe_{0.77}Nb_{0.23})_{0.5}S_{1.5}]_{1.13}NbS_2$ (strong solid line, signed as SrFe). Inset shows a zoom on the pre-edge part; T_d = tetrahedral, O_h = octahedral [18].

In another very interesting paper the correlation between the presence, position and shape of the pre-edge feature is described for the Fe K-edge, and oxidation state, coordination numbers and symmetry are derived for a large number of minerals containing iron [19].

XANES may also be used for the quantitative determination of the composition of a mixture of species. The two most common methods are: Least squares linear combination fitting (LC) and Principal component analysis (PCA). LC is quite a straightforward traditional approach; a group of pure standards is chosen, then their edges are fitted to a measured sample edge. But a number of questions arise as for example: how many standards are necessary or how to check the model correctness. And if wrong standards are chosen, there is no way a correct answer can be derived. That is the reason why the PCA method should be preferred to the LC method for investigations of mixtures. The LC method is based on linear algebra - each spectrum is represented by a vector. The aim is to find the number of components that can reproduce the experimental spectra [17].

2.6.3 EXAFS (Extended X-ray Absorption Fine Structure)

The extended X-ray absorption fine structure area usually comprises the area from 50 eV after the K-edge, it is approximately 1200 eV long. The normalized oscillatory part of the absorption coefficient is calculated [21]:

Mathematically, EXAFS (E) is defined as the periodic change of μ relative to the nonmodulated absorption coefficient μ_0 (i.e. the absorption coefficient of an isolated atom of the same kind).

$$\chi(E) = [\mu(E) - \mu_0(E)]/ \mu_0(E)$$

χ is also usually expressed as a function of the wave vector $k = 2\pi/\lambda$:

$$\chi(k) = [\mu(k) - \mu_0(k)]/ \mu_0(k)$$

At energy values above the absorption edge, $\mu(k)$ shows fluctuations, like a sine function, as a result of scattering from each shell of atoms at R_j, the average radial distance from absorber atom to the *j*-th atoms. This phenomenon, EXAFS, or the oscillatory characteristics of the X-ray absorption coefficients in matter, is very useful in its application in obtaining structural information, and is given by:

$$\chi(k) = (-1)^l/k \cdot \sum_j N_j/(R_j)^2 |F_j(k)| \cdot e^{(-2(\sigma_j)^2 k^2)} \cdot e^{(-2R_j/\lambda_j(k))} \cdot \sin[2kR_j + \varphi_{ij}(k)]$$

where:

k - photoelectron wave number, defined as $k = [2m_e E(k) - E_0(k)(2\pi/h)^2]^{1/2}$, $E(k)$ is the kinetic energy of the ejected photoelectron measured from the absorption edge, $E_0(k)$ is the null point energy of the Fermi energy at low energies (≤30 eV) and $E(k) - E_0(k) = h\nu - E_k - E_0(k)$, where E_k is the binding energy of the 1s electron before absorption

l - Angular momentum quantum number

N_j - Number of neighboring atoms, i.e. backscattering atoms in the j-th coordination shell

R_j - Average radial distance of the j-th shell backscattering atoms from absorber atom

$|F_j(k)|$ - Backscattering amplitude of neighboring atoms in j-th coordination shell. In addition to k, it is also dependent on the scattering angle β

$e^{(-2(\sigma_j)^2 k^2)}$ - Debye-Waller factor, accounts for thermal vibration or atomic disorder; σ_j is the root mean square fluctuation of the j-th shell atoms about R_j

$e^{(-2R_j/\lambda_j(k))}$ - Accounts for decay of photoelectron with mean-free pass λ as a result of electron-electron scattering

$\varphi_{ij}(k)$ - Phase shift experienced by the photoelectron in the potential field of the absorber and of the backscattering atoms. That the photoelectron experiences twice the potential field effect of the absorber atom i (outgoing and entering) and once that of the backscattering we have:

$$\varphi_{ij}(k) = 2\varphi_i + \varphi_j(k)$$

$2kR_j$ - Period of a seemingly sine function attributed to atoms in the j-th coordination shell at distance R_j from the absorber atom

The EXAFS function, $\chi(k)$, is valid for only isotropic compounds. For oriented samples, such as single crystals and surface adsorbate, one has to consider polarization effects when employing radiation of high degree of linear polarization, such as the synchrotron radiation [21].

Unfortunately, these values are not independent of one another. Examples of how modifications of each of these parameters influence the Fourier transformed absorption function are demonstrated in Fig 2.6.2.1 and Fig 2.6.2.2 [21].

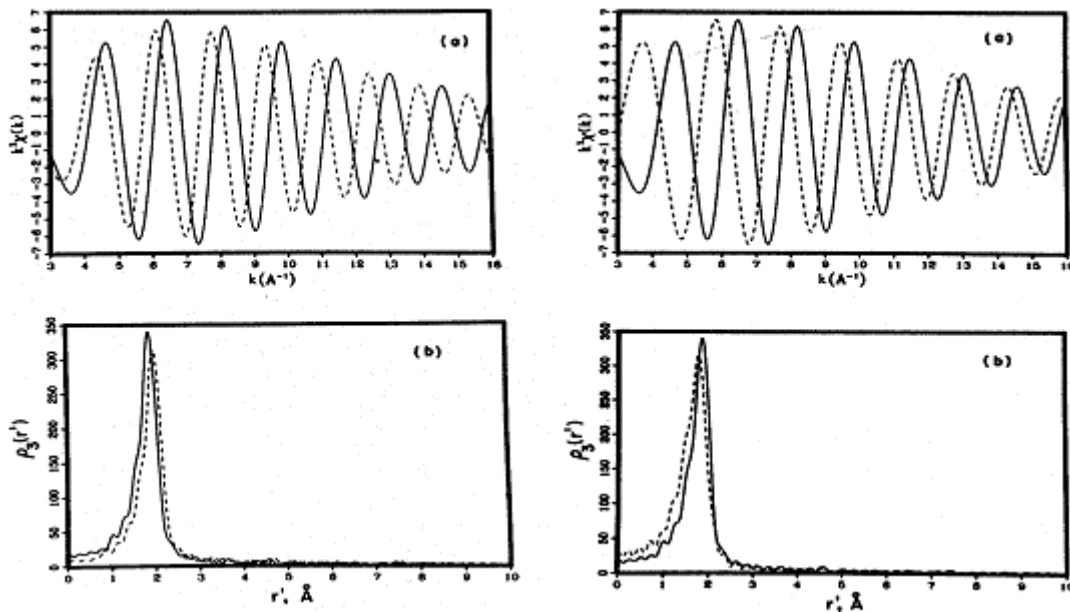Fig 2.6.3.1 (right) Effect of the distance R on the EXAFS data in k (a) and r (b) space. In both (a) and (b), $R = 2.3$ Å (solid curve) and 2.3 Å (dashed curve); the remaining variables are the same. (left) Effect of ΔE_0 on the EXAFS data in k (a) and r (b) space. In both (a) and (b), ΔE_0 = 0 eV (solid curve) and - 30 eV (dashed curve); the remaining variables are the same [21]
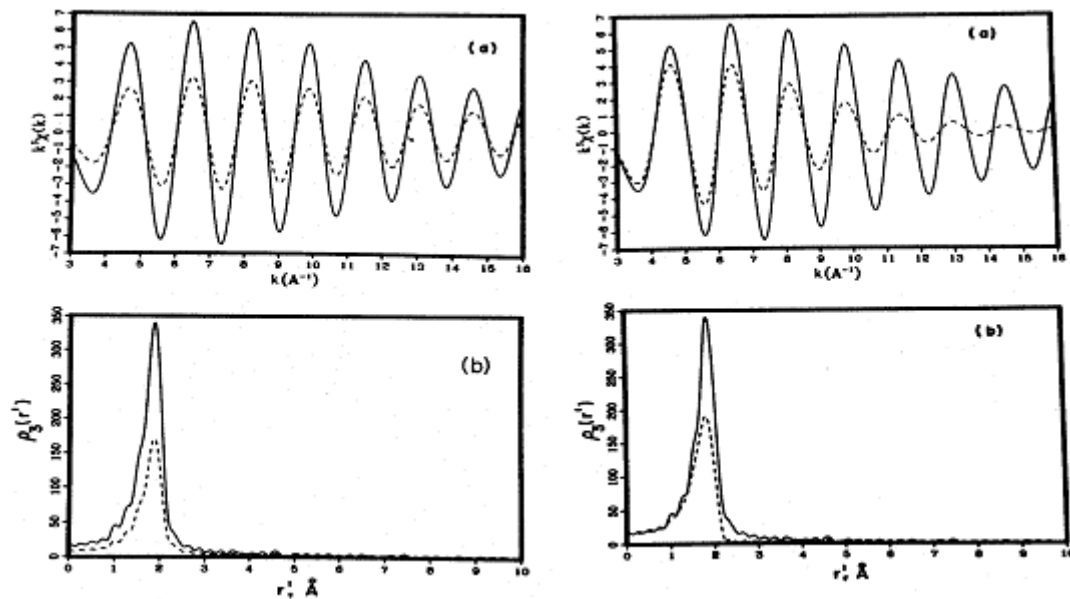
Fig 2.6.3.2 (right) Effect of the coordination number N on the EXAFS data in k (a) and r (b) space. In both (a) and (b), N = 2 (solid curve) and 1 (dashed curve); the remaining variables are the same. (left) Effect of the Debye-Waller factor σ on the EXAFS data in k (a) and r (b) space. In both (a) and (b), σ = 0.05 (solid curve) and 0.09 (dashed curve); the remaining variables are the same [21]

That is why it is recommended first to fit energy shift and Debye-Waller factor on some known (with known coordination numbers and distances) compound with a similar composition and then use these parameters as a start set, fit an experimental sample. Programs "WinXAS" [70, 134], "ATOMS" [135] and "FEFF7" [136] were used. EXAFS spectra allow to estimate semiqualitative the atomic distances (Fig 2.6.2.3 [129]), if the substance is crystalline or not, it can be used as a finger print.
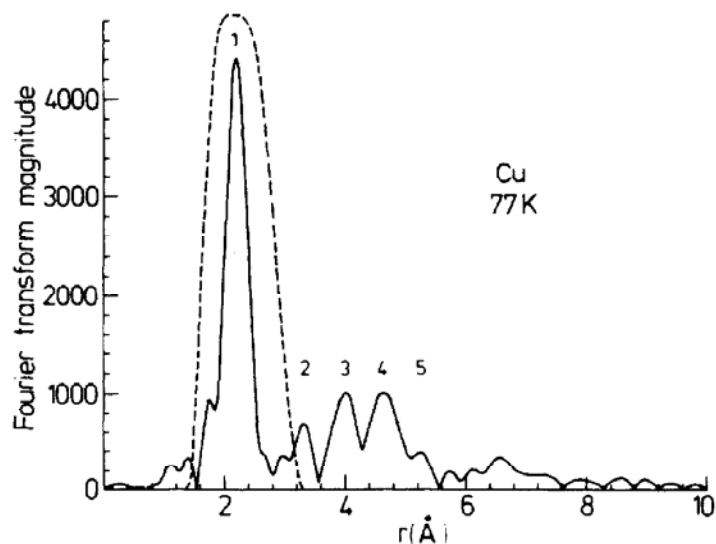
Fig 2.6.3.3 Absolute value of the Fourier transform. The peaks labeled 1 to 5 are due to the backscattering of the photoelectron from the first five shells respectively. The not normalized average radial distances of the j-th shell backscattering atoms from absorber atom can be measured on the *r* axis [129]

According to some other work [22] the peak at the distance of approximately twice the distance of a main peak can arise from multiple scattering pathways involving the absorbing atoms.

Its intensity is very sensitive to deviations of the bond angle from 180° at the absorbing atom and could be used for calculations of the bond angle (Fig 2.6.2.4 [22]).
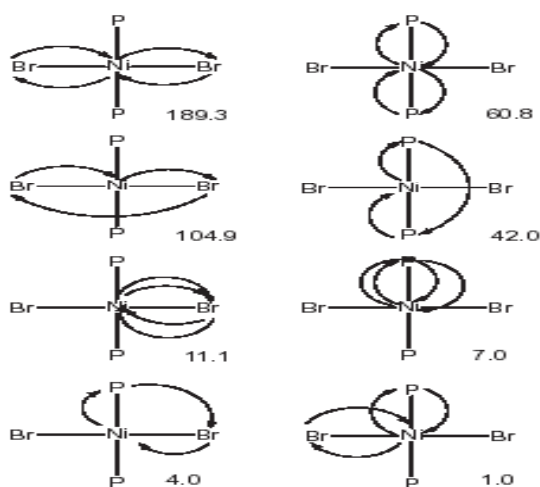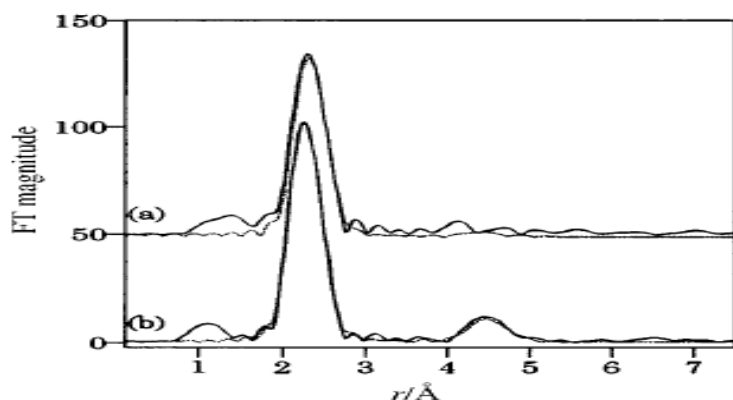
Fig 2.6.3.4 (above) Fourier transforms of Ni K-edge XAFS data at 10 K of (a) *tetrahedral-*[NiBr$_2$(PPh$_3$)$_2$] and (b) trans-[NiBr$_2$(PEt$_3$)$_2$]. Experimental data, solid line; calculated data, dotted line. (below) Diagrammatic representation of the multiple scattering pathways (and their relative importance) that contribute to the 2 R features in Ni K-edge XAFS data of trans-[NiBr$_2$(PEt$_3$)$_2$] [22]

2.6.4 Experimental

The samples were mixed together with polyethylene powder. The necessary amount of a sample depends from the chemical composition and was calculated with a program "XAFS mass" [137]. The mixture was pressed with a hydraulic press in 10 mm diameter pellets. The pellets were measured at the Hamburg synchrotron, DESY, HASYLAB, Beamline A1with Si (111) monochromator, in transmission mode, under vacuum of 10^{-2} mbar. The measurement was done in the energy range of 6950 to 8100 eV with energy steps of 5 eV for the Fe K-edge, from 3900 to 4700 eV with energy steps of 5 eV for the Ca K-edge and from 16000 to 17000 eV with energy steps of 5 eV for the Sr K-edge. A schematic view of the measurement experiment is shown on the Fig. 5.1.1 [16].

The data reduction of experimental absorption spectra and EXAFS fitting and simulation were carried out using the program "WINXAS 3.1" [70, 134]. For energy reference a metal foil was measured together with each sample. The reference energy threshold E_0 of the metal foil was determined from the first inflection point in the spectra and raw data were linearly calibrated against the difference between the obtained experimental E_0 and the tabulated absorption edge energy (Fe K-edge reference $E_0 = 7112$ eV, Ca K-edge reference $E_0 = 4038$ eV, Sr K-edge reference $E_0 = 16105$ eV). Pre-edge background subtraction and normalization was carried out by fitting a linear polynomial to the post-edge region of an absorption spectra. A smooth atomic background, $\mu_0(k)$, was obtained using cubic splines. The fitting range in k space, the number of spline knots and k-weighting were optimized to afford a rigid background curve at low k, minimization of low R peaks in the Fourier transformed signal and symmetric peak shapes. The radial distribution function FT($\chi(k)$) was obtained by Fourier transforming the k^3-weighted experimental $\chi(k)$ function, multiplied by a Bessel window, into the R space [70].

2.7 Electron microscopy

2.7.1 Background

Electron microscopy is nowadays an extremely important research method capable of providing structural information over a wide size range. It allows to study the texture, topography and surface features of powder or solid piece samples, at magnifications where it is impossible with any kind of optical (laser) microscopy. With modern scanning electron microscopy (SEM) features up the nanometer scale can be seen, and owing to the depth of focus of the SEM device the resulting pictures have a definite three-dimensional quality. At the same time, high resolution transmission electron microscopy (HRTEM) is able, under some conditions, to give information on an atomic scale by direct lattice imaging. A resolution of about 0.2 nanometers is achieved , so it is really possible "to see" separate atoms.
Electron microscopes are constructed either in transmission or in scanning mode.

2.7.2 Transmission Electron Microscopy

In transmission mode, the sample should not be thicker than about 200 nanometers. The reason is the absorption of electrons by the sample. It makes sample preparation and investigation somewhat difficult. The most common procedure is to grind a sample into a fine powder, which would ensure that at least some of the particles would be thin enough. Thinning techniques could be used, for example, ion bombardment , but this is not always successful. Another possible solution could be to use an instrument with a higher voltage (e.g. 1 MV); thicker samples could be investigated and higher resolution obtained. The principle that the TEM microscope works on is shown in Fig. 2.7.2.1 [26]. Electrons are emitted from the filament (tungsten, LaB_6 etc.). Electron microscopes contain several electromagnetic lenses. The condenser lenses form and control the size and angular spread of the electron beam. Electrons are accelerated through a high voltage (e.g. 300 kV). Their wavelength is related to the accelerating voltage (V) by $\lambda = h(2meV)^{-1/2}$, *h* is the Planck constant, *m* and *e* electron mass and charge respectively. The electron wavelength is much smaller than that of the X-rays, which allows the high resolution in electron microscopy.

The electron beam is incident on the sample. Transmitted electrons then pass through objective, intermediate and projector lenses and form a magnified sample image on the screen (the camera translating the image onto the computer).
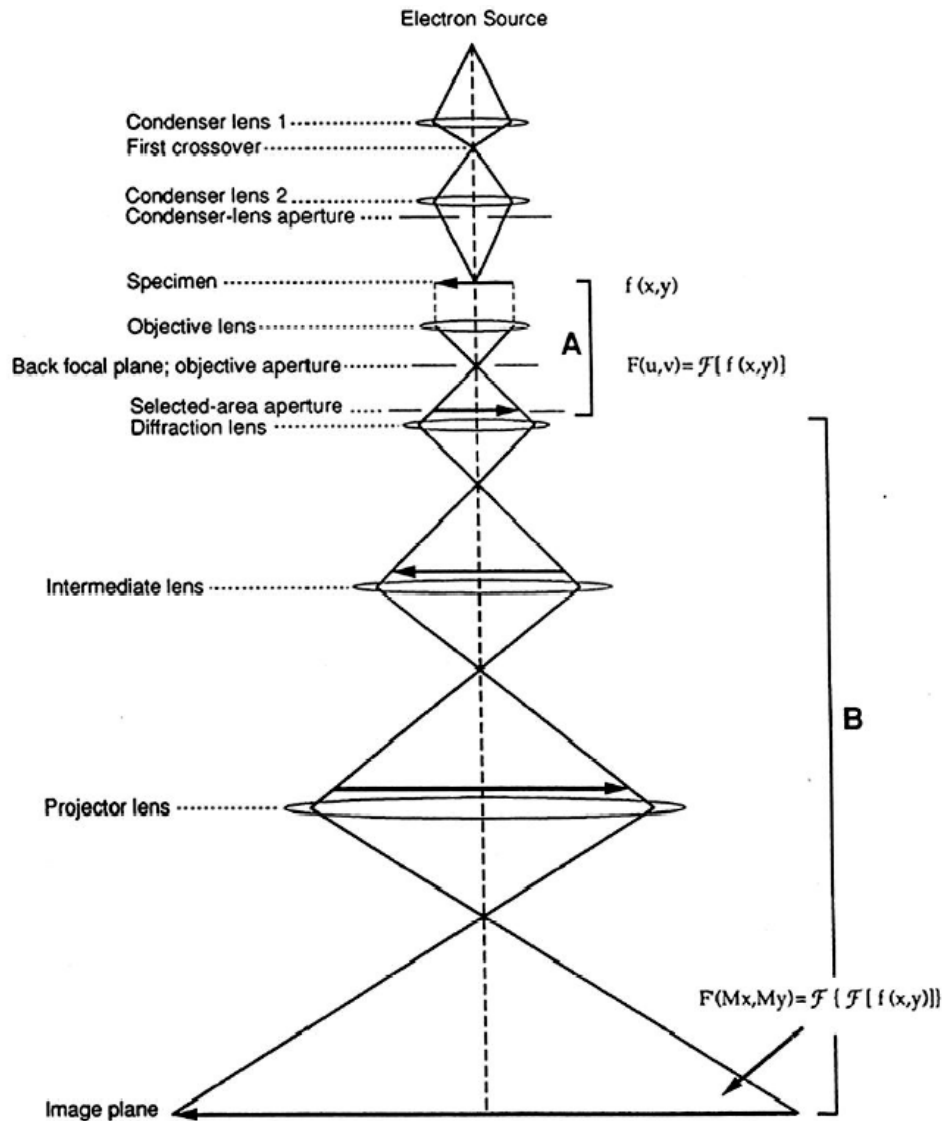
Fig. 2.7.2.1 Ray-diagram of a transmission electron microscope. The horizontal arrows indicate the specimen and its images as they are progressively enlarged at various levels of the microscope. In stage "A" the beam is scattered in the specimen and the primary (diffraction) image is formed. In stage "B" the image is magnified and projected on the image plane.[26] The quality of the pictures may be improved by dark field imaging. This method is known from optical microscopy, it is only the diffracted beams from the specimen that are allowed to recombine to form the image.

The resolution is so high that domain structures can be seen in ferromagnetic and ferroelectric materials; crystal defects such as dislocations, stacking faults, antiphase and twin boundaries

could be seen directly. By changing of the position of the screen (camera) the electron diffraction pattern of the specimen can be seen.

2.7.3 Selected Area Electron Diffraction

The Selected Area Electron Diffraction (SAED) method can sometimes supply some additional information about unit cell and space group, or be used for phase identification. However, it is not really reliable because secondary diffraction usually occurs. There are two undesirable consequences: extra spots in the electron diffraction pattern, intensities are unreliable and cannot be used quantitatively for crystal structure determinations.

2.7.4 Electron Energy Loss Spectroscopy

A very important process during the transmission of electrons through a sample is the loss of electron energy. Electron energy loss spectroscopy (EELS) analyses the energy distribution of (initially) monoenergetic electrons after their interaction with a sample. The interaction happens only in a few atomic layers, this is why the measurement should be carried out in a high vacuum. Otherwise only oxide or carbon impurities (from the material of sampler) on the surface of specimens would be measured. When a sample in a microscope is bombarded with high-energy electrons, quite a number of things happen, Fig. 2.7.4.1 [13].
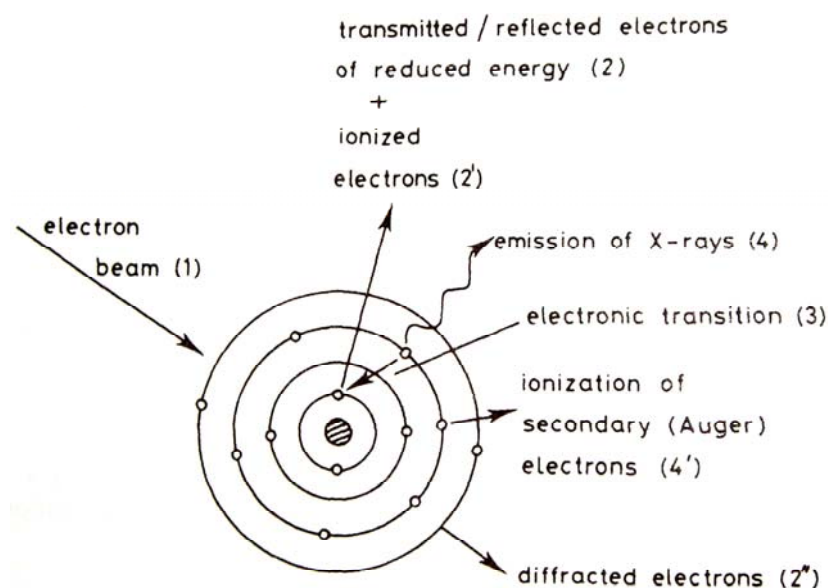

Fig. 2.7.4.1 Processes that take place during the bombarding of a sample with electrons [13]

47

Only the primary and secondary processes of the inelastic interaction of an electron beam with the electron shell of sample atoms - during which the electrons of the primary beam lose their energy - are considered here. The atom electrons could be excited only to Fermi level and higher, because all levels below Fermi one are occupied. They need a relatively large amount of energy for this (from several hundred to a thousand electron volt). The primary electrons lost the necessary for the excitement energy.

An atom cannot exist for long in a state of excitement. It relaxes when one of the electrons of the external shell takes up the electron vacancy, emitting any surplus energy in the form of X-ray radiation. In case an excited electron is not emitted, it can also go back irradiating the energy excess as X-rays. Another possibility is the transfer of energy to an external level electron as kinetic energy. The electron is emitted (auger electron). Because the electron shells are element specific, the energy loss of inelastic interaction is also element specific. It allows us to use electron energy loss spectroscopy for element analysis [23]. Electron energy loss spectroscopy can be used for both quantitative and qualitative analysis. Light elements lend themselves especially well to this kind of analysis. The only problem in our case is that boron and phosphorous edges cannot be distinguished from one another. With the help of EELS information about the electronic situation (band states, coordination and oxidations states) can be obtained. The method can be applied to crystalline and amorphous samples. The EEL spectra present the intensity of the scattering of primary electrons as a function of the loss of their kinetic energy. Three areas could be distinguished: zero-loss peak, low-loss-region, and high-loss-region. The zero-loss-peak detects electrons that have not lost any energy; it has the highest intensity and serves for the calibration of spectra. In the low-loss-region (it follows after the zero-loss-peak up to 50 eV) electrons are found which have interacted with electrons of external shells. The region contains information about the electronic situation of the sample. The estimation of the band gap is possible. The high-loss-region (>50 eV) contains information about the inelastic scattering of primary electrons on the internal shells. The peaks in this area are known as element edges, because their positions in spectra are element specific. The edges are marked as K-edges or L-edges etc., depending on the shell with which primary electrons have interacted. The edges have a very strong background, due to excitation in elastic scattering. Integrating the edges whilst taking into account the background allows a quantification of elements in a specimen to be made. The necessary condition is that the element edges should be within one energy loss region.

2.7.5 Scanning Electron Microscopy

For SEM instruments, on the other hand, sample thickness is not a problem at all, no special methods of preparation are required. Usually it is only necessary to coat a sample surface with a conducting layer (carbon or some metal, very often gold), especially if a sample is a poor electrical conductor, in order to prevent a charge building up on the surface of the sample. The range of resolution of a SEM lies between the limit of resolution of optical microscopy (about 500 nanometers) and tens of nanometers.

In the scanning electron microscope electrons from the filament (electron gun) are focused on a very small spot on the surface of the specimen. The electron beam scans the whole surface systematically, similarly to the electron gun in a TV-set, secondary electrons are emitted from the sample and used to build up an image of the sample surface on a screen. The disadvantage of the SEM is lower resolution compared with TEM.
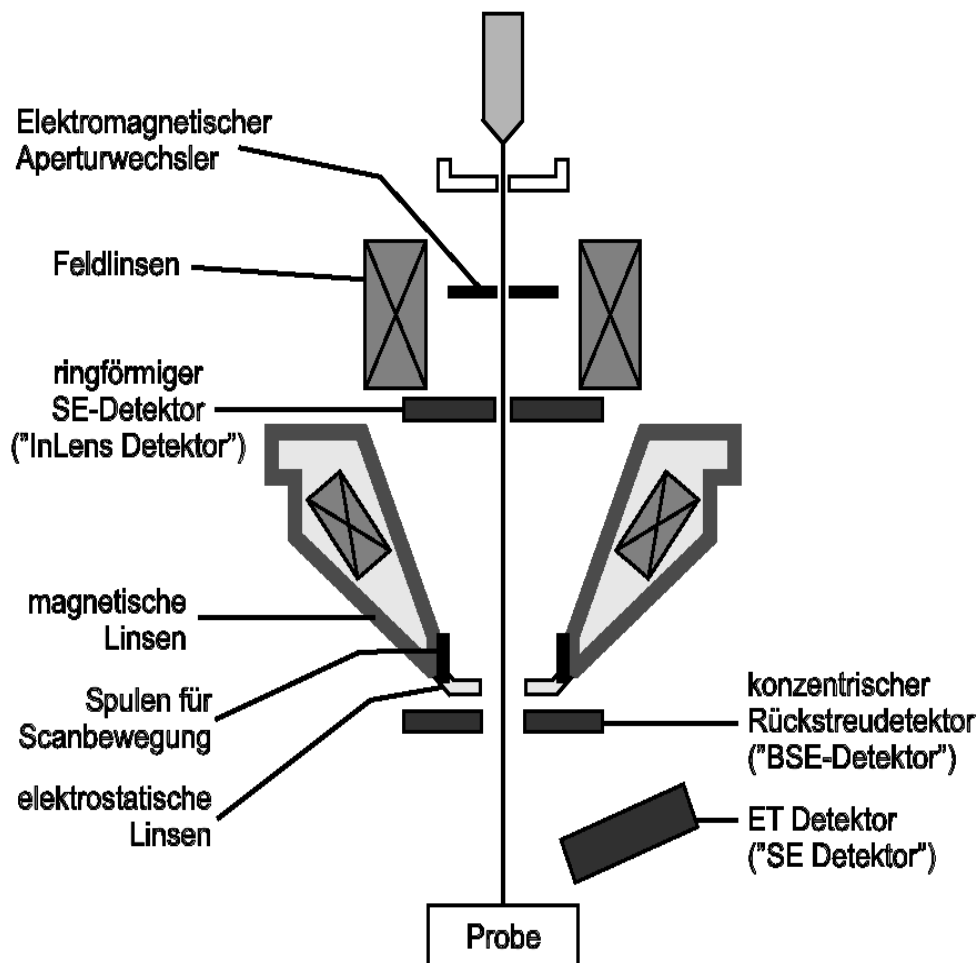

Fig. 2.7.5.1 Basic components of a scanning electron microscope [28]

2.7.6 Energy Dispersive X-ray spectroscopy

Today, almost all SEM and TEM microscopes have additional features for the elemental analysis of samples. In the present work it was energy dispersive X-ray analysis (EDX), in which the energy of X-rays generated by bombarding a sample electrons is scanned. Each element has its own characteristic energies and it is characteristic for each element presents. Under appropriate conditions and after calibration, quantitative analysis is also possible. Unfortunately, for elements lighter than Na the method is not sensitive enough, and in the case of boron, it cannot be always discriminated from the carbon energy peak. When the sample is so thin that the carbon peak from the substrate can be observed, or if the sample includes carbon containing ligands, the carbon signal is so strong that a quantitative, and very often even qualitative analysis of boron is impossible. In this case some other method must be used, for example EELS.

2.7.7 Experimental

The electron energy loss spectra (EELS) were recorded using a TEM CM 30-ST (Philips, 300 kV, LaB_6-filament) equipped with a PEELS 666 spectrometer (Gatan) with a YAG scintillation detector.

High-resolution transmission electron microscopy (HRTEM), selected area electron diffraction (SAED), and energy-dispersive X-ray analysis (EDX) were performed using a TEM CM300 (Philips, 300 kV, LaB_6-filament) equipped with a EDX-spectrometer (EDAX, Si(Li)).

Scanning electron microscopy (SEM) experiments were performed on a SEM LEO 1550 Supra (Oxford, 30 kV, FEG-filament), equipped with a EDX-spectrometer (Oxford, Si(Li)).

2.8 Infrared spectroscopy (IR)

2.8.1 Background

Infrared spectroscopy is a very useful instrument in chemistry. It makes use of the fact that atoms in solids vibrate with individual frequencies of 10^{12} to 10^{13} Hz [13]. If a sample is radiated with the appropriate frequency the separate vibration modes can be evoked.

The same atomic bonds can vibrate in several different modes (e.g. stretching or bending), which is why individual atomic bonds may absorb more than one IR frequency. Stretching absorptions usually have a stronger intensity than bending, however the weaker bending absorptions can be useful in differentiating between similar types of bonds (especially in organic chemistry). It is also very important to note that symmetrical vibrations do not cause absorption of IR radiation. For example, neither of the carbon-carbon bonds in ethene or ethyne absorb IR radiation. The other important fact is that one of the major factors influencing the IR absorption frequency of a bond is the identity of the two atoms involved. More precisely, it is their atomic mass which is important. The greater the mass of attached atoms, the lower the IR frequency at which the bond will absorb.

The atomic bonds in different environments will absorb varying intensities and at varying frequencies. Thus IR spectroscopy involves collecting absorption information and analyzing it in the form of a spectrum. The frequencies at which there are absorptions of IR radiation ("peaks" or "signals") can be correlated directly to bonds within the researched compound. The range in which we have usually measured is 4000 to 400 cm^{-1}. Since metal-boron bonds appears below 400 cm^{-1}, the method is suitable for detecting impurities but not for characterizing borides.

The boron-oxygen bond can be easily detected and indicate presence of metal borates [30-29], as shown in Fig. 2.8.1 [29], where a broad band at around 1450 cm^{-1} was observed for crystalline B_2O_3 which was present in V_2O_5 glasses.

Glasses low in V_2O_5 show a very sharp absorption peak at 1195 cm^{-1}. This peak may be attributed to triangular B-O stretching vibrations [29].

.
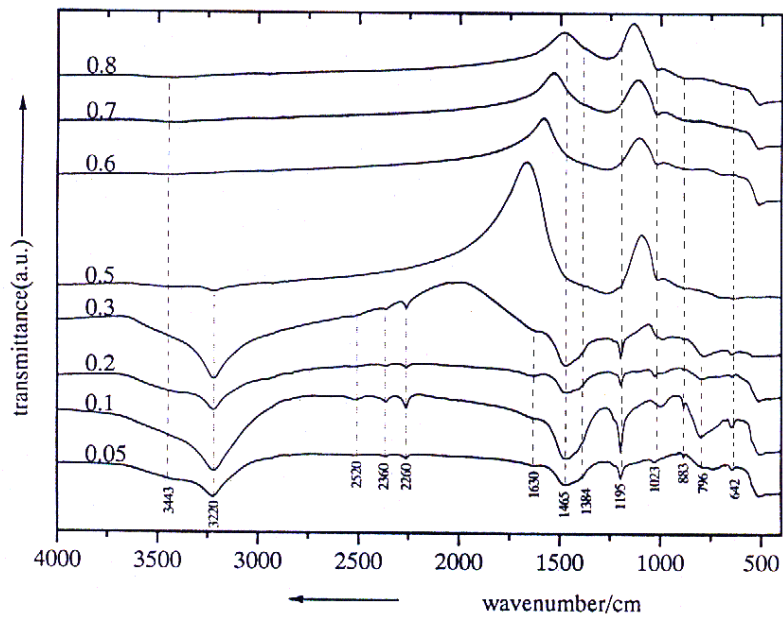
Fig. 2.8.1 IR spectra of $xV_2O_5(1-x)B_2O_3$ glasses with $0.05 \le x \le 0.8$ [29]

2.8.2 Experimental

The samples were mixed together with vacuum-dried (300 ˚C, 12 h) KBr powder under argon in a glove-box, ratio 5/200 mg and pressed with a hydraulic press, in 10 mm diameter pellets. Than the pellets were measured with "Infrared Fourier Transform Spectrometer" 1720 (Perkin-Elmer), the spectrometer was managed with a program "Spectrum v2.00" (Perkin-Elmer).

2.9 Conductivity measurements

2.9.1 Types of conductivity

When talking about electronic conductivity, one usually distinguishes between several types of conductors: metals, semiconductors and insulators. At a first glance, the main difference is their degree of conductivity. The conductivity of metals is very high, $\sigma \sim 10^4$ to 10^6 ohm^{-1}cm^{-1}; insulators conduct very poorly, or not at all: $\sigma \leq 10^{-15}$ ohm^{-1}cm^{-1}, and the conductivity of semiconductors ranges from $\sigma \sim 10^{-5}$ to 10^3 ohm^{-1}cm^{-1}. The boundaries between these three kinds of conductors are somewhat arbitrary and overlaps occur.

Another fundamental difference between the three sets of conductors is a different conduction mechanism in metals, on the one hand, and semiconductors/insulators, on the other. This can be seen from the temperature dependence of conductivities: for most semiconductors and insulators conductivity grows rapidly with increasing temperature, while that of metals decreases slightly but gradually.

Conductivity is usually determined by a simple equation: $\sigma = n\,e\,\mu$, *n* is the concentration of electrons, *e* their charge and *μ* their mobility. The temperature dependence of different materials can be explained by considering *n* and μ as functions of the temperature. Mobility is similar for most materials in that it decreases slightly with increasing temperature owing to collisions between the moving electrons and lattice vibrations (phonons). The main difference in conductor behaviour between metals, semiconductors and insulators is therefore the magnitude of *n* and its temperature dependence:

a) For metals *n* is large and temperature independent. It is μ that determines the σ temperature dependence.

b) For semiconductors and insulators, *n* increases exponentially with the temperature. It outweighs the effect of the small decrease in μ. That is which σ increases with temperature. Insulators and semiconductors are different concerning the value of *n* at room temperature, for insulators it is extremely small.

The differences between different types of conductors concerning their conductivities and their temperature dependences are illustrated in Fig. 2.9.1.1 [30].
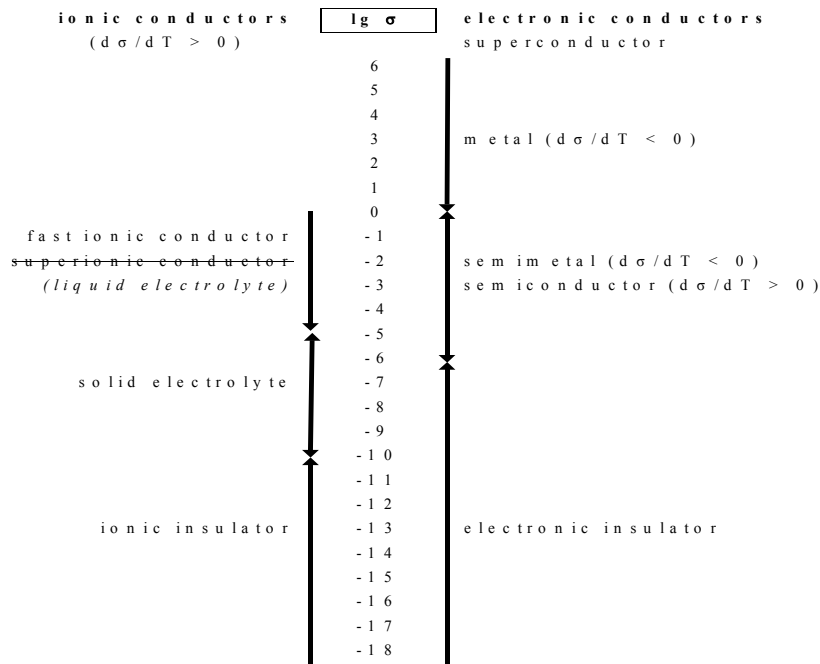
```
ionic conductors        lg  σ      electronic conductors
 ( dσ/dT > 0 )                      superconductor

                          6
                          5
                          4
                          3         metal ( dσ/dT < 0 )
                          2
                          1
                          0
fast ionic conductor     -1
superionic conductor     -2         semimetal ( dσ/dT < 0 )
 (liquid electrolyte)    -3         semiconductor ( dσ/dT > 0 )
                         -4
                         -5
                         -6
solid electrolyte        -7
                         -8
                         -9
                         -10
                         -11
                         -12
ionic insulator          -13        electronic insulator
                         -14
                         -15
                         -16
                         -17
                         -18
```

Fig. 2.9.1.1 Different types of conductors concerning values of their conductivities and their temperature dependences [30]

2.9.1.1 Metals

A metal crystal is a three-dimensional packing of metal atoms which interact with each other. The very dense set of energy states appears there, from the almost equivalent atom orbital of atoms, in consequence of the interaction. It is called energy bands.

For a simple example, we can consider lithium, because it possesses only one valence electron ($2s^1$). When two wave functions interact with one another, the result is one state of higher and another of lower energy. In the same way the interaction between two 2s-orbitals of two lithium atoms leads to two energy levels, one connecting (s), and one anticonnecting ($s^{*)}$. Through combining all 2s-orbitals of all atoms of the lithium crystal, a very dense set of molecular orbitals appears, which extends along the whole crystal. The number of molecular orbitals corresponds to the number of atom orbitals from which they were constructed. Between the energy band built of 1s-atom orbitals and the one of 2s-atom orbitals there exists an energy area with no electron level. Because the electron energies of this area are forbidden, it is called a band gap. The width of the band gap depends on the force of interaction of atom orbitals in the crystal lattice. It is stronger when the distance between atoms is less. If we consider energy bands built from 2s- and 2p-orbitals we can observe an overlap of the 2s- and 2p-bands. The occupation of energy bands obeys the same Pauli principle as for the occupation of atom orbitals. For the metals, the band built from the orbitals of valence

electrons (valence band) almost always overlaps with the next higher band (conduction band). For good electrical conductivity high electron mobility is necessary. It can be achieved either through a valence band that is not completely occupied or a possible transition of electrons from the valence band to the conduction band. Because in the alkali metals the valence band is only half occupied, they would be metallic conductors without the overlap of valence and conduction bands. The alkaline earth metals, on the contrary, have a totally occupied valence band and they could not conduct electrical current without this overlap. The electrons do not belong to one atom any more but can freely move through the whole crystal.

Because there cannot be more than two electrons per orbital, they have some energy also when the temperature is at the absolute zero. The upper energy level which is occupied when the temperature is at the absolute zero, is called the Fermi energy.

The chaotic thermal (Brownian) movement of electrons can be oriented by applying an electrical field. During the oriented electron movement (electrical current) the electrical resistance should be overcome. The definition of electrical resistance (Ohm's Law) is: $R=U/I$, R - electrical resistance $[\Omega]$, U - electrical voltage $[V]$, I - electrical current $[A]$. For the electrical resistivity: $\rho=R \cdot A/l$, A - cross area $[m^2]$, l - length of conductor $[m]$. The definition of conductivity is: $\sigma=1/\rho$, σ=electrical conductivity $[\Omega^{-1}m^{-1}]$, ρ=electrical resistivity $[\Omega\, m]$. With increasing temperature, the kinetic energy of lattice atoms in a metal crystal also increases. Because all the other degrees of freedom are frozen it is converted to vibration energy. The lattice vibrations hinder electrical current without any preferable direction. Therefore part of the electrons is deviated from the direction of flow of the electrical current, and the electrical resistance grows.

2.9.1.2 Insulators

The conduct band of one insulator has no electrons and is separated from the energetically lower valence band, which is totally occupied with electrons, by a wide forbidden zone. In the valence band no conductivity takes place, because there should be free quantum states in order to guarantee electron mobility.

Furthermore no electron can pass through the band gap (which, e.g. for diamond is 5.45 eV wide) in the conduction band. Therefore such solid state bodies do not conduct electrical current.

2.9.1.3 Semiconductors

If the band gap between the totally occupied valence band and the empty conduction band is narrow enough (e.g. silicon has a band gap of 1.1 eV), electron excitation can enable electrons to go over the band gap in the conduction band. The process is called intrinsic semiconductivity and for example thermistors (temperature sensitive resistors) are based on this.

Electron excitation can be brought about not only by thermal energy but also by photon radiation. It is then called photosemiconductivity. In order to pass through the forbidden zone the electrons need a definite amount of energy, ΔE. So the intrinsic conductivity of a semiconductor can be described by the Boltzmann equation: $\sigma = \sigma_0 \cdot e^{-\Delta E/kT}$, σ - conductivity, σ_0 - standard conductivity, ΔE - activation energy, k - Boltzmann constant, T - temperature. After taking the logarithm from both sides of the equation: $\ln \sigma = -\Delta E \cdot 1/kT + \ln \sigma_0$.

If we plot $ln\ \sigma$ as a function of inverse temperature, we receive a straight line, from the slope/gradient of which the band gap ΔE can be calculated.

Apart from the phenomenon of the intrinsic conductivity of semiconductors, a possible extrinsic conductivity is known. For example, if we built arsenic atoms in a crystal lattice of silicon, they have one valence electron more than silicon. This extra electron is weakly connected to an As-atom and could be easier transferred in the conduction band of the crystal than strongly connected valence electrons of silicon atoms. The embedded alien atoms are in this case called "donor" atoms. Their energy level is within the band gap and directly below the conduct band and their activation energy is small. Such types of semiconductors are called n-semiconductors (n for negative, because the charge carriage are negative electrons).

In the case, we take the dopant from the third main group, e.g. indium atoms, which have one valence electron less, then due to substitution of a Si atom by an indium atom one electron less is populating the valence bands. Therefore in the valence band an empty place appears, a defect electron. The indium atoms are called "acceptor" atoms. Their energy levels are slightly above the valence band. By a small addition of energy the electrons from the valence band can go to the acceptor level, thus creating a defect electron conductivity inside the valence band. Such semiconductors are called p-semiconductors (for positive, because the defect electrons have a formally positive charge).

The conductivity of a semiconductor consists of intrinsic and extrinsic contributions. The extrinsic conductivity can be observed at relatively low temperatures, while the intrinsic conductivity is predominant at higher temperatures.

$$\sigma = \sigma_i \cdot e^{-\Delta Ei/kT} + \sigma_e \cdot e^{-\Delta Ee/kT}$$

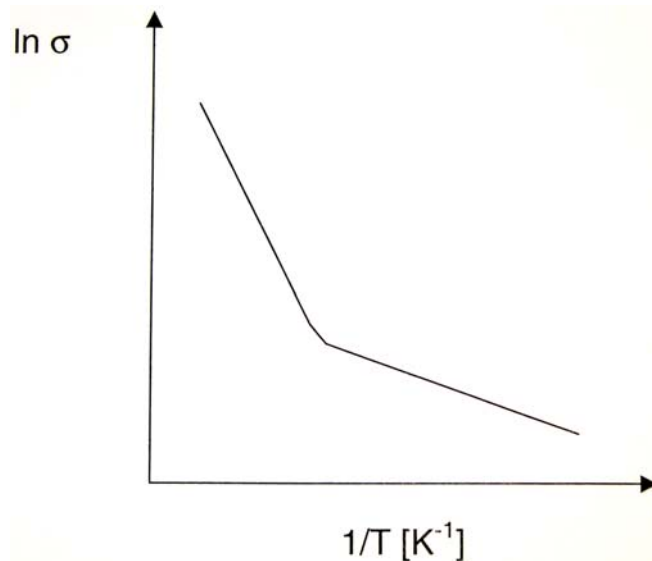(indices *i* and *e* correspond to "intrinsic" and "extrinsic" respectively)

Fig. 2.9.1.3.1 Logarithmic conductivity of a doped semiconductor as a function of inverse temperature [3]

Fig. 2.9.1.3.1 shows the typical curve of the conductivity of a semiconductor [3]. At low temperatures it is influenced mainly by extrinsic conductivity and the slope of the curve is higher. At higher temperatures, the intrinsic conductivity dominates so, the band gap should be calculated at higher temperatures.

2.9.1.4 Semimetals

A semimetal is a conductor whose resistance lies between metal conductor and semiconductors. Its conductivity is (Fig. 2.9.1.1 [30]) very close to that of doped semiconductors but the temperature dependence of their conductivity is metallic: it decreases with rising temperature.

In band theory, semimetals have a similar electronic situation to intrinsic semiconductors: the valence band is completely occupied and the conduction band is empty, but there is a small overlap in the band gap allowing a limited concentration of charge carriers (electrons and defect electrons or holes). The size of the overlap does not depend on the temperature, therefore the concentration of charge carriers is more or less constant, but the resistance increases with the temperature owing to the same mechanism as for metals.

2.9.2 Experimental

In the linear four-probe method the current is flowing through two contacts and the voltage is measured between two other. The resistance of the current contacts is irrelevant, because the measured current is flowing through the sample. And the resistances of voltage contacts are laying together with the inner resistance of the used voltmeter parallel to the resistance of the sample between these contacts. Because the inner resistance is very high the contacts resistances do not influence the measurement at all. The resistivity depends on the sample geometry and in our case (round pellet), it can be calculated: $\rho = R \cdot h \cdot d / a$, h - height of the sample, d - diameter of the sample, a - distance between contacts.

Electronic properties were investigated with a linear four-probe AC low frequency instrument that was recently constructed in our group (scheme of the experiment is shown in Fig. 2.9.2):
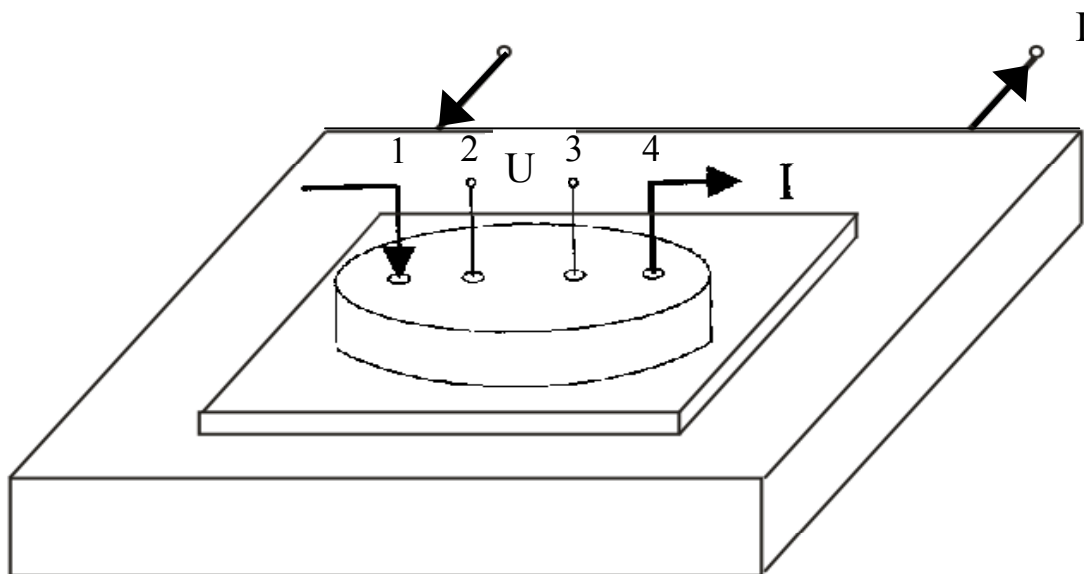

Fig. 2.9.2.1 Schema of conductivity measurement experiment

The current flows through contacts 1 and 4 and the voltage is measured between contacts 2 and 3. The samples were heated with a direct current (current source was Laboratory Power Supply EA-PS 9065-05 from EA-ELEKTRO-AUTOMATIK) going through a heater element (Bach Resistor Ceramics GmbH) (contacts 5 and 6) separated from the pellet with an insulation corundum plate. The temperature is measured with a thermocouple element connected with the Eurotherm controller 2408, which controls the heating current, through the Power Supply. The measurement system (Fig. 2.9.2.1) is closed in a stainless steel housing

together with the thermocouple (Fig. 2.9.2.2 a). The electrical contacts are led out through the flange together with a vacuum output.

The measurements can be carried out under air, argon or vacuum, thanks to the vacuum-argon line which can be connected to the measurement cell. The current supplying and voltage measurements as well as the data registration are made by an impedance spectrometer (Novocontrol GmbH Alpha-A). The whole process of temperature measurement can be done automatically with the help of the measurement computer program WinDeta (Novocontrol GmbH) (Fig. 2.9.2.2 b).
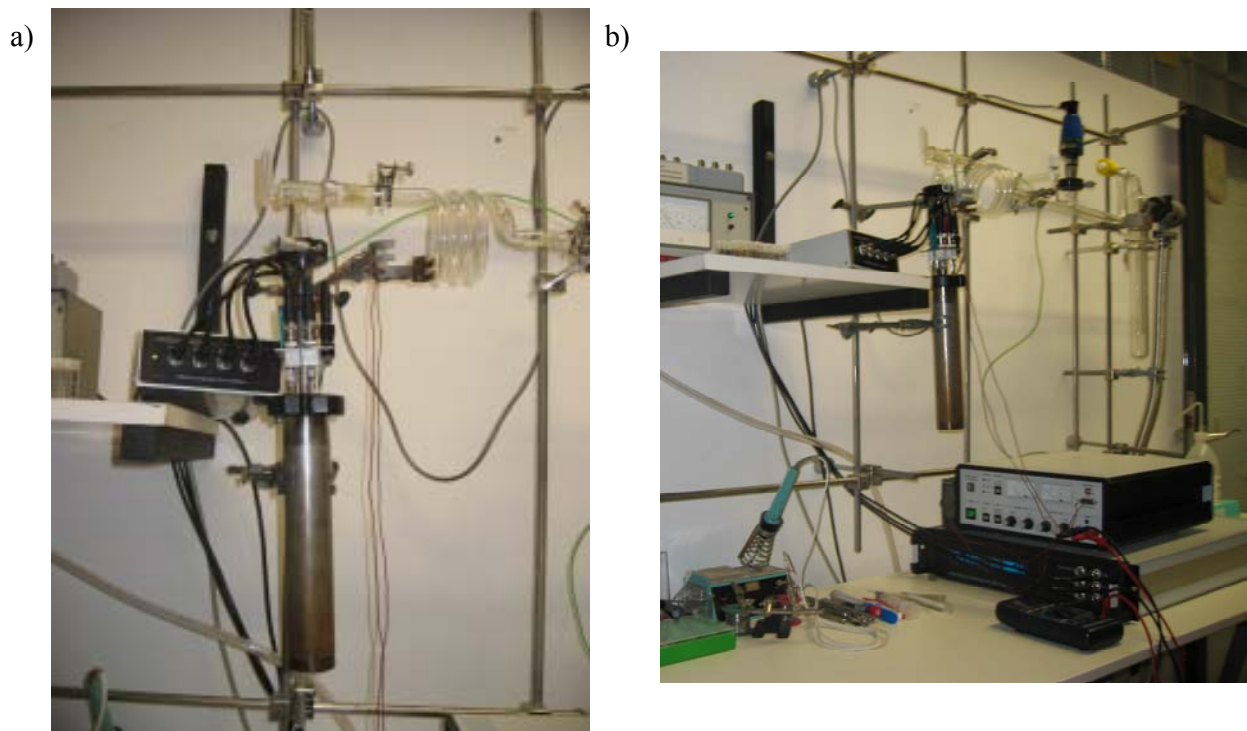
a) b)

Fig. 2.9.2.2 Photos of the experimental plant: a) Measurement cell connected to the impedance spectrometer and the vacuum-argon line b) the experimental plant as whole

2.10 Magnetic measurements

2.10.1 Magnetic phenomena

Inorganic solids which interact with a magnetic field usually have unpaired electrons. We should therefore speak, about spins. The solids can be divided into several groups (Fig. 2.10.1.1 [13]).
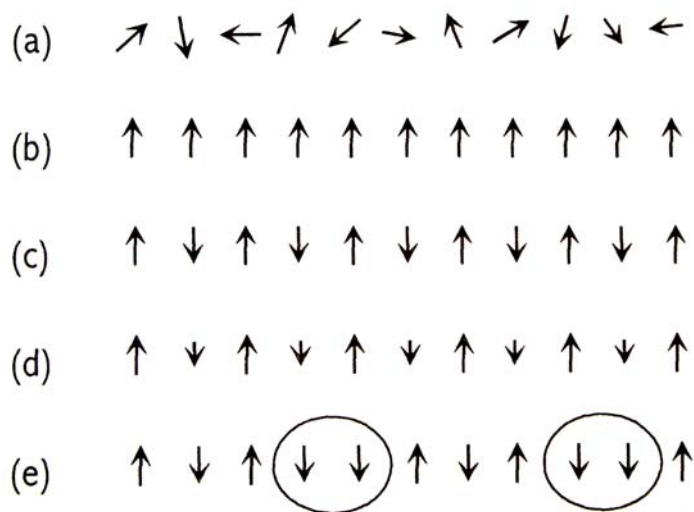

Fig. 2.10.1.1 Schematic magnetic phenomena in a 1D crystal: (a) paramagnetism; (b) ferromagnetism; (c) antiferromagnetism; (d) ferrimagnetism; (e) spin glass-type behavior when an antiferromagnetic array is disrupted or frustrated by enforced ferromagnetic coupling (circled) [13]

Spins can be oriented randomly, the material is paramagnetic (a). They can also interact with each other and create cooperative magnetic effects. When all of them are oriented in parallel, the material has an overall magnetic moment and is ferromagnetic (b). They can be aligned antiparallel, the overall magnetic moment is zero and the material is antiferromagnetic (c). If the alignment is antiparallel but we have more spins in one direction than in the other, the overall magnetic moment is not zero and the material is ferromagnetic (d). A special case is constituted by antiferromagnets with spin glass-like behavior (e). In this case, there is a natural cooperative interaction between neighboring spins which leads to antiferromagnetism, but is not able to develop a long-range antiferromagnetic structure, the "spin up-spin down" arrangement becomes frustrated by the frequent occurrence of unavoidable "spin up-spin up" ("spin down-spin down") ferromagnetic pairs.

In the presence of an external magnetic field all materials interact with it. Mainly two effects are distinguished: diamagnetism, when the induced magnetic field of the material is directed in the opposite direction compared with the external field, and paramagnetism, when the direction of the internal, induced field is the same as that of the external field. One speaks of the material being magnetized.

When the external magnetic field, **H**, is applied the relation with the internal field (magnetic induction), **B**, could be described: **B**=**H**+4π**M**, **M** - magnetic moment per unit volume. Permeability, *P*, and susceptibility, *K*, are thus defined: P=**B**/**H**=1+4πK, K=**M**/**H**. Molar susceptibility, χ, is given by: χ=KF/ρ, where *F* is the formula weight and ρ the density of the material.

The molar susceptibility is the main parameter that is usually considered to characterize magnetic properties of materials and is a measure of their response to the externally applied magnetic field, see table 2.10.1.1 [13]:

Behavior	Typical χ value	Change of χ with increasing temperature	Field dependence
Diamagnetism	-8×10^{-6} for Cu	None	No
Paramagnetism		Decreases	No
Pauli paramagnetism	8.3×10^{-4} for Mn	None	No
Ferromagnetism	5×10^{3} for Fe	Decreases	Yes
Antiferromagnetism	0 to 10^{-2}	Increases	(Yes)

Table 2.10.1.1 Magnetic susceptibilities [13]

As we can see, the different kinds of magnetic behavior can be distinguished by the values of χ and its temperature and field dependences. For diamagnetic materials, χ is very small and negative. For paramagnetic materials, it is also small and positive. Fig. 2.10.1.2 [13] shows that for an external magnetic field its density in samples is greater for paramagnetic and slightly less for diamagnetic materials, than in vacuum. Paramagnetic materials are attracted by an external magnetic field, whereas diamagnetic ones show a slight repulsion. Only superconductors have ideal diamagnetism, when χ=-1 and the magnetic field is completely expelled. Ferromagnetic materials, where χ>>1, are strongly attracted to an external magnetic field. In antiferromagnetic materials, χ is positive and about the same or smaller than in paramagnetic materials.

When the temperature changes, the molar susceptibility of a lot of paramagnetic materials follows the simple Curie law, especially at high temperatures, that magnetic susceptibility is inversely proportional to temperature:

$$\chi = C/T$$

Where C is the Curie constant. Such dependence occurs when there is no spontaneous interaction between spins. They do tend to align in a magnetic field, but with increasing temperature it becomes more difficult and the susceptibility decreases.

If there is some spontaneous interaction between neighboring spins, which may develop into ferro- or antiferromagnetism at low temperatures, the susceptibility dependence can be described by the Curie-Weiss law:

$$\chi = C/(T-\theta)$$

where θ is the Weiss constant. Both kinds of behavior are illustrated in Fig. 2.10.1.3 [13], where χ^{-1} is plotted as a function of temperature.
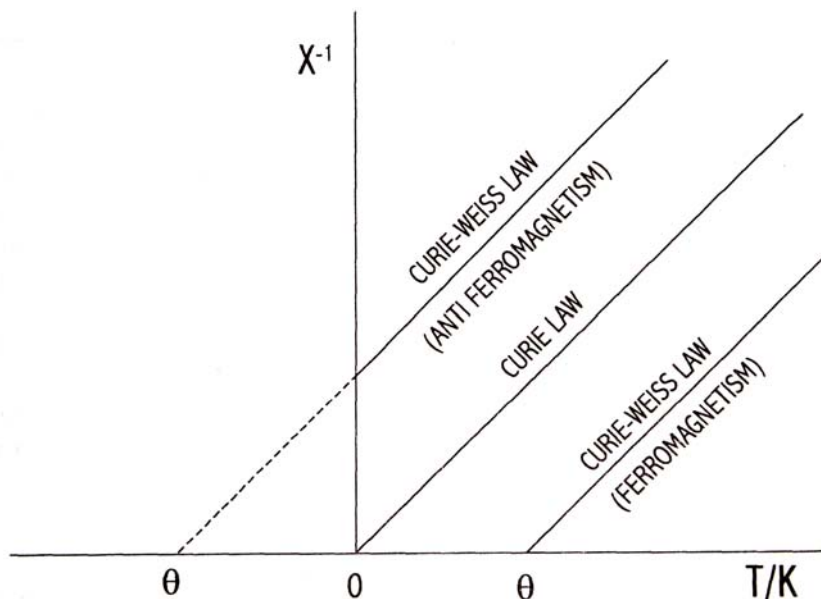

Fig. 2.10.1.3 Plot of reciprocal susceptibility against temperature for substances that are paramagnetic but may show magnetic ordering at low temperatures [13]

For paramagnetic materials that show no tendency towards magnetic order, the plot extrapolates to 0 K. For paramagnetic substances that do tend towards ferromagnetic alignment of spins, χ is greater than for simply paramagnetic materials. It becomes infinite ($\chi^{-1} \to 0$) at a positive value of θ, which is called the ferromagnetic Curie temperature, T_c, below which the material is ferromagnetic.

If paramagnetic substances have a tendency towards antiferromagnetic alignment of spins, χ is smaller than for simple paramagnetic materials. The Curie-Weiss plot is moved to lower temperatures and the extrapolated value of θ is below 0 K. But the plot is not so ideal, such materials have a Neel temperature, T_N, below which a departure from Curie-Weiss law takes place. An example of the Curie and Neel temperatures for some transition metals are shown in table 2.10.1.2 [13].

Material	T_c (°C)	T_N (°C)
Cr		35
Mn		-173
Fe	770	
Co	1121	
Ni	358	

Table 2.10.1.2 Some Curie and Neel temperatures [13]

Another way to characterize magnetic materials is to investigate the dependence of the magnetic moment (magnetization of sample), **M**, on the external magnetic field, **B**. With increasing intensity of **B**, **M** increases also, up to a maximum possible value, **M_s**, after which it does not depend on increasing **B** any more. If we start to decrease **B**, **M** decreases also but slowly as it increased before, and it is not equal to zero when there is not **B** intensity any more. This is an effect of permanent magnetization. In order to remove it we should apply **B** in the opposite direction, -**B**, the value of demagnetizing the external field which we need to remove the permanent magnetization called coercivity, **B_c**. If we continue to increase **B** further in this direction, the magnetization will re-appear with an opposite orientation. If we repeat the procedure several times we can describe it with a closed loop called hysteresis-loop (Fig. 2.10.1.4 [31]).
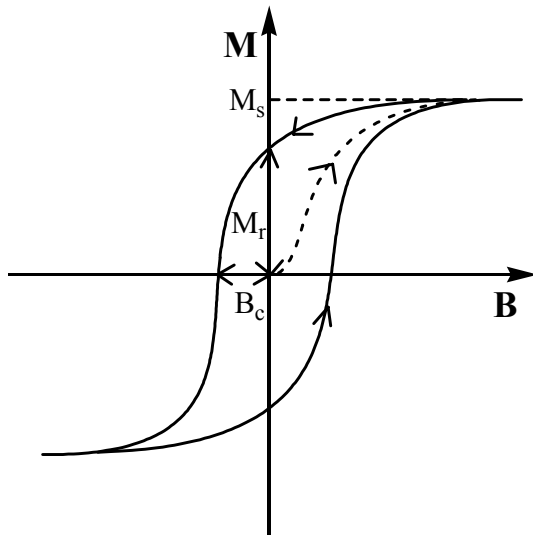
Fig. 2.10.1.4 Typical hysteresis-loop of a ferromagnetic material and the most important parameters [31]

The explanation of hysteresis is a domain structure of macroscopic ferromagnetic materials. The material consists of magnetic domains oriented in antiparallel which are separated from each other by a Bloch wall [31]. Within a domain all spins are oriented in parallel. In the absence of an external magnetic field the overall magnetization is zero. After reaching maximal (saturation) magnetization, when all domains are oriented in one direction, they cannot, in the absence of an external field, reorient themselves: this is the reason for permanent magnetization.

2.10.2 Nanomagnetism

The spin (domain) structure of a nanoparticle strongly depends on the particle size, it leads to magnetic behavior depending on particle size [31]. With decreasing particle size, the number of domains in it also decreases (M_s, M_r and B_c change). Below a critical size, the formation of separate domains is not energetically advantageous any more and the particle consists of only one domain [31]. This critical size depends on the material, and varies from 14 nm for Fe to 170 nm for γ-Fe_2O_3 [33].

Another effect which can be observed, that the susceptibility differs when measured in different directions, is called magnetic anisotropy. This can be caused by the orientation of the crystal lattice or the macroscopic shape of the magnetic material under consideration [31]. Anisotropy is a very important parameter which strongly influences the behavior of a magnetic material. When the material is magnetically anisotropic, the overall magnetization

of the considered system lies along a special direction; this direction is called the "easy axis of magnetization" [31].

For one-domain particles the energy connected with this effect is called anisotropy energy, E_a, which can, in a one-axis approximation, be described as:

$$E_a = KV \sin^2\theta$$

where:

K - anisotropy constant

V - particle volume

Θ - angle between the easy axis of magnetization and the moment of magnetization

When an external magnetic field, **B**, is applied to such a particle, there is a potential energy, E_f.

$$E_f = -\mathbf{M_s} \cdot \mathbf{B}$$

where:

$\mathbf{M_s}$ - saturation magnetization

The influence of the magnetic field on the magnetic moment of particles depends on the angle between the easy axis of magnetization and the magnetic field (Fig. 2.10.2.1 [33]).
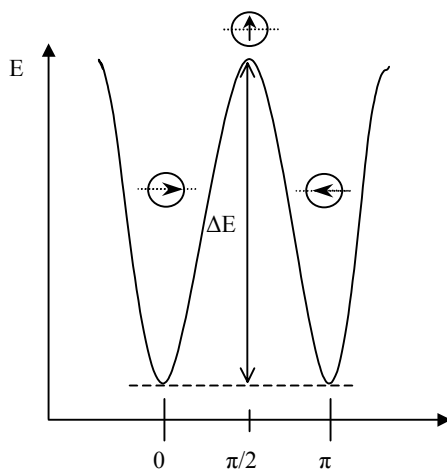

Fig. 2.10.2.1 Anisotropy energy as a function of the angle between the easy axis of magnetization and the moment of magnetization for particles with one easy axis. The minimum relates to magnetization along the easy axis, ΔE is an energy barrier of a rotation of the magnetization [33]

The next picture shows the dependence of potential energy on the power of an external magnetic field in two directions (horizontal and vertical) (Fig. 2.10.2.2 [31]).

a   Magnetfeld
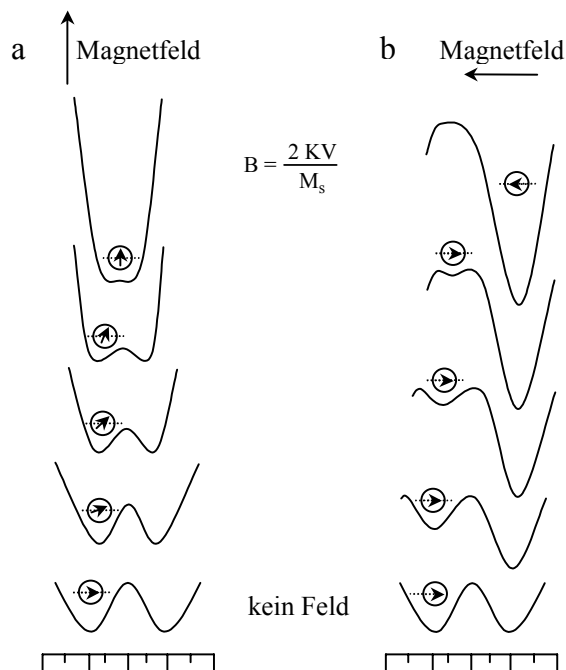
$B = \dfrac{2\,KV}{M_s}$

b   Magnetfeld

kein Feld

Fig. 2.10.2.2 Dependence of the potential energy on the direction of the magnetic moment of a particle in the presence of an external magnetic field which runs a) horizontally and b) vertically to the easy axis of magnetization. Lower plots relate to the intensity of a magnetic field = 0, upper plots to saturation magnetization, when magnetic moments lie along the field [31]

The total energy E_t, equals $E_t = E_a + E_f$.

The equilibrium direction (which relates to the minimum of E_t) changes relating to fields, until it lies along the external magnetic field and magnetization reaches saturation (a). Or it runs along the antiparallel axis and when the field is strong enough, it springs into parallel with the field direction (b). This happens at:

B=2KV/M_s

Therefore the behavior of a one-domain particle depends on the direction of the external magnetic field. In reality the easy axes of magnetization are randomly oriented (Fig. 2.10.2.3 [31]).
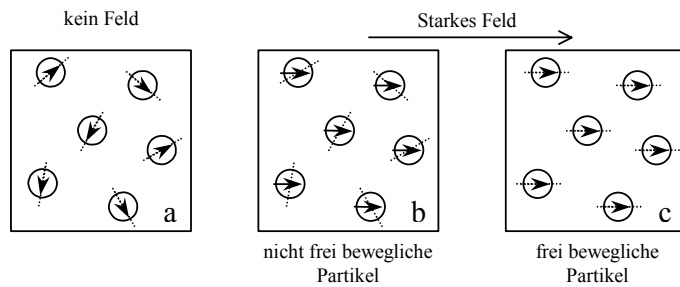
Fig. 2.10.2.3 (a) Set of magnetic nanoparticles with randomly oriented easy axes of magnetization. (b) Magnetization of the set of magnetic nanoparticles through orientation of magnetic moments in the external magnetic field. (c) Magnetic nanoparticles in a solution can orient their easy axes along the external magnetic field [31]

In a very strong magnetic field all the particles orient their magnetic moment along the field and thus reach saturation magnetization. When all the particles are dispersed in a non-magnetic matrix, their easy axes of magnetization are randomly oriented and saturation magnetization will be reached through rotation of magnetic moments. The time necessary for this is in the region of 10^{-9} c [31]. The particles in the solution can do the same by simple reorientation of their easy axes at much lower energy [31].

Thermal fluctuations also influence the behavior of magnetic nanoparticles when there is no external field. The energy barrier, ΔE, must be overcome in order to change the orientation of a particle. The height of the barrier is proportional to the particle volume:

$$\Delta E = KV$$

With decreasing particle size ΔE can also decrease, so that it will be comparable to thermal energy, E_{th}, [31].

$$E_{th} = k_B T$$

After that, the energy barrier cannot fix the magnetic moment in one direction any more and it rotates following thermal fluctuations. A particle in this state is super-paramagnetic. The coercivity, **B_c**, of such particles is zero because thermal fluctuations do not admit any stable magnetization. The cooling of super-paramagnetic particles reduces the energy of thermal fluctuations and below some definite temperature the anisotropy prevents the free rotation of the magnetic moment. The temperature of transition from the super-paramagnetic to the ferromagnetic state is called blocking temperature and depends on the particle volume and the anisotropy constant.

The coercivity of a magnetic nanoparticle depends strongly on its size. If a particle is big enough for a multidomain structure, magnetization takes place through a movement of domain walls. Because this is relatively easy the coercivity is low. For a one-domain particle a

change of direction of magnetization can happen only through the simultaneous rotation of all spins, which leads to very high coercivity compared with the multidomain particle. When the particle size is further decreased, coercivity decreases also because the influence of thermal fluctuation is increased, which leads at last to super-paramagnetism (B_c=0) (Fig. 2.10.2.4 [32]).
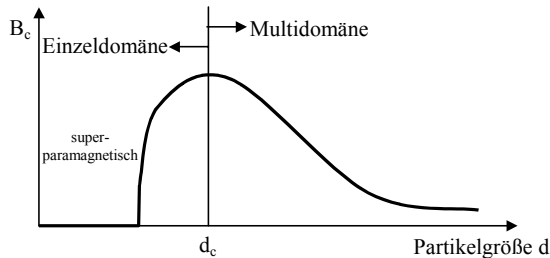
Fig. 2.10.2.4 Coercivity of a magnetic nanoparticle as a function of its size- maximum coercivity is observed at the size of transition from multidomain to one-domain structure [32]

2.10.3 Experiment

In order to detect the magnetic properties of materials, there are a number of important methods, for example, magnetic balances (Gouy, Faraday) or SQUID (superconducting quantum interference device). In this work a SQUID Magnetometer (Quantum Design Inc.) was used, measurements were done in the temperature range 5-300 K, at the MPI Stuttgart, in the group of Prof. Dr. M. Jansen.

The SQUID can measure extremely weak signals. In conjunction with a device called a Josephson junction, a SQUID can detect a change of electromagnetic energy as low as 100 billion times weaker than, for example, the energy that moves a compass needle. A Josephson junction consists of two superconductors, separated by an insulating layer, which is so thin that electrons can pass through it. The special properties of the Josephson junction cause the impedance of the SQUID loop to be a periodic function of the magnetic flux threading the SQUID so that a modulation signal supplied to the bias current is used with a lock-in detector to measure the impedance and to linearize the voltage-to-flux relationship. The net result is that a SQUID functions as a flux-to-voltage converter with unrivaled energy sensitivity [38]. SQUIDs are usually made of either a lead alloy (with 10% gold or indium) and/or niobium, often consisting of tunnel barrier sandwiches between the base electrode of niobium and the top electrode of lead alloy.

There are two types:

A radio frequency (RF) SQUID is made up of only one Josephson junction, which is mounted on a superconducting ring. An oscillating current is applied to an external circuit whose voltage changes as an effect of the interaction between it and the ring. The magnetic flux is then measured.

A direct current (DC) SQUID, which is much more sensitive, consists of two Josephson junctions employed in parallel so that electrons tunneling through the junctions experience quantum interference dependent upon the strength of the magnetic field within a loop. DC SQUIDs show resistance in response to even tiny variations in a magnetic field, which is the capacity that enables detection of such minute changes [39].

3 Investigations and results

3.1 Alkaline earth metal hexaborides

3.1.1 State of research

As it was already mentioned in Chapter 1.2 there are different opinions on the electronic situation of alkaline earth metal hexaborides among both theoretical and experimental scientists.

The first theoretical calculations of Longuet-Higgins and de V. Roberts predicted a semiconducting behavior for divalent hexaborides, suggesting a transfer of two valence electrons from a metal atom to a B-octahedron [49]. A little later Perkins calculated that the transfer of a single electron to the B-octahedron is enough to stabilize the B-lattice [56]. Hasegawa and Yanase did a bond structure calculation in the Muffin-Tin approximation and found semi-metal behavior, but without the Muffin-Tin approximation they found a small band gap. The calculations were based on the structure model with equidistant intra- and interoctahedron B-B distances [51]. Massidda et al. did bond structure calculations for CaB_6 and SrB_6 using the FLAPW-method (full-potential linearized augmented plane wave) [52]. The basis of their calculations was a structure model that had been energy-optimized by changing the lattice parameters a and the position of parameter z. Calculated values of a and z were very similar to experimentally determined data. The authors explored the dependence of calculated band gaps on values of the position of parameter z and they found semiconductor behavior for $z > 0.206$, whereas a semimetal state was calculated for $z < 0.206$.

Stackelberg and Neumann carried out the first experiments on powder samples of CaB_6 and described the compound as a metallic conductor [41]. Johnson and Daane have received by DC four contact measurements on a SrB_6 single crystal a band gap of 0.38 eV [57]. The experiment was done in a temperature range from 725 to 1185ºC. The single crystals were grown in a two-zone oven (1650ºC and 1800ºC) with excess of strontium in tantalum ampoules. For investigations of CaB_6 and BaB_6 powder samples were prepared, which contained elemental boron as an impurity. For CaB_6 a band gap of 0.4 eV was found (temperature range 700 - 1670ºC), for BaB_6 0.12 eV (temperature range 530 - 1430ºC). Ott et al. investigated the temperature dependence of electrical conductivity of SrB_6 single crystals between -267ºC and 27ºC [46]. Above -23ºC metallic conductivity was found, between -253ºC and -23ºC semiconductor behavior, and below -253ºC metallic conductivity again.

Bandgap values for the semiconductor range were not published. In recent years, high temperature ferromagnetism was observed in CaB_6 [58], but later had to be assigned to an impurity phase [59]. A very interesting paper is one of the most recent ones of Rhyee, Oh and et al., where the authors [60] compared pure CaB_6 single crystals, synthesized with 99.9999 %-pure boron, which exhibited fully semiconducting characteristics, such as monotonic resistance for -271ºC - 27ºC, a tunnelling conductance gap, and an optical absorption threshold at 1.0 eV, with CaB_6 single crystals synthesized with 99.9 %-pure boron, where boron-related defects induced mid-gap states 0.18 eV below the conduction band and extra free charge carriers, with the transport, optical, and tunnelling properties substantially modified. Remarkably, no ferromagnetic signals were detected from single crystals made with 99.9999 %-pure boron, regardless of stoichiometry, whereas those made with 99.9 %-boron exhibited ferromagnetism within a finite range of carrier d.

In 2002, Denlinger et al. again described SrB_6 as a semiconductor [61]. According to our own investigations, BaB_6 is also a semiconductor [62].

As described above, the electronic situation of divalent hexaborides is not properly understood. The conductivity behavior is assumed to be easily affected by nature and concentrations of impurities. The aim of this work is to synthesize SrB_6 and CaB_6 of a controllable purity/dopant status, to characterize them and to investigate their conductivity properties as a function of nature and concentrations of impurities/dopants.

3.1.2 Synthesis of alkaline earth metal hexaborides

The synthesis was carried out from the elements: boron (Chempur, 99.9 %) and strontium or calcium (Alfa Aesar 99.95 %). For some of the reactions strontium and calcium was additionally distilled prior to use (Fig. 3.1.2.1).

a)

b)

Water cooler

Flange

Vacuum connection

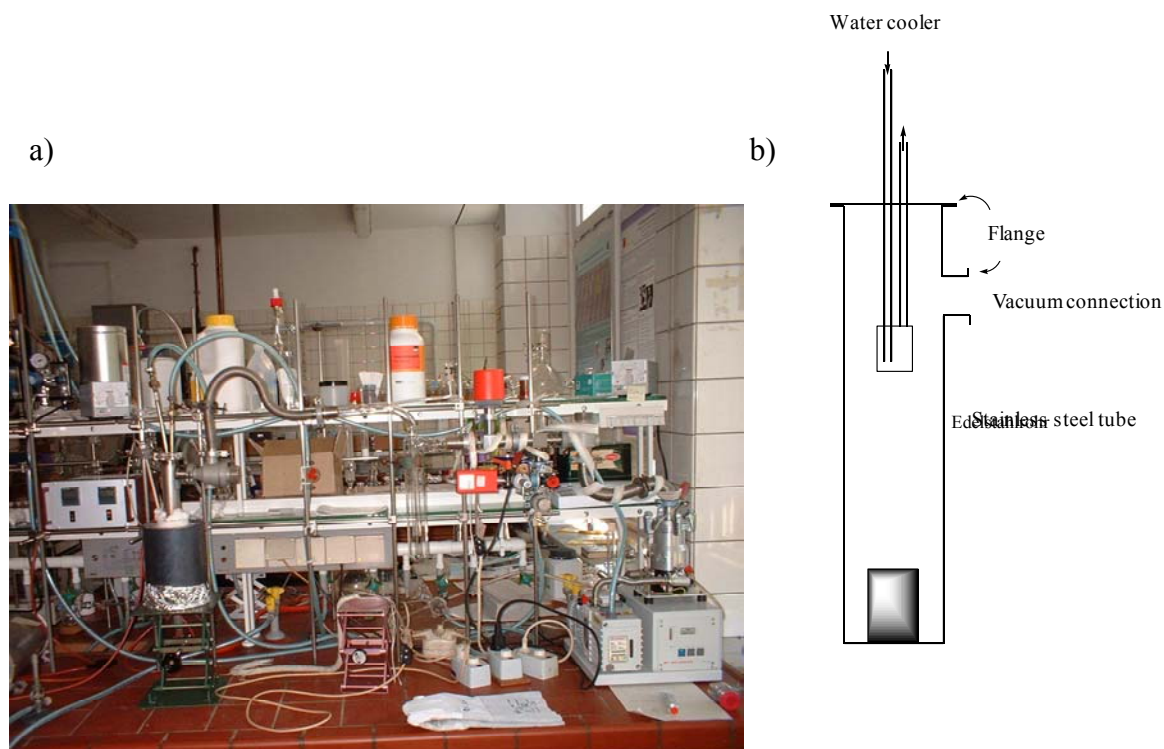Edelstahlrohr Stainless steel tube

Fig. 3.1.2.1 Distillation setup, photo (a) and scheme (b)

As reaction mixture the molar ratio of Sr/Ca:B was chosen to be 1:4, as it was found to be optimal due to the loss of metal during synthesis [3]. Tantalum crucibles were prepared as described in Chapter 2.2. The elements were weighted, intimately mixed, put in a tantalum crucible under argon in a glove-box, and vacuum tight closed using a grip vise. Then they were vacuum tight welded in the arc-melting setup. The crucible was put in a quartz ampoule, which was melted off under vacuum using the vacuum-argon line. After this preparation it was heated to 1050 ºC for 48 hours in an oven. After the synthesis the crucible was opened in a glove-box under argon. The reaction product was washed under air-free conditions, using standard schlenk techniques, with degassed, distilled hydrochloric acid in order to remove any excess of strontium/calcium and possible impurities such as metals or strontium/calcium oxide. Finally the product was washed with distilled water and vacuum dried (150 ºC, 24 hours).

After that it was handled under air.

The reference samples were: CaB_6 (Alfa Aesar, 99.5 %), SrB_6 (Alfa Aesar, 99.5 %), $CaBr_2$ (Merck, 99 %), CaC_2 (Roth, 99 %), $CaCl_2 \cdot 6H_2O$ (Merck, 96 %), $CaCO_3$ (Merck, 99 %), CaF_2 (Merck, 99 %), SrB_6 (Alfa Aesar, 99.5 %), $SrBr_2$ (Schuchardt, 99 %), $SrCl_2 \cdot 6H_2O$ (Merck, 96 %), $Sr(NO_3)_2$ (Merck, 99 %).

3.1.3 Characterization of alkaline earth metal hexaborides

3.1.3.1 Scanning Electron Microscopy

Scanning electron microscopy (SEM), carried out for three samples of CaB_6 (samples CaB_6-1, CaB_6-2, CaB_6-3) and two of SrB_6 (samples SrB_6-1, SrB_6-3), confirmed the cubic shape [35, 39] of the microcrystals for all of them, a typical example is shown on Fig. 3.1.3.1.1. While if the microcrystals of CaB_6 reach to normally only 0.5-1 μm size, SrB_6 crystals generally were larger, their size can achieve 3 μm.
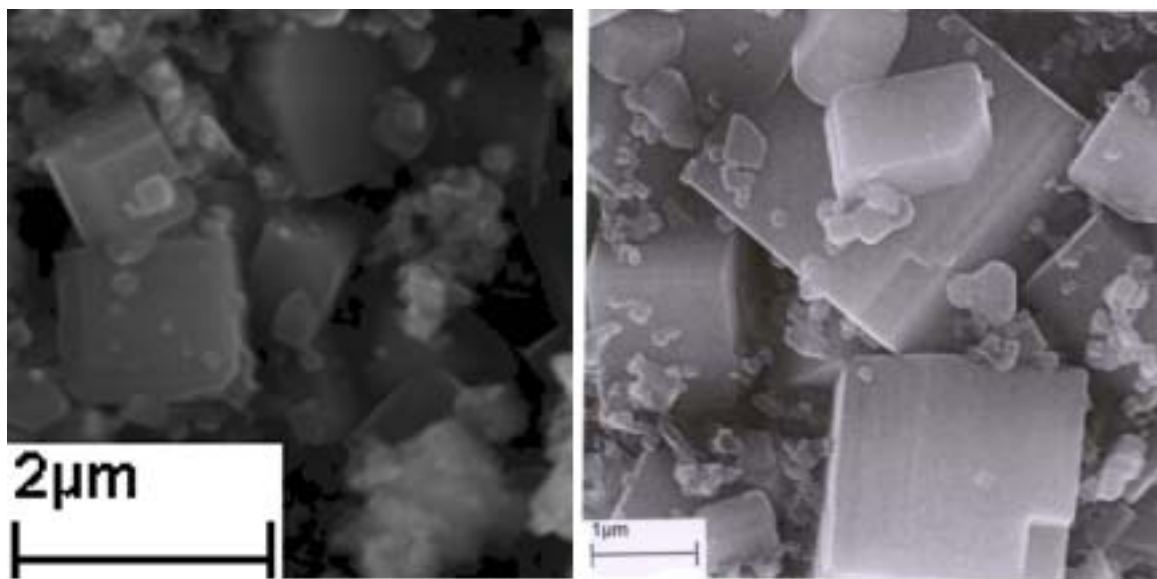
Fig. 3.1.3.1.1 SEM image of CaB_6 (CaB_6-1, left) and SrB_6 (SrB_6-1, right) microcrystals

3.1.3.2 Electron Energy Loss Spectroscopy

Electron energy loss spectroscopy (EELS) was used to identify impurities in the detectable concentration range. For samples CaB_6-1, CaB_6-2, SrB_6-1, SrB_6-3 the metals (Ca or Sr for CaB_6 or SrB_6 respectively), boron and traces of oxygen were detected.

The same samples were used for investigation of the correlation between the boron framework and the fine structure of boron k-edge in EEL spectra [64, 65]. For the same boron units (octahedra) a very similar fine structure of boron K-edges in the energy loss spectra is observed (Fig. 3.1.3.2.1).
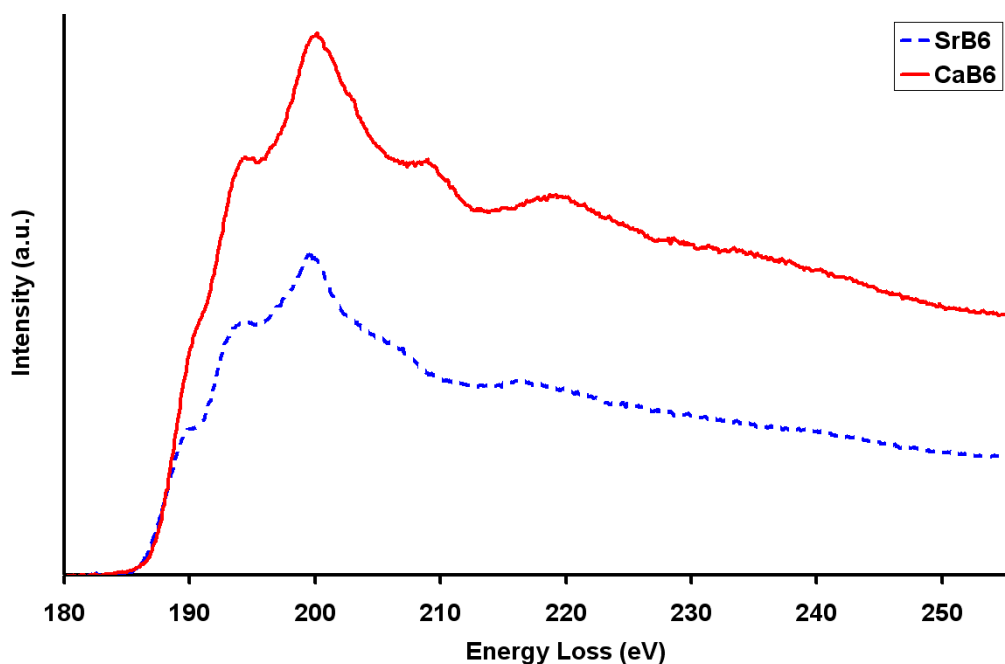
Fig. 3.1.3.2.1 Fine structures the boron K-edges of CaB_6 and SrB_6

Since the shapes of the boron K-edge fine structures are almost identical for both compounds investigated here, these fine structures can possibly serve as references for this boron framework in other borides.

3.1.3.3 Energy Dispersive X-ray Spectroscopy

Additionally the same samples (CaB_6-1, CaB_6-2, SrB_6-1, SrB_6-3) together with LaB_6 as reference were studied with energy dispersive X-ray spectroscopy (EDX). No impurities except traces of oxygen (which are always observed) were detected.

The metal/boron ratio was calculated from the areas below the corresponding peaks. In the table 3.1.3.3.1 the result in normalised units for measured samples and reference LaB_6 can be seen.

Sample	B, norm. unit	Metal, norm. unit	Ratio B:M
LaB_6	69.35	11.82	5.87
CaB_6-1	75.92	13.22	5.74
CaB_6-2	83.30	13.93	5.98
SrB_6-1	53.85	9.64	5.59
SrB_6-3	31.81	5.53	5.75

Table 3.1.3.3.1 Measured areas for of boron and metal peaks and their ratio

For all the measured samples of CaB_6 and SrB_6 as well as for the LaB_6 reference sample the B/M ratio was quite close to six. On the fig. 3.1.5.1 the example of typical EDX spectra of one of our samples can be seen. The spectrum shows no impurities besides the traces of oxygen in the area at around 0.5 keV.
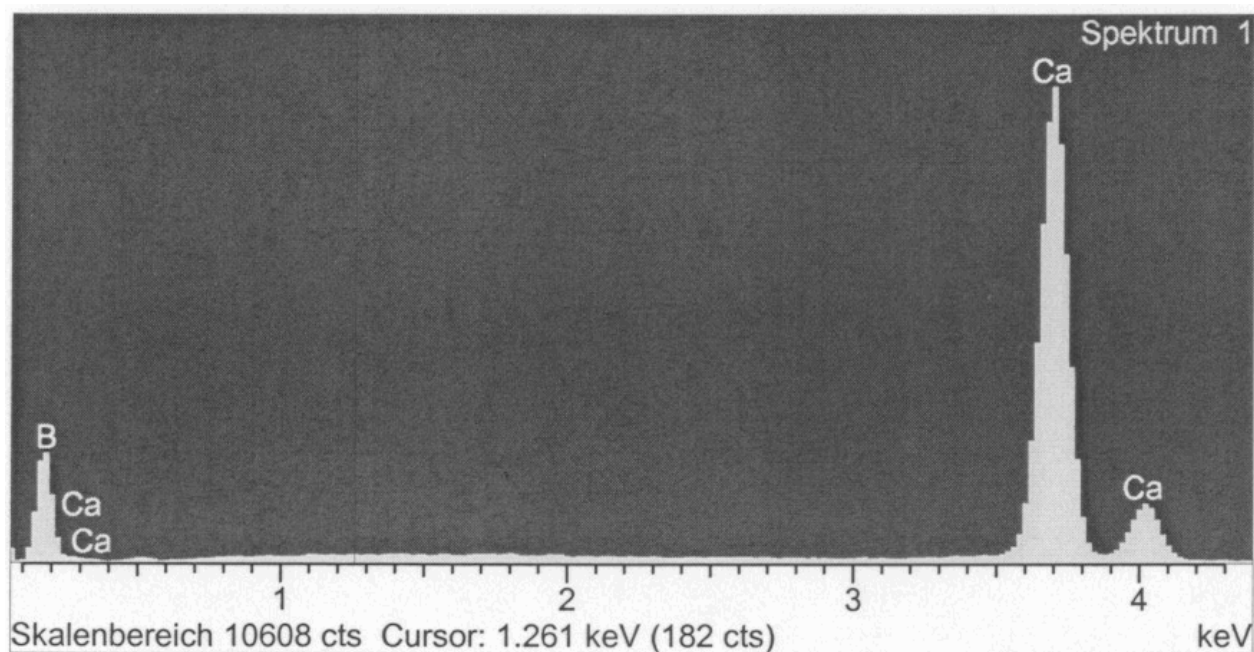

Fig. 3.1.3.3.1 EDX spectrum of CaB_6-1

3.1.3.4 X-ray Absorption Spectroscopy

With help of X-ray absorption near edge structure spectroscopy the k-edge position of metal (in our case Ca or Sr) which correlates with the respective oxidation state can be measured and compared with the K-edge positions of references with known oxidation states. Some of the samples were measured several times. As can be seen in Table 3.1.3.4.1-2 below the K-edge positions of all the samples are similar to the K-edge positions of the references. The examples of K-edges of samples CaB_6-2 and SrB_6-3, compared to references $CaCO_3$ and respectively $Sr(NO_3)_2$, are shown in figures 3.1.3.4.1 and 3.1.3.4.2. It can be concluded that CaB_6 and SrB_6 have similar oxidation state as the references, +2. (Fig. 3.1.3.4.1).

Sample	k-edge position, eV	Known oxidation State
CaB_6-1-1	4041.01	
CaB_6-1-2	4041.01	
CaB_6-2-1	4040.99	
CaB_6-2-2	4040.84	
CaB_6-2-3	4040.00	
$CaBr_2$	4040.49	+2
CaC_2	4040.47	+2
$CaCl_2 \cdot 6H_2O$	4040.61	+2
$CaCO_3$	4040.91	+2
CaF_2	4040.92	+2

Sample	k-edge position, eV	Known oxidation State
SrB_6-1-1	16112.79	
SrB_6-3-1	16112.22	
SrB_6-3-2	16112.71	
$SrBr_2$	16112.95	+2
$SrCl_2 \cdot 6H_2O$	16111.93	+2
$Sr(NO_3)_2$	16113.67	+2

Table 3.1.3.4.1-2 K-edge position of Ca and Sr in measured samples and reference substances and related oxidation states of references
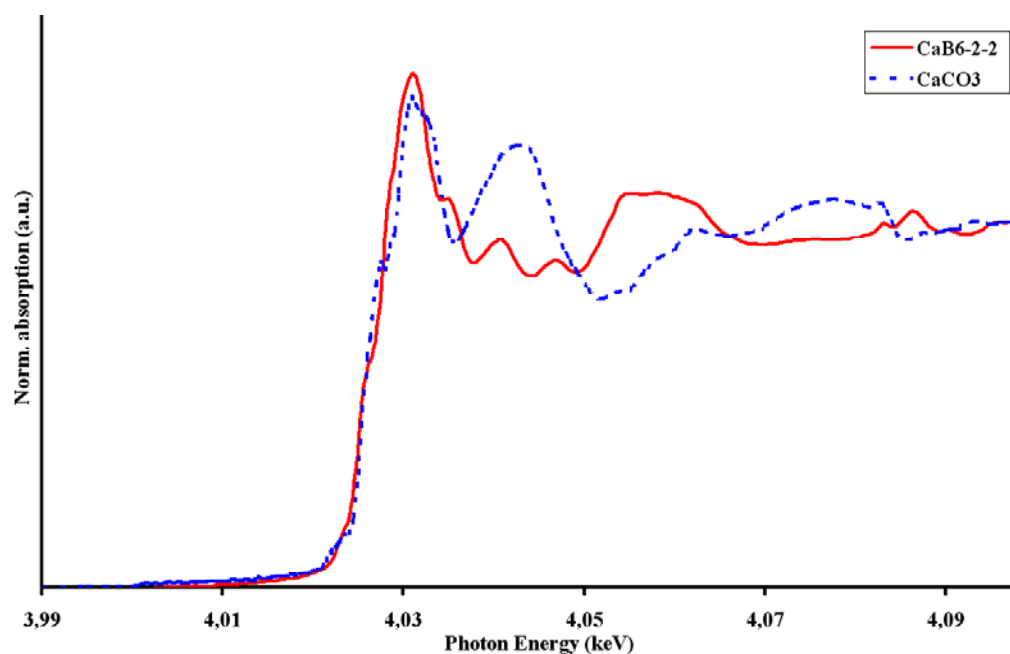

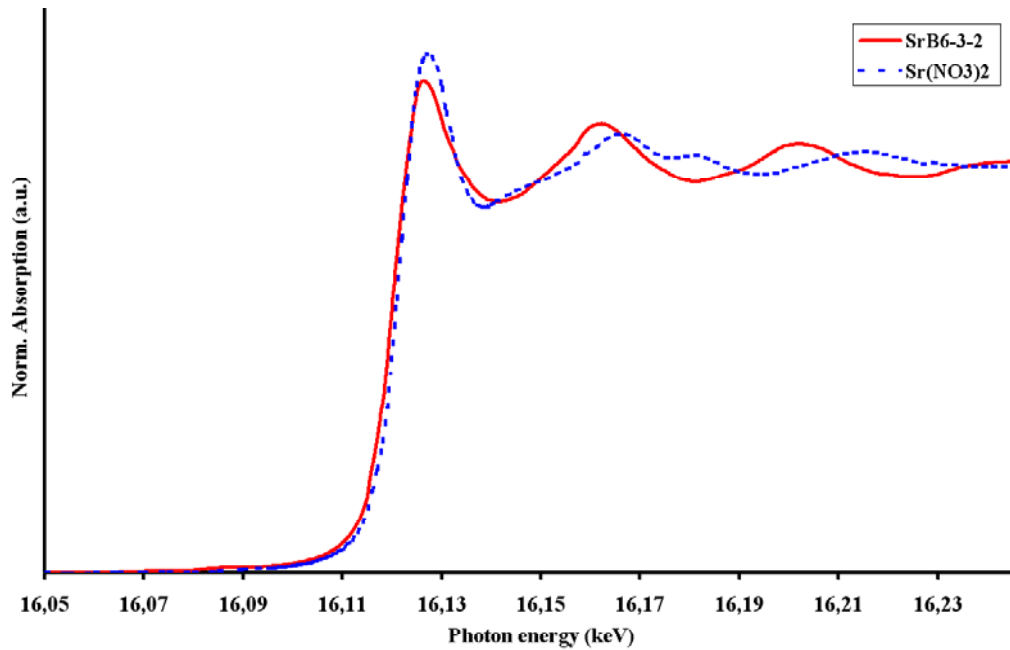Fig. 3.1.3.4.1 K-edge of CaB_6-2 compared with $CaCO_3$

Fig. 3.1.3.4.2 K-edge of SrB_6-3 compared with $Sr(NO_3)_2$

3.1.3.5 X-Ray Diffractometry

The X-ray diffractometry (XRD) patterns of all samples prepared in the course of this work perfectly fit with the theoretical patterns [46, 101], calculated from single crystal data, and confirm the identity of our samples. No crystalline impurities can be observed. The two examples of samples CaB_6-2 and SrB_6-3, together with the theoretical pattern, are shown on the Fig. 3.1.3.5.1, Fig. 3.1.3.5.2
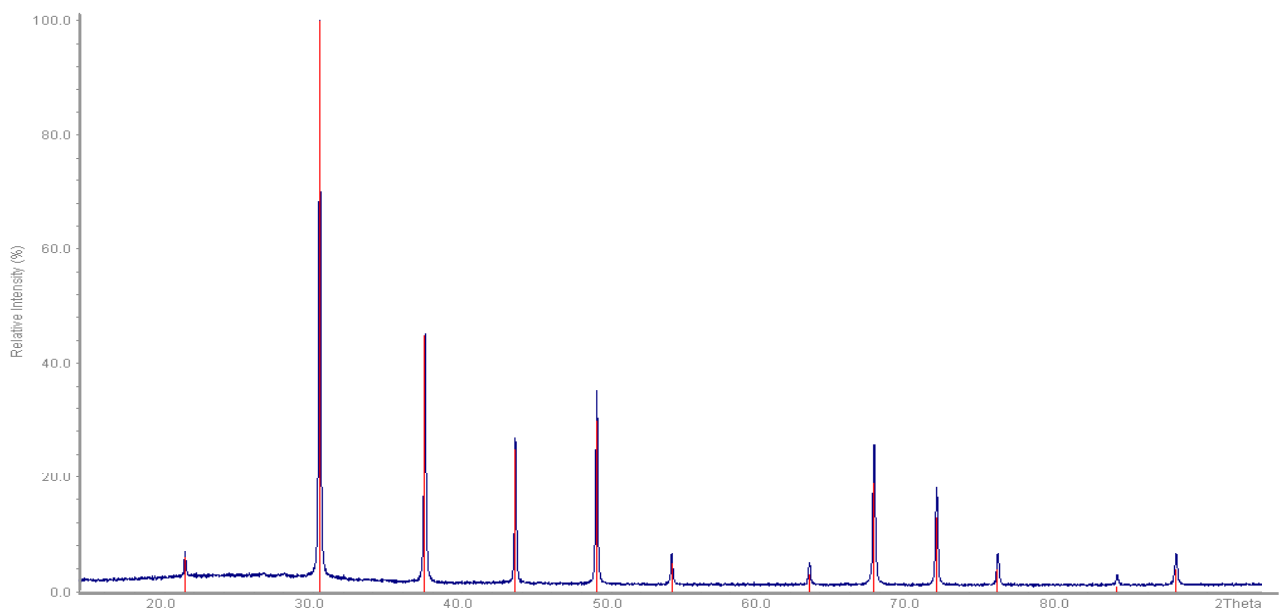

Fig. 3.1.3.5.1 XRD pattern (blue) CaB_6-2 with the theoretical pattern [101] (red lines)
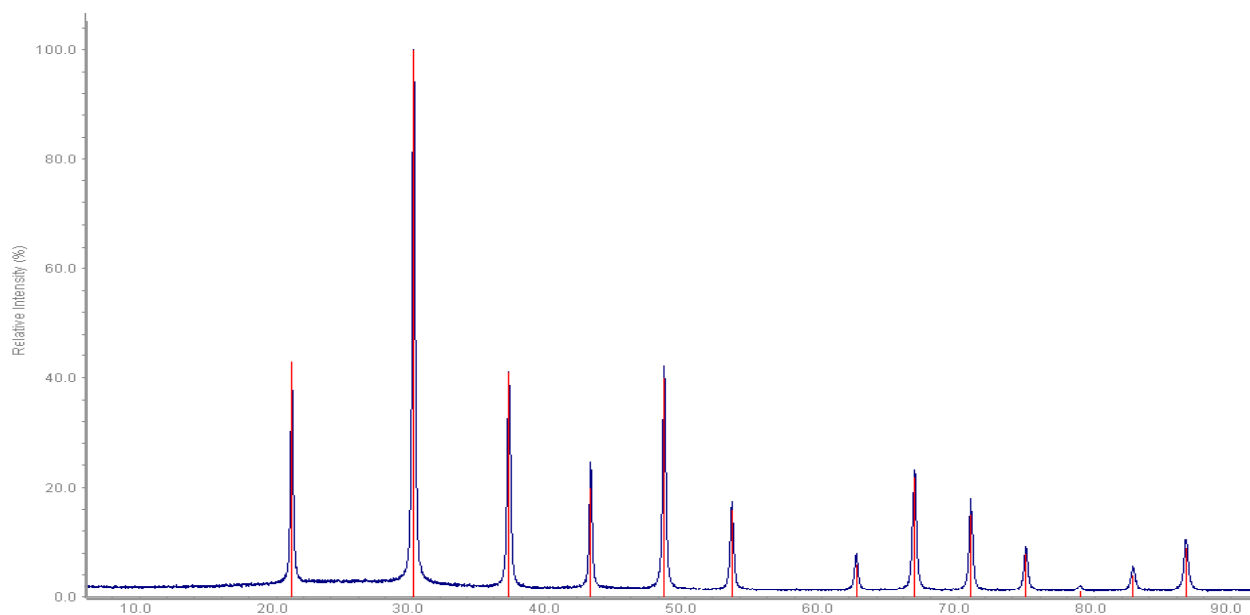
Fig. 3.1.3.5.2 XRD pattern (blue) of SrB$_6$-3 with the theoretical pattern [46] (red lines)

3.1.3.6 Thermogravimetric Analysis

Thermogravimetric analyses (TGA) show that SrB$_6$ and CaB$_6$ react with oxygen relatively slowly up to 670 ºC. Above that the rate of the reaction increases significantly (Fig. 3.1.3.6.1). For CaB$_6$ the experiment was done in oxygen atmosphere, in air and in technical Ar atmosphere. The starting point of oxidation does not depend on the amount of oxygen in the atmosphere. In the case of a small amount of oxygen it is possible to distinguish the separate reaction steps of the oxidation. According to the weight increase an addition of 3, 4 and 5 oxygen atoms per CaB$_6$ formula unit proceeds at around 1073 ºC, 1173 ºC, 1273 ºC, respectively. A complete oxidation should result in a formal addition of 10 oxygen atoms (CaO + 3B$_2$O$_3$) and a weight increase up to 260 % which is not observed in any of our experiments. In accordance with the literature the residual sample is CaB$_4$O$_7$ detected after heating up to 973 ºC and CaB$_2$O$_4$ (1173 ºC), respectively, as oxidation products [63].
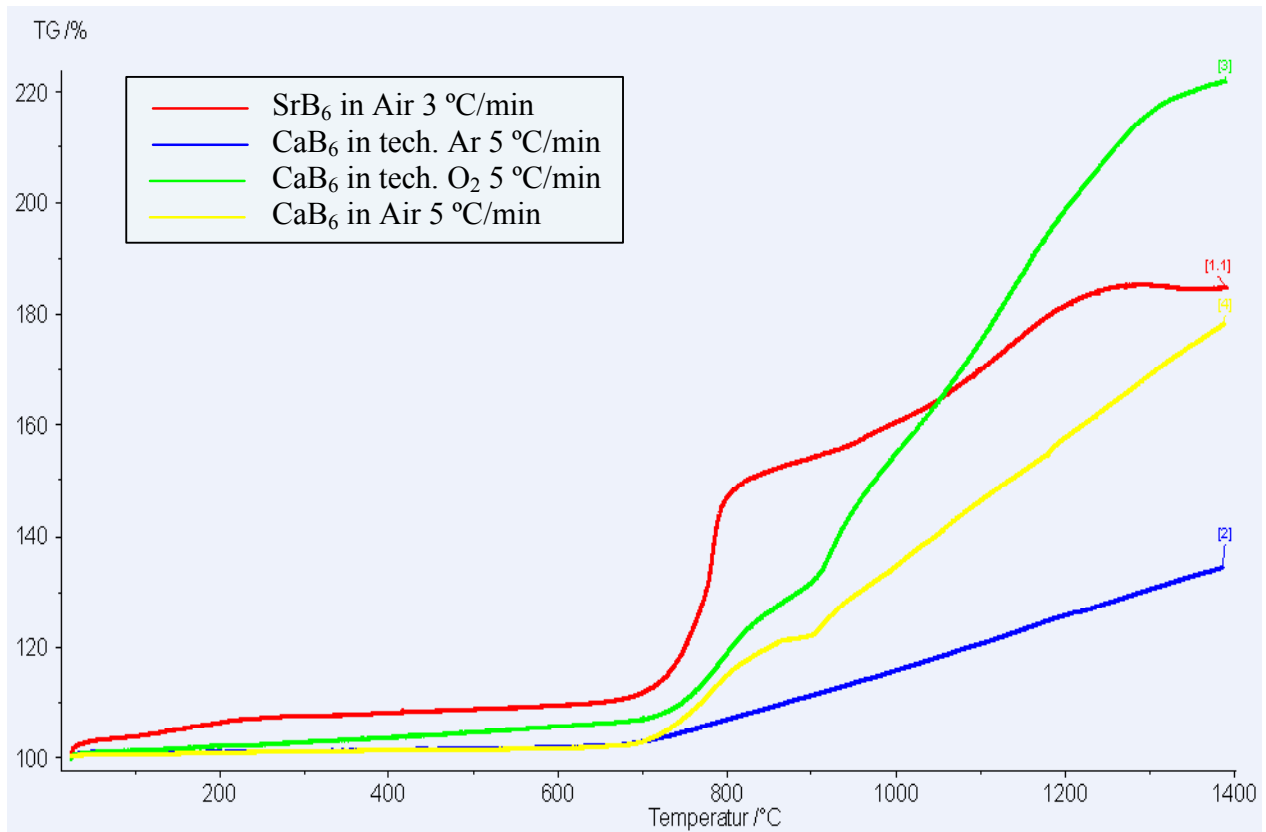
78

Fig. 3.1.3.6.1 TGA analysis of SrB_6-3 and CaB_6-2

3.1.3.7 Low Temperature Conductivity Measurements

The resistance was measured with the collinear direct-current four-contact method. Powder samples (CaB_6-1, SrB_6-4, SrB_6-3) were pressed and annealed at 400 ºC for 24 hours. Both the samples of strontium hexaboride demonstrate the same conductive behavior.

In the graph, the resistances R of CaB_6-1 and SrB_6-4 are plotted as a function of the temperature T.

For 50 K < T < 310 K the resistance decreases with increasing temperature, which is characteristic for semiconducting behavior. At low temperatures, generally extrinsic phenomena like impurities become more important. Probably those are responsible for the discontinuities below 50 K here also. For this reason a band gap should be estimated from high temperature investigations.
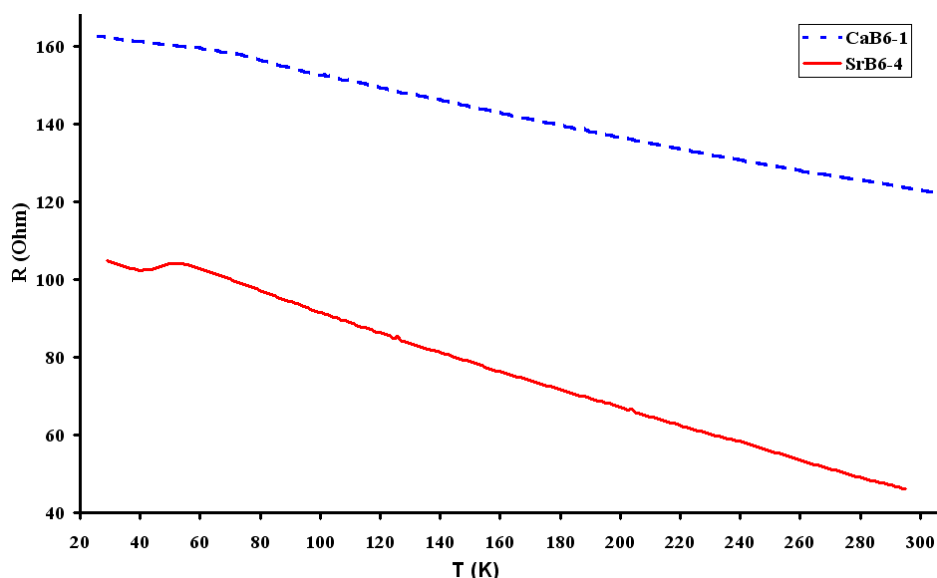
Fig. 3.1.3.7.1 Resistance of CaB_6-1 and SrB_6-4 versus temperature

3.1.3.8 High Temperature Conductivity and ICP-OES Measurements

In order to investigate the conductivity behavior at high temperatures and to determine the band gaps a linear four probe AC frequency instrument was constructed (Chapter 2.9.2).

To give an example, the resistance of sample SrB_6-1 is shown in Fig. 3.1.3.8.1 as a function of the temperature (30 - 420 °C). The typical semiconducting behavior was found for all measured samples. The range between 340 and 400 °C was used to estimate the band gap (inset). In different samples it was found to vary remarkably between 0.029 and 0.129 eV. This is probably caused by different impurity contents, which were tried to detect by ICP-OES.
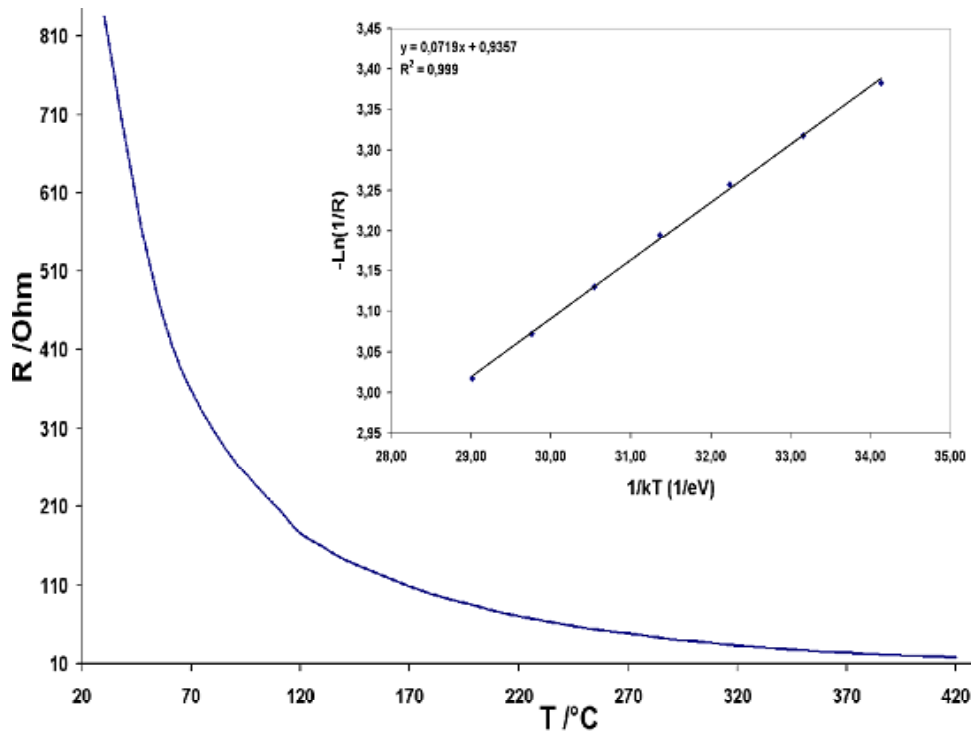
Fig. 3.1.3.8.1 Dependence of resistance on temperature, sample SrB$_6$-4

The results of impurity determinations are shown below in table 3.1.3.8.1.

Sample\Element	Al, mg/g	Ba, mg/g	Ca, mg/g	Fe, mg/g	K, mg/g	Mg, mg/g	Na, mg/g	Ni, mg/g	Si, mg/g	Zn, mg/g	Band gap, eV
SrB6-1	0.001	0.019	0.088	0.018	0.128	0.006	0.019	<C$_L$	<C$_L$	0.001	0.035
SrB6-3	0.032	0.060	0.161	0.031	0.231	0.034	0.206	<C$_L$	<C$_L$	0.003	0.056
SrB6-4	0.008	0.012	0.173	0.025	0.125	0.054	0.032	<C$_L$	<C$_L$	0.008	0.030
SrB6-5	0.025	0.097	0.193	0.027	0.255	0.029	0.121	<C$_L$	0.508	0.007	0.029
SrB6-10	0.022	0.170	0.201	0.018	0.174	0.008	0.037	<C$_L$	0.576	0.008	0.032
SrB6-7	0.043	0.156	0.386	0.020	0.375	0.026	0.555	0.002	1.583	0.023	0.060
M1	<C$_L$	0.480	0.158	0.130	0.234	0.023	<C$_L$	<C$_L$	<C$_L$	<C$_L$	0.086
M2	<C$_L$	0.630	0.049	0.015	0.219	0.016	<C$_L$	<C$_L$	<C$_L$	<C$_L$	0.075
M3	<C$_L$	0.330	0.040	0.009	0.165	0.013	<C$_L$	<C$_L$	<C$_L$	<C$_L$	0.072
M5	<C$_L$	0.559	0.135	<C$_L$	<C$_L$	0.030	0.028	<C$_L$	<C$_L$	<C$_L$	0.086
M6	0.012	0.690	0.093	<C$_L$	<C$_L$	0.031	0.042	<C$_L$	<C$_L$	<C$_L$	0.086
M7	0.004	0.533	0.122	<C$_L$	<C$_L$	0.030	0.044	<C$_L$	<C$_L$	<C$_L$	0.056
M8	0.006	0.597	0.251	<C$_L$	0.048	0.021	0.041	<C$_L$	0.328	<C$_L$	0.084
M9	<C$_L$	0.908	0.165	0.171	<C$_L$	0.006	0.049	0.055	<C$_L$	<C$_L$	0.091
MB1	0.005	0.761	0.082	<C$_L$	0.029	0.039	0.022	<C$_L$	<C$_L$	<C$_L$	0.129
MB2	<C$_L$	0.640	0.105	<C$_L$	0.034	0.020	0.067	<C$_L$	<C$_L$	<C$_L$	0.078
MB3	0.014	0.682	0.094	0.334	<C$_L$	0.019	0.040	0.082	0.080	<C$_L$	0.081
2nd	<C$_L$	0.356	0.078	0.097	0.010	<C$_L$	0.039	0.032	<C$_L$	<C$_L$	0.082
S1	0.013	0.454	0.140	0.072	<C$_L$	0.027	0.044	0.032	0.471	<C$_L$	0.059
S3	<C$_L$	0.564	0.080	0.044	0.060	0.008	0.034	0.058	<C$_L$	<C$_L$	0.077

Table 3.1.3.8.1 Impurity contents of SrB$_6$ samples (C$_L$ = detection limit) and their band gaps (calculated in temperature range 340-400 °C)

When the synthesis was optimized (metal distillation was applied for samples M1 to S3), the amount of impurities decreased according to ICP-OES. As an overall tendency, the band gaps increase in size with decreasing amounts of aluminum, nickel, sodium and potassium. Applying a multi-linear regression equation to all samples except M3, M6, M9, S1, S3 (they were used later to check the reliability of the equation) led to the following result:

$$\text{band gap [eV]}= 0.073 - 670 \cdot Al - 664 \cdot Na - 132 \cdot K - 94 \cdot Ni + 72 \cdot Ba$$

[metal content in mg/g]

The free term 0.073 refers to a band gap in the absence of impurities. It matches well with a theoretical value calculated with the LMTO method and with the band gap of SrB_6 measured in [3].

The negative contributions of aluminum and nickel are attributed to their electron-rich character. Sodium and potassium ions replace two-valence strontium and act as p-donors, thus diminishing the band gap further. When two-valence strontium ions are replaced by two-valence and very large barium ions, the lattice is distorted and the resistance increases.

We did not expect the contribution of iron atoms to be negligible. It can only be explained if we assume that our samples did not contain iron as an integral component. Traces of iron were found probably due to manipulation processes and adhere to the surface of the particles.

In the table below the band gap values calculated on the basis of our model are compared with measured values. The comparison shows a considerable congruence especially in the central range of values. The deviations of the extreme values (samples M9 and S1) indicate some disregarded contributions possibly related to not detected impurities or the, so far, surprising independence from the iron content, so this finding should be regarded carefully.

Sample	Calc. band gap, eV	Meas. band gap, eV
M3	0.076	0.072
M6	0.087	0.086
M9	0.113	0.091
S1	0.068	0.059
S3	0.078	0.077

Table 3.1.3.8.2 Calculated and measured band gaps of SrB_6

The same linear four probe AC frequency experiment was done for the samples of CaB_6-1, CaB_6-2, CaB_6-n, CaB_6-5. They all demonstrate the typical semiconducting behavior.

3.1.4 Summary

Different samples of CaB_6 and SrB_6 were synthesized. Their cubic crystal shapes were confirmed with SEM. Some samples were investigated using the EELS method showing an

almost identical fine structure of the boron K-edge for both compounds. This is assumed to be characteristic for the boron framework of divalent hexaborides. The chemical composition and the purity of the samples were proven with EELS and EDX spectroscopies. Their chemical identity was proven by XRD. The traces of impurities for SrB_6 (0-0.7 mg/g range) were measured using ICP-OES. With help of XANES the oxidation state (+II) for Ca and Sr in the respective hexaborides were confirmed. Their oxidation behavior was investigated with help of TGA method.

The conductivity of CaB_6 was investigated with low-temperature linear DC four-contact method and with high-temperature linear AC low frequency four-contact method. All measurements showed semiconducting behavior for CaB_6 and SrB_6.

The synthesis of SrB_6 was optimized so the concentration of impurities (except Ca and Ba) were decreased till 0.1-0.01 weight percent. The impurity content was characterized using a high sensitive ICP-OES method. The electronic properties of the samples were investigated by a linear four probe AC low frequency method. SrB_6 has semiconducting behavior, but the magnitude of band gap of different samples varies depending on the impurity content.

The dependence was approximated using a multi-linear regression method. The sign and the magnitude of influence of different elements were estimated and explained. The received model was used to calculate the band gap for other samples, and the results compared with measured band gaps are satisfactory.

From these calculations the band gap of 100 % pure SrB_6 can be estimated to be about 0.073 eV.

3.2 Nanoparticles of iron borides

3.2.1 State of research

In the binary system iron-boron, a lot of crystalline phases are reported. The compositions of investigated compounds range from Fe_8B to FeB_{49} [130, 131]. Within the large number of more or less well characterized compounds, the best known iron borides are Fe_2B and FeB, their crystal structures were primarily described by Wever and Mueller [132] (Fe_2B) and by Hendricks and Kosting [122] (FeB). Recently Kapfenberger succeeded in growing single crystals of Fe_2B and FeB shown in Fig. 3.2.1.1 and redetermined their crystal structures [102].

Fe_2B in *I 4/mcm*
a = 512.04(3) pm
c = 425.88(3) pm
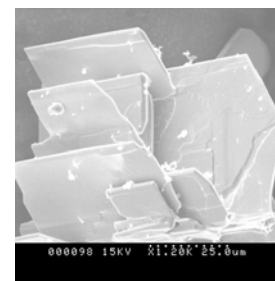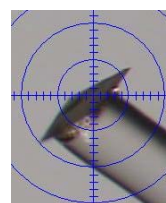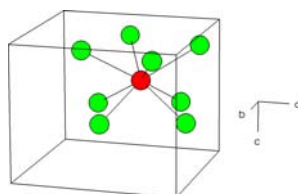
FeB in *P mcn*
a = 294.08(2) pm
b = 404.77(2) pm
c = 549.54(3) pm

Fe ●
B ●
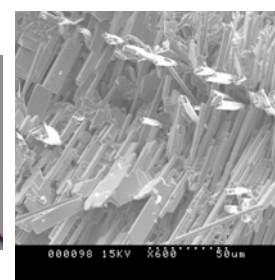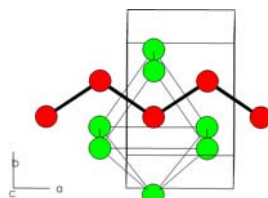

Fig. 3.2.1.1 Iron borides Fe_2B and FeB: space groups and lattice parameters, boron environment in the crystal structures, and morphology of single crystals [102]

Both compounds adopt structure types which are typical in transition metal borides. The boron environment is related to the Fe/B ratio. In Fe_2B the boron atoms are neighboured by eight iron atoms in form of a square antiprism. In FeB, the boron atoms are coordinated by seven iron atoms as a capped trigonal prism, but the closest distances are found to other boron atoms to form zigzag chains as illustrated in Fig. 3.2.1.1.

Next to the Fe/B ratio of the compound mentioned above is Fe_3B. This compounds shows a low stability against decomposition into Fe_2B and Fe, particularly at elevated temperatures. Consequently, Fe_3B is difficult to synthesize in a pure state but has been obtained by heating of amorphous $Fe_{80}B_{20}$ alloys at 50 °C/h. The crystal lattice was first considered to be orthorhombic similar to Co_3B and Ni_3B [105], but was doubted because of a remarkably

larger *b* axis which should be irreconcilable with the *b/a* ratio necessary for the stability range for the orthorhombic structure [106]. Today Fe_3B is considered to be tetragonal with lattice parameters of *a* = 863 pm and *c* = 429 pm, isotypical to Fe_3P. This conclusion was consistent with both, detailed X-ray diffraction analyses [107] and Moessbauer experiments [106]. The three compounds, discussed in detail above, are ferromagnetic with smaller local moments than for iron, exhibiting Curie temperatures of 582 °C, 1013 °C [103] and 820 °C [106] for FeB, Fe_2B and Fe_3B, respectively. The Curie temperatures, as representatives for magnetic properties in general, do not depend on the Fe/B ratio linearly. Furthermore, they differ strongly from those of amorphous alloys with the same chemical composition, but prepared by liquid-quench technique or high-rate sputtering [106, 108, 109]. Nevertheless, the tendency of the Curie temperature/boron content relationship is similar in both crystalline and amorphous iron borides. The dependence of the Curie temperature from the Fe/B ratio is illustrated in Fig. 3.2.1.2 which has been made from literature data on various iron borides [106, 109, 110, 138 - 144]. The main parameter in amorphous iron-boron alloys influencing the magnetic properties of amorphous iron borides, as shown by Fdez-Gubieda et al., is the closest distance between iron atoms [111].
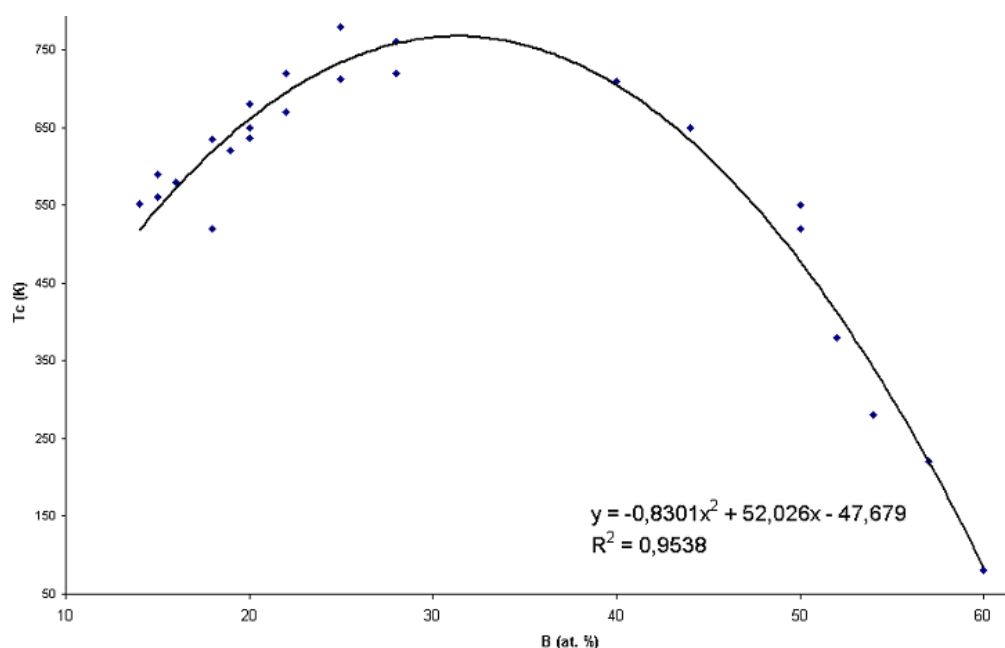

Fig. 3.2.1.2 Curie temperature of amorphous iron borides on the percentage of boron [106, 109, 110, 138 - 144]

The reduction of metal ions with alkali metal borohydride has been used extensively for the production of fine powder of metals and metal borides. Also borate particles were produced via this route [66, 67]. Other attempts resulted in preparation of amorphous Fe-B [75, 76, 112, 116], Fe-Co-B [76, 112-114] and Fe-Ni-B [115] alloy particles. A magnetic short range order

(SRO), detected in samples with similar composition 21, 27, 38 boron at. % by the zero field spin echo nuclear magnetic resonance technique, is shown to be similar to that of Fe_3B-, Fe_2B and FeB, respectively [117].

Also elemental iron was found to crystallise from amorphous $Fe_{60}B_{40}$ accompanied by Fe_2B and Fe_3B [118]. All these experiments resulted in agglomerated particles and no way to control the particle size was reported so far.

Separate magnetic nanoparticles with an adjustable size are of interest because they have a wide range of potential applications: high density magnetic recording media, ceramics, catalysts, drug delivery systems, ferrofluids, pigments in paints, and medical diagnostics [87, 88].

Iron nanoparticles with attractive magnetic properties were prepared in coordinating solutions [119, 120], but no information of their stability in air was reported.

Usually, iron nanoparticles are highly reactive and an exposition to air is not possible. For this reason, iron oxide nanoparticles, which do not change properties after air exposure, are preferred. Examples of synthesis routes and magnetic properties of iron oxides nanoparticles are given in [99, 100].

As far as we know, no successful attempt to synthesise iron boride nanoparticles is reported. The aim of this work is to synthesize nanoscale iron borides in order to analyze their composition, structural and physical properties, particularly their magnetism, as well as the character of the surface of the particles and the influence of impurities.

There are roughly two approaches to the synthesis of nanostructural materials: "top-down" and "bottom-up". The former produces nanomaterials from bulk materials mainly by physical methods (laser deposition [89], vapor deposition [90], ball milling [90, 91] etc.). The latter is more chemical in nature and includes the growth of nanoparticles from atoms and molecules. This approach is followed here in different ways.

One method involves reverse micelles as the site of formation of boride nanoparticles. The formation of Ni_2B and Co_2B, for example, was reported to proceed in cationic reverse micelles [79]. In another work, the synthesis of Co or Co_2B nanoparticles succeeded depending on the water content of the reverse micelles [80, 81]. Also Ni_2B nanoparticles [85], besides Co_2B [84] and metal and metal alloy (Co, Cu, Fe-Cu) nanoparticles [83] were obtained and characterized by means of XPS.

The second important method involved in this work, is the nanoparticle synthesis in coordinating solutions, developed and described by Murray et al. [93-95].

All products obtained in this work by the reduction of metal ions with alkali metal borohydride in water or reverse micelles methods mentioned above are amorphous powders. This often implies problems in characterisation of the samples. One method applied in particular in this work is X-ray absorption spectroscopy (XAS).

XAS is a reliable method which is widely used for the study of amorphous materials, but. The investigation of the X-ray absorption near edge structure (XANES) allows us to receive information about oxidation state, kind of scattering atom, coordination number and ionisation energy. The extended absorption fine structure (EXAFS) provides quantitative information about a local structure (coordination numbers, bond distances and debye-waller factor). Spectra in both areas could be used as fingerprints, and the results are more or less independent (in XANES the main role play multiscattering processes, in EXAFS it is single scattering processes).

Other methods used are X-Ray powder diffractometry (XRD), infrared spectroscopy (IR) and energy dispersive X-ray spectroscopy (EDX).

3.2.2 Starting materials and reference compounds

The starting materials were:

$FeSO_4 \cdot 7H_2O$ (Fluka, 99.5 %), $FeCl_2 \cdot 4H_2O$ (Merck, 99 %), $FeCl_2$ (Aldrich, 99.5 %), $Fe(acac)_2$ (iron(II)acetylacetonate, Aldrich, 99.95 %, kept under Ar atmosphere), $Fe(AOT)_2$ (was synthesized as described in [122, 123] and kept under Ar atmosphere), $NaBH_4$ (97 % Alfa Aesar, kept under Ar atmosphere) and $LiBH_4$ (Aldrich, 95 %, kept under Ar atmosphere) served as iron and boron sources, respectively.

Complexing agents were:

Sodium bis(2-ethylhexyl)sulfosuccinate (NaAOT, 96 % Alfa Aesar), trioctylphosphine (TOP, 90 % Fluka), hexadecylamine (HDA, Merck, 92 %), 1,2-hexandiole (Fluka, > 97 %), oleylamine (Fluka, technical, $\geq$ 70 %), oleic acid (Aldrich, technical, 90 %, was kept in a refrigerator).

As solvents were used:

Trioctylphosphine (TOP, 90 % Fluka), diphenylether (Alfa Aesar, 99 %), dioctylether (Fluka, $\geq$ 97 %) were degassed before use.

Chloroform (Acros, technical), methanol (Acros, technical), acetone (Acros, technical), toluene (Riedel-de-Häen, technical), tetrahydrofuran (THF) (Merck, pro analyze), isooctane (99.5 % Fluka) were distilled before use.

Ion-exchangers were:

Lewatit SP 112 and Lewatit CNP-80 (Bayer, 98 %).

The reference materials were:

$FeSO_4 \cdot 7H_2O$ (Fluka, 99.5 %), Fe (Chempur, 99.9 %), FeO (Alfa Aesar, 99.5 %), Fe_2O_3 (Fluka, 99 %), Fe_3O_4 (Chempur, 99.5 %), $FeCl_3$ (Aldrich, 98 %), FeB (Chempur, 99 %), FeB synthesised from Fe (Chempur, 99.9 %) and B (Chempur, 99.9 %), mixed and pressed together with an excess (5 %) of boron and melted in an electric arc. The example together with the theoretical pattern [126] is shown in Fig. 3.2.2.1.

Fig. 3.2.2.1 XRD pattern (blue) of FeB-5 with the theoretical pattern [126] (red lines)

Fe_2B (Chempur, 99 %). Fe_2B synthesised from Fe (Chempur, 99.9 %) and B (Chempur, 99.9 %), mixed and pressed together with an excess (5 %) of boron and melted in an electric arc. The example together with the theoretical pattern [126] is shown in Fig. 3.2.2.2.
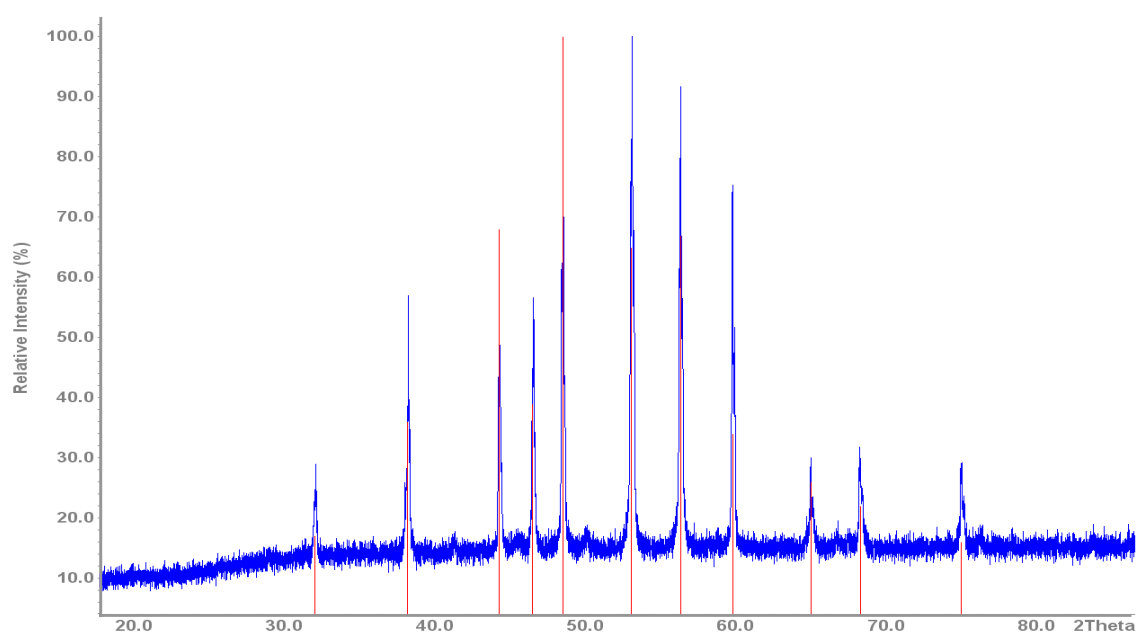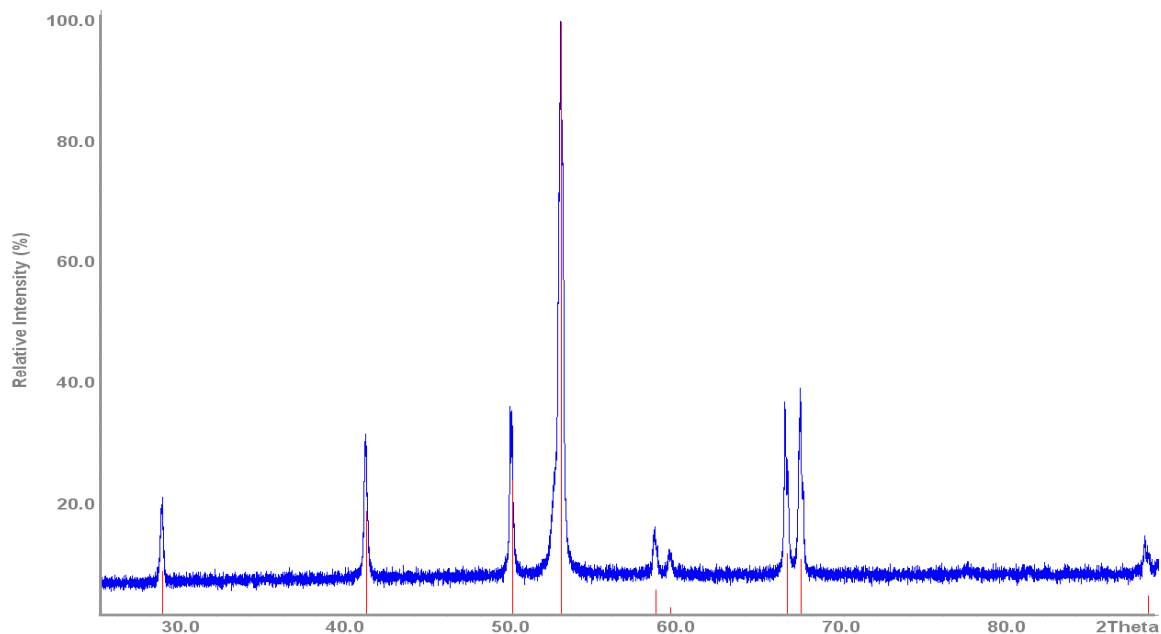
Fig. 3.2.2.2 XRD pattern (blue) of Fe$_2$B-6 with the theoretical pattern [126] (red lines)

Fe$_6$B$_{14}$O$_{27}$·H$_2$O was synthesized as it was described in [121]. The example together with the theoretical pattern [121] is shown in Fig. 3.2.2.3. The main impurity (reflection at 49.5º (2θ)) indicates the presence of FeO impurities [145].
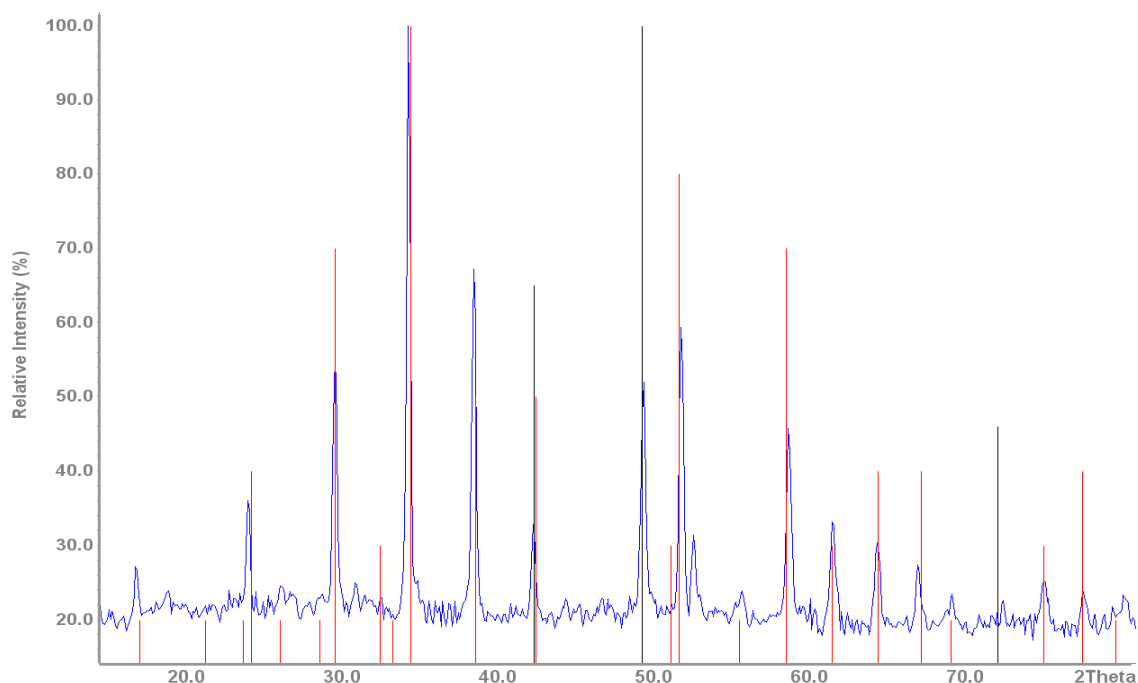
Fig. 3.2.2.3 XRD pattern (blue) of Fe$_6$B$_{14}$O$_{27}$·H$_2$O-1 with the theoretical patterns of Fe$_6$B$_{14}$O$_{27}$·H$_2$O [121] (red lines) and FeO [145] (black lines)

Fe(BO$_2$)$_2$ was synthesized from FeO (Alfa Aesar, 99.5 %) and B$_2$O$_3$ (Alfa Aesar, 99 %) (900ºC, 48 h, in Ar atmosphere) as it was described in [146]. The example together with the

theoretical pattern [146] are shown in Fig. 3.2.2.4. Impurities are starting materials FeO [145] and B_2O_3 [152], and two modifications of Fe_2O_3 [151, 153].
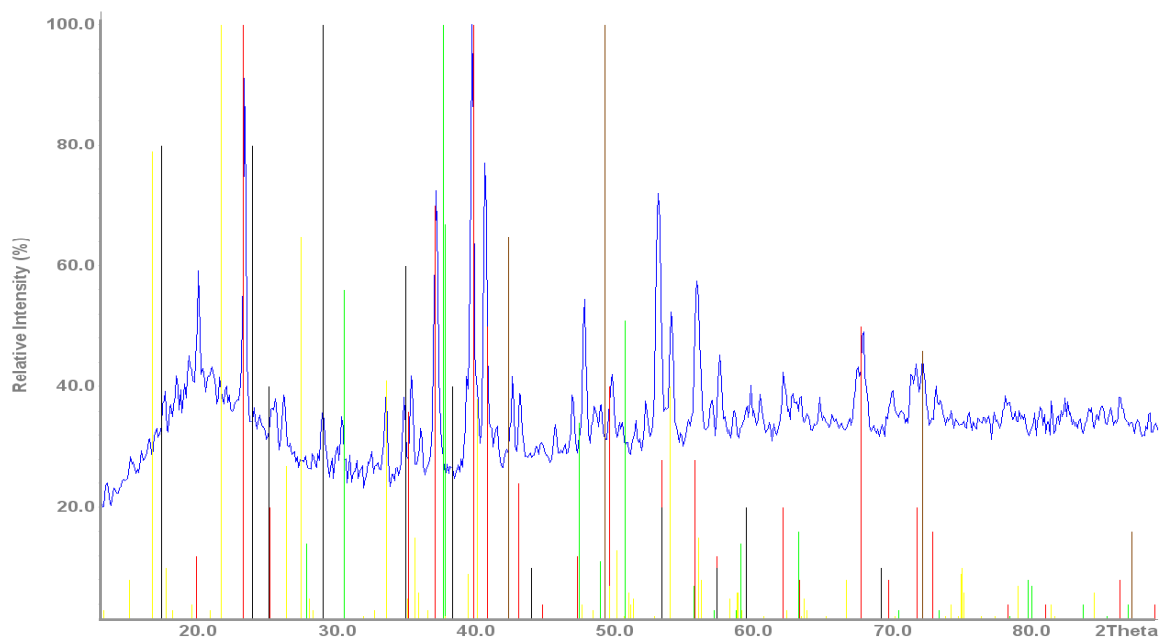
Fig. 3.2.2.4 XRD pattern (blue) of $Fe(BO_2)_2$ -1 with the theoretical patterns of $Fe(BO_2)_2$ [146] (red lines), FeO [145] (brown lines), B_2O_3 [152] (green lines), Fe_2O_3 [151, 153] (black and yellow lines, respectively)

$FeBO_3$ and Fe_3BO_6 were synthesized as it was described in the literature [27]. The examples together with the theoretical pattern [27, 147] are shown in Fig. 3.2.2.5 and Fig. 3.2.2.6.
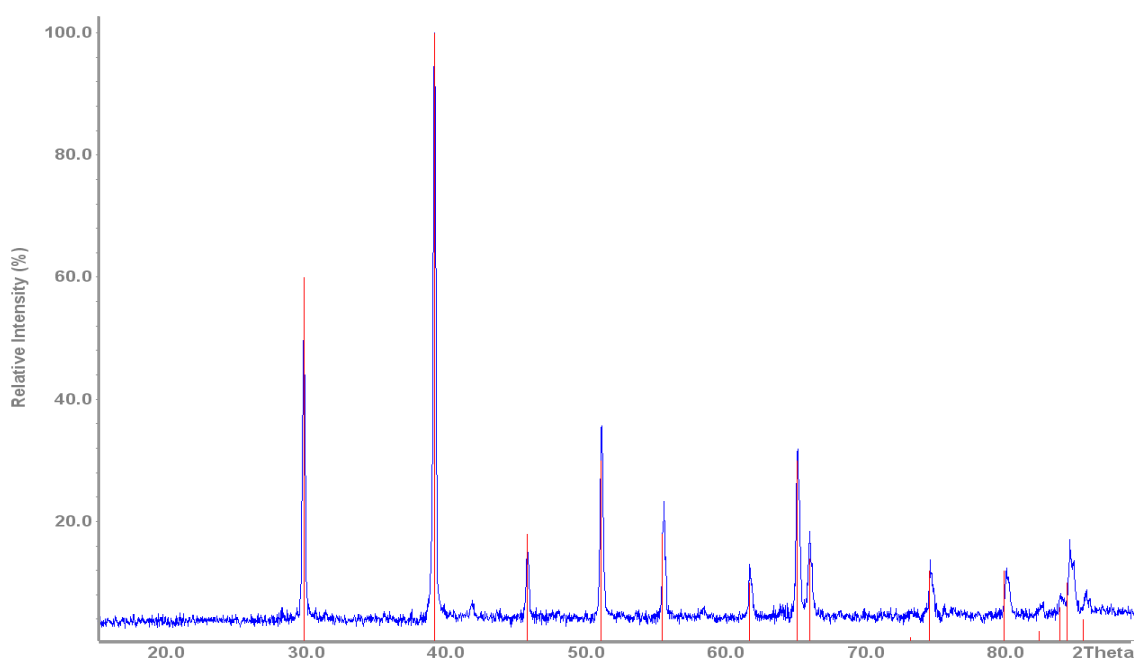

Fig. 3.2.2.5 XRD pattern (blue) of $FeBO_3$ -d with the theoretical pattern [27] (red lines)
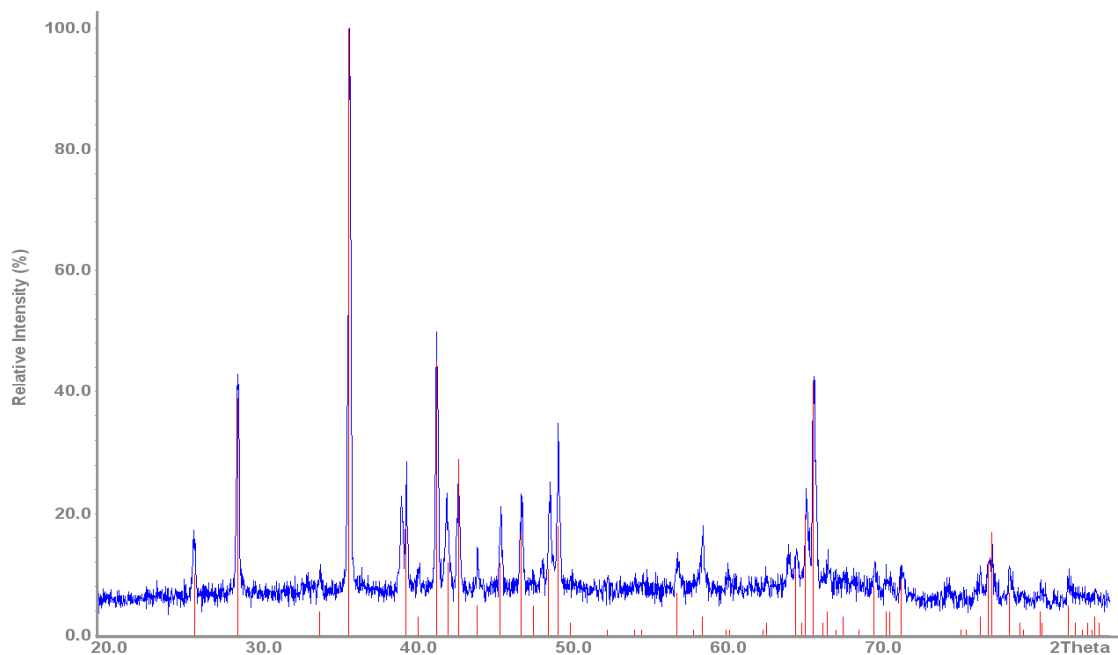
Fig. 3.2.2.6 XRD pattern (blue) of Fe_3BO_6 -d with the theoretical pattern [147] (red lines)

3.2.3 Synthesis in aqueous solutions

The synthesis of the investigated compounds is based on the preparative routes described bei Glavee and Klabunde in [67, 68, 71]. Samples were prepared by chemical reduction of Fe^{2+} with $NaBH_4$.

All reactions were carried out in 250-ml three necked round bottom flasks equipped with a dropping funnel and a reflux condenser. They whole apparatus was attached to a vacuum-argon line. Prior to the synthesis it was evacuated and kept under argon over pressure (0.1 bar). The deionised water and acetone needed were purged with argon for one hour before to use. All the chemicals were weighed in the glove-box. The whole synthesis was done in argon atmosphere.

The needed amount of $NaBH_4$ was solved in 50 ml deionised water in the reaction vessel. In a separate 100-ml flask the aqueous solution of 50 ml of $FeSO_4 \cdot 7H_2O$ solution was prepared. Then it was added drop wise during some time interval (Time 1) via the dropping funnel to formerly prepared $NaBH_4$ solution, accompanied by vigorous stirring. The reaction took place immediately, indicated by a blackening of the solution accompanied by gas evolution. It was kept stirring for another time interval (Time 2) to be sure that the reaction is complete. Afterwards the black precipitate was filtered and washed with degassed water and subsequently with degassed acetone. Finally it was vacuum-dried (150 °C) for 12 h. The

91

influence of concentrations of the starting materials and time intervals on the products were investigated. Table 3.2.3.1 shows the reaction conditions used.

Sample	NaBH$_4$, mol	FeSO$_4$·7H$_2$O, mol	Time 1, min	Time 2, min
Fe-t-1	0.5	0.5	2	2
Fe-t-2	0.5	0.5	15	15
Fe-t-3	0.5	0.5	30	30
Fe-t-4	0.5	0.5	45	45
Fe-0	0.3	0.3	30	30
Fe-0-1	0.3	0.3	30	30
Fe-1	0.5	0.5	30	30
Fe-1-1	0.5	0.5	30	30
Fe-2	0.5	0.1	30	30
Fe-2-1	0.5	0.1	30	30
Fe-3	0.1	0.5	30	30
Fe-3-1	0.1	0.5	30	30
Fe-4	0.1	0.1	30	30
Fe-4-1	0.1	0.1	30	30
Fe-51104	0.5	0.5	2	2
Fe-71104	1.0	0.1	30	30
Fe-91104	0.1	1.0	30	30

Table 3.2.3.1 Reaction conditions

The products were fine, pyrophoric powders. Part of each sample was passivated under slow flowing argon with 4 ppm oxygen for 24 hours, in order to investigate it in air also.

3.2.4 Characterization of products of synthesis in water solutions

Scanning electron microscopy (SEM), carried out for samples Fe-0, Fe-0-1, Fe-1-1, Fe-2-1, Fe-3-1 and Fe-4-1, shows that they consist of agglomerated nanoparticles of size from 20 to 150 nm, typical examples are shown on Fig. 3.2.4.1-3.
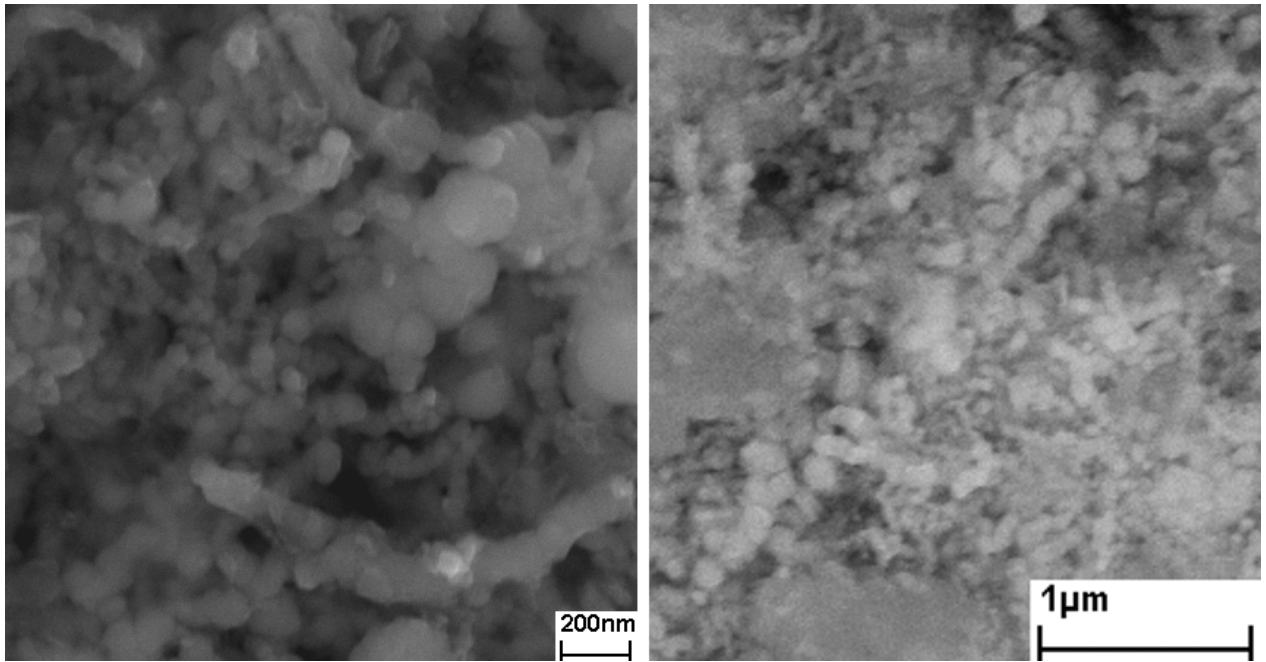
Fig. 3.2.4.1 SEM image of Fe-0-1 (left) and Fe-1-1 (right) samples
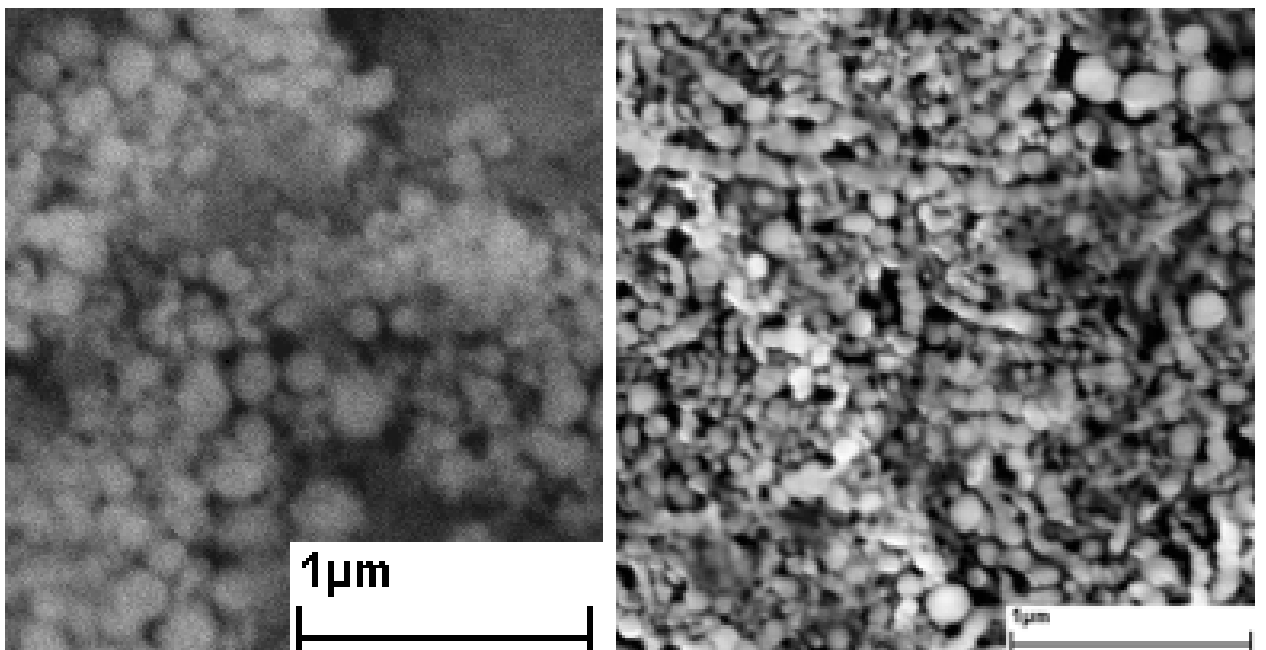
Fig. 3.2.4.2 SEM image of Fe-2-1 (left) and Fe-3-1 (right) samples
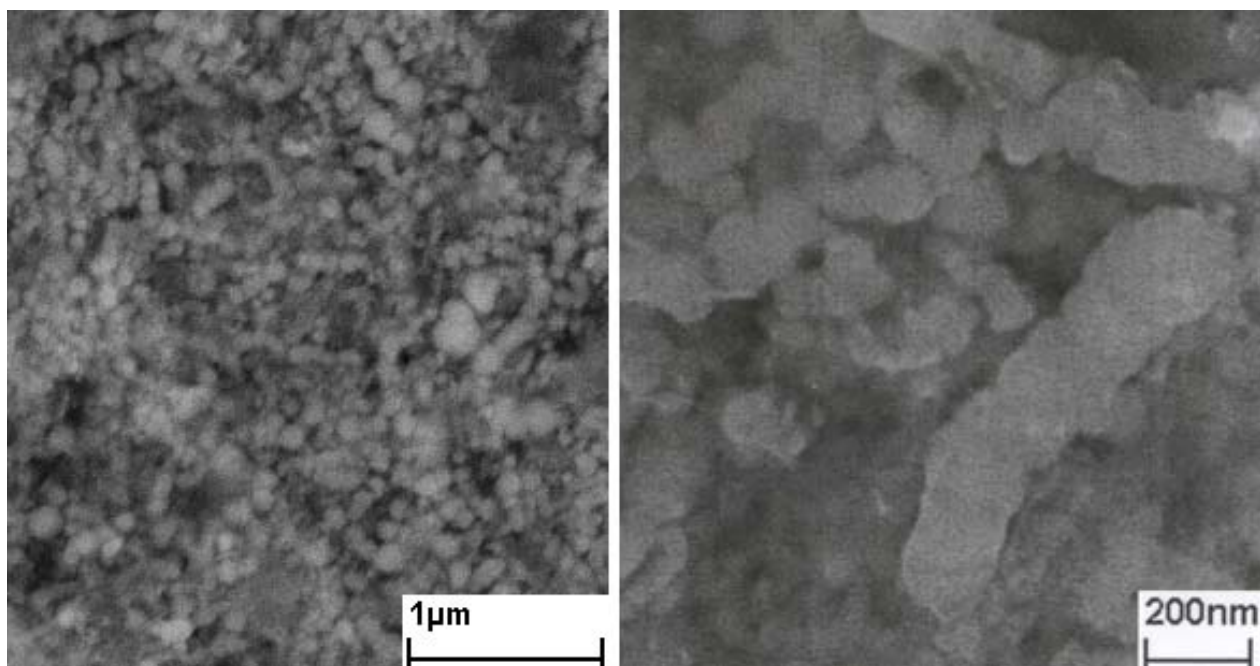
Fig. 3.2.4.3 SEM image of Fe-4-1 (left) and Fe-0 (right) samples

At first, the influence of reaction times on the results of the syntheses was investigated. When the times of dropping (T_d) and stirring (T_s) were shorter than five minutes, only pure iron resulted after washing and drying (Samples Fe-t-1 and Fe-51104). By EDX of passivated samples only iron and oxygen have been detected. After annealing (in vacuum, 400 ºC, 12 h) the XRD pattern shows iron reflections with traces of iron oxides (Fig. 3.2.4.4).
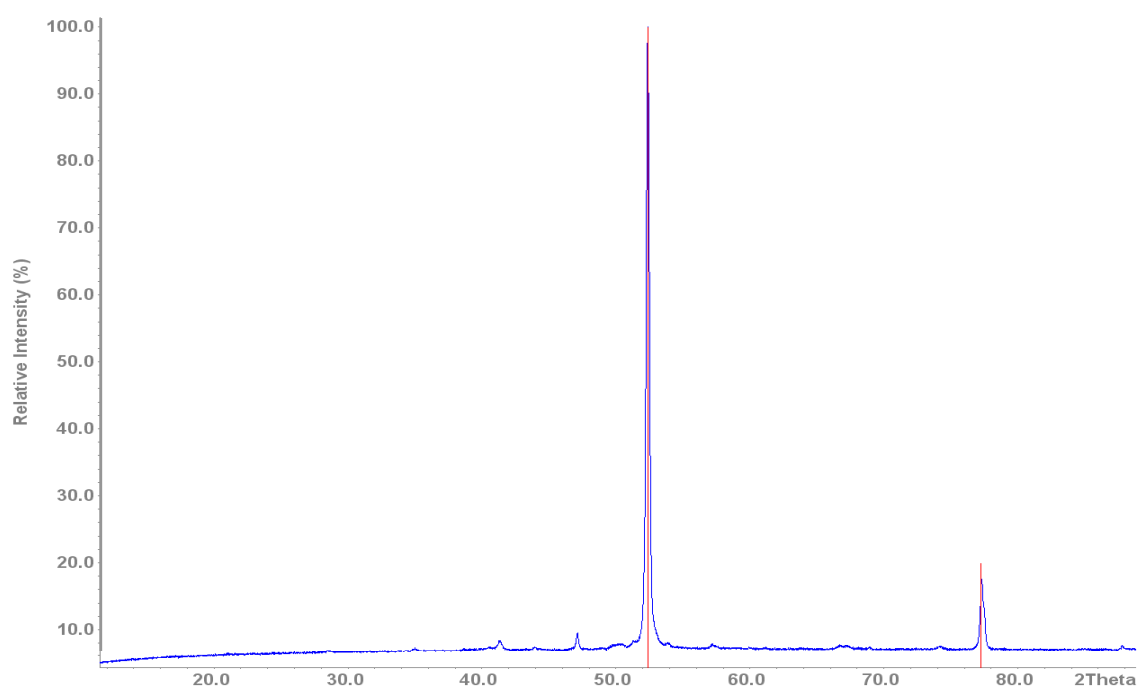
Fig. 3.2.4.4 XRD pattern (blue) of Fe-51104 with the theoretical patterns of Fe [148] (green lines)

The XANES spectra of these samples repeat almost exactly that of the reference iron powder. The same is valid for EXAFS spectra, where the only difference is a shift of peaks a little bit left compared to the reference, meaning slightly shorter Fe-Fe distances for amorphous than for crystalline iron. The experiment was done two times exactly with the same result, the examples of XANES and EXAFS spectra are demonstrated on the Fig. 3.2.4.5-7.
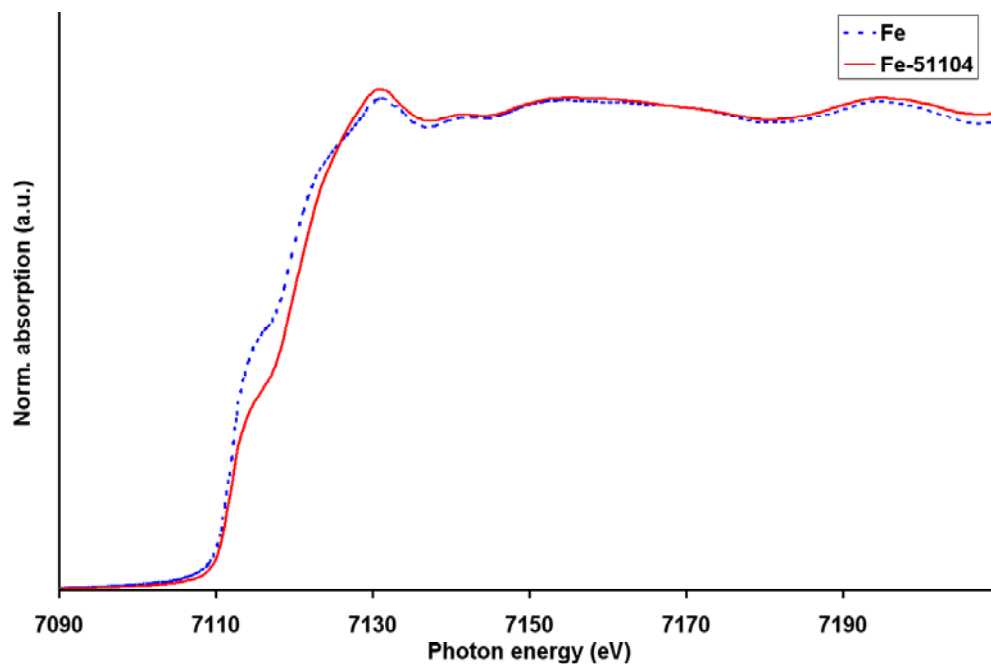
Fig. 3.2.4.5 K-edges (XANES) of the sample (Fe-51104) and reference iron powder (Fe)
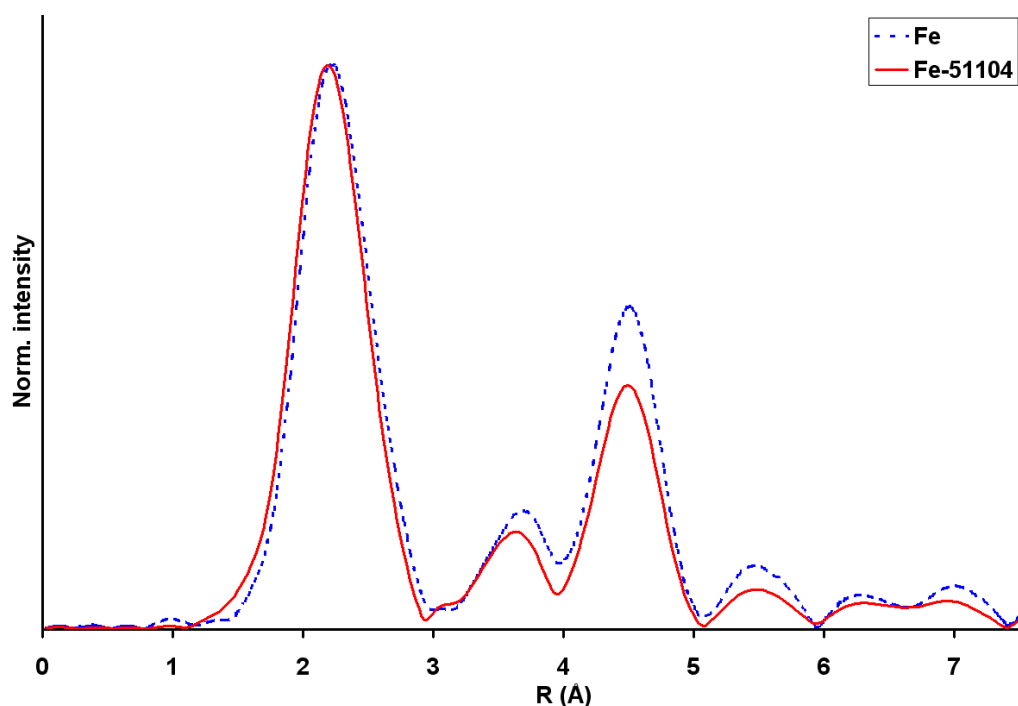
Fig. 3.2.4.6 EXAFS spectra of the sample (Fe-51104) and reference iron powder (Fe)

EXAFS profile fits were made using FEFF-7 files for Fe. Both magnitude and imagine parts of Fourier transformed k^3-weighted experimental absorption function were fitted, for more reliability in obtained distances [70]. The example of an EXAFS fit for sample Fe-51104 is shown in Fig 3.2.4.7.
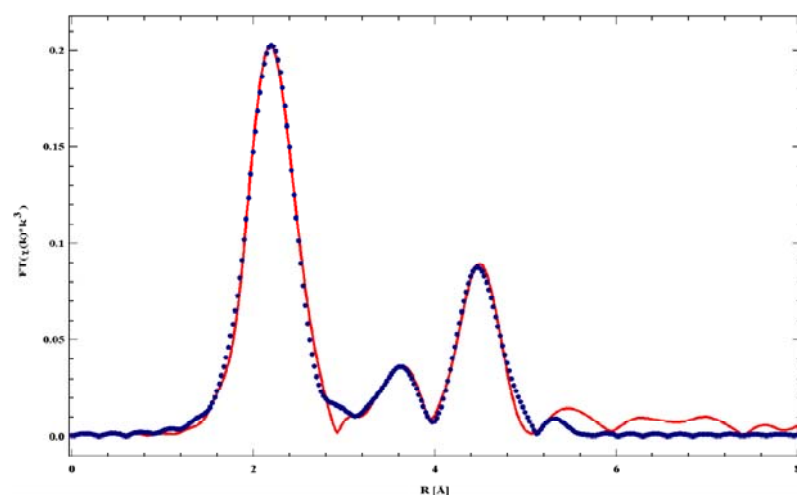
Fig. 3.2.4.7 EXAFS FT fit (blue dashed line) for the sample Fe-51104 (red line)

When T_d and T_s are longer than 5 minutes, it is possible to see traces of Fe_2B after annealing (in vacuum, 400 ºC, 12 h). The amount of Fe_2B is increasing with increase of T_d and T_s up to 30 minutes, after that it is constant. The example (Fe -1) together with the theoretical patterns of Fe [148] (green lines) and Fe_2B [132] (red lines) are shown in Fig. 3.2.2.8.
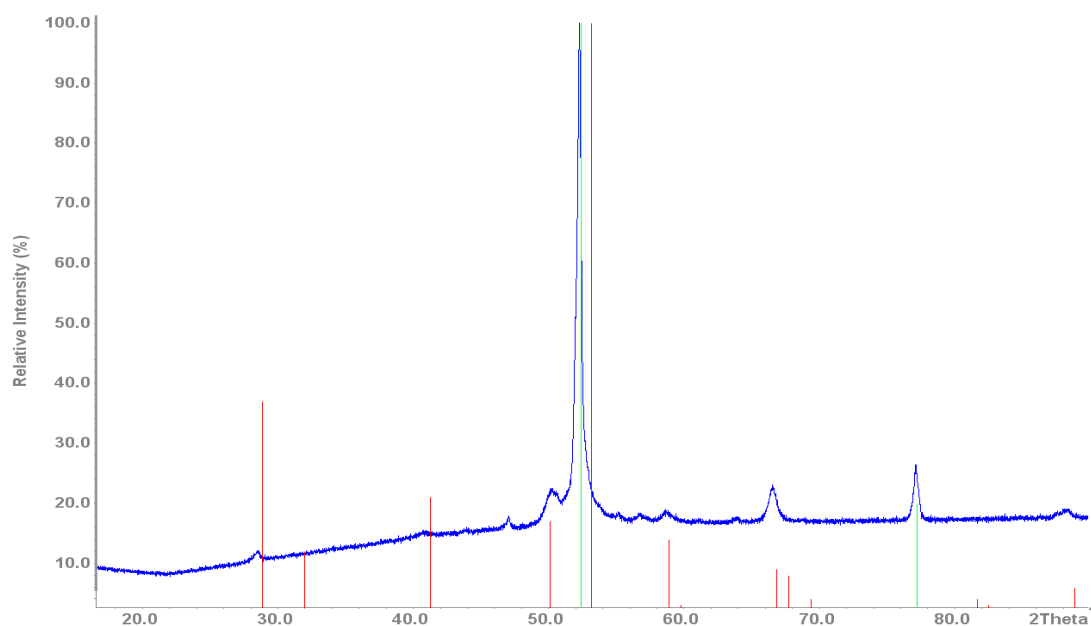
Fig. 3.2.4.8 XRD pattern (blue) of Fe-1 with the theoretical patterns of Fe [148] (green lines) and Fe_2B [132] (red lines)

The next step was to find a dependence of the reaction products on the concentrations of the starting compounds. They were changed in the range from 0.1 to 0.5 mol with different ratios, while T_d and T_s were kept constant at about 45 minutes. By EDX of passivated samples iron, boron and oxygen have been detected, the average ratio of iron to boron was 3.5 to 1. The main factor in the investigated area was the concentration of $FeSO_4 \cdot 7H_2O$. The influence of the concentration of $NaBH_4$ on the products in the investigated range was negligible. Regarding the K-edge positions in XANES spectra, the samples could be classified into two groups with more or less than a concentration of 0.3 mol of Fe^{2+} ions in the reaction mixtures. Samples resulting from lower concentrations show a K-edge shift of 0.65 eV to the right compared to those from higher concentrations as can be seen on the Fig. 3.2.4.9.
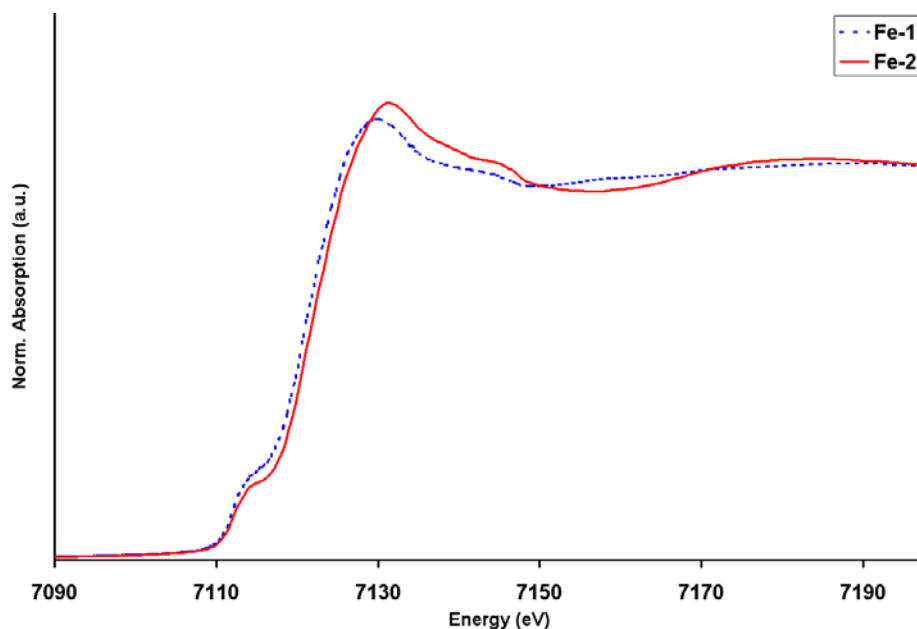
Fig. 3.2.4.9 Positions of K-edges (XANES) for the group 1 (sample Fe-2) and the group 2 (sample Fe-1)

The position of energy edge (EE) depends on the oxidation state and the kind of scattering atom in the first atomic shell. The EE was fitted with a Lorentzian and a modified arctangent function, the fit parameters were used to determine the EE positions of the systems studied [70].

The dependence of the oxidation state from the EE position for the reference samples is shown in the Fig. 3.2.4.10.
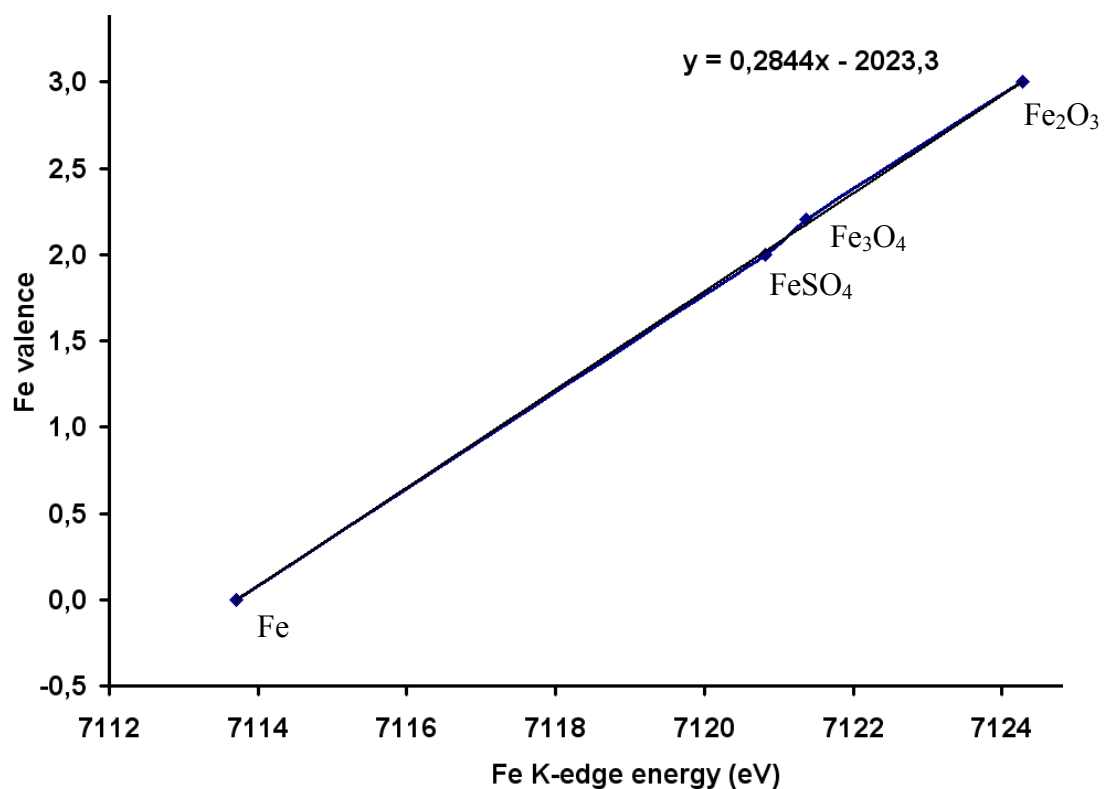
Fig. 3.2.4.10 Dependence of oxidation state from the position of EE for reference samples

Concerning the different type of scattering atoms in the first coordination shell, for reference compounds with the same oxidation state the energy of the main feature of the edge increases with the increasing of the atomic number (AN) of scattering atoms. As an example, the EE positions for the reference compounds Fe_2O_3 and $FeCl_3$ are shown in Fig. 3.2.4.11.
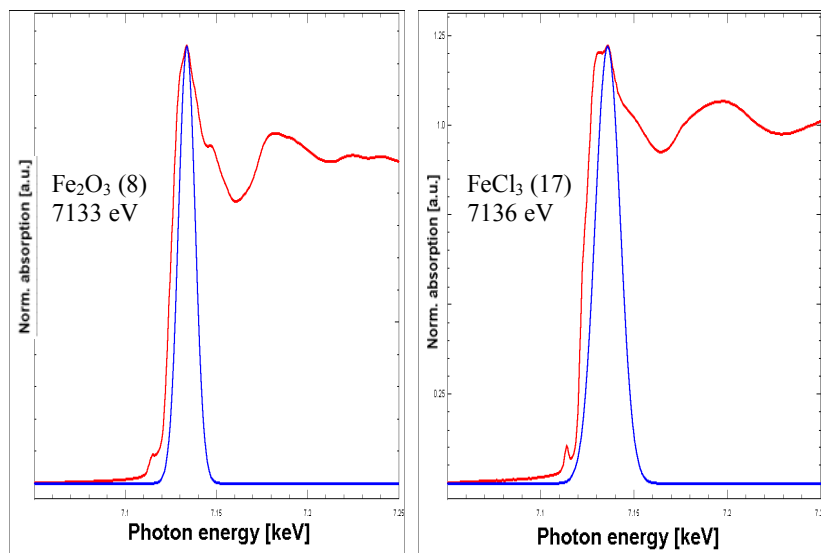
Increase of Edge Energy (EE) => Increase of scattering atomic number (AN)
$\Delta EE_{Cl-O}=3$ eV for $\Delta AN_{Cl-O}=9$

Fig. 3.2.4.11 Dependence of the position of EE (XANES) from the kind of scattering atoms

The EE differs about 3 eV for an AN difference of 9 for the first shell scattering atom (AN(O)=8, AN(Cl)=17). For an EE difference of 0.65 eV between the different groups of samples concerning the Fe concentration, this means to have different elements in the first coordination shell of iron also, but probably with less differing AN's, and with the lighter element in the samples with lower EE position, i.e. higher iron concentrations. Worth to be considered as close neighbors to iron are boron and oxygen only, according to EDX and EELS measurements. Attempts to fit the XANES spectra of the first group of samples with those of iron, iron oxides and iron borides were not successful.

In figure 3.2.4.12, XANES spectra of $Fe(BO_2)_2$, FeO and one sample out of the first group are compared. The peaks following the K-edge of higher energies (A and B in figure 3.2.4.12) of sample Fe-71104 are closer to those of the borate than to those of the oxide.

So from XANES, EDX and EELS measurements it can be concluded that the samples of the first group prepared from lower concentrated iron solutions mainly consist of iron borates.

99
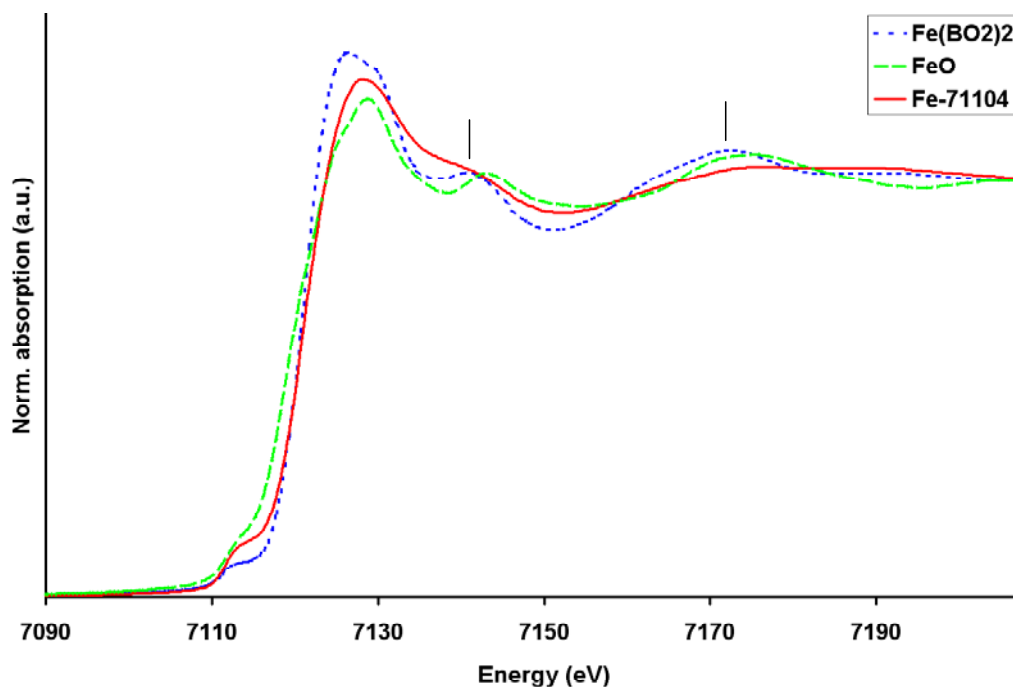
Fig. 3.2.4.12 K-edges (XANES) of $Fe(BO_2)_2$, FeO and the sample Fe-71104 (group 1)

The EXAF spectrum of the same sample is compared to another borate, $Fe_6B_{14}O_7·H_2O$, and to FeO in figure 3.2.6.13. Here also the sample spectrum is more similar to the borate then to the oxide, especially the peak at 2.5-3.5 Å is weak in the sample but intensive in FeO.

Fig. 3.2.4.13 EXAFS spectra of $Fe_6B_{14}O_7·H_2O$, FeO and the sample Fe-71104 (group 1)
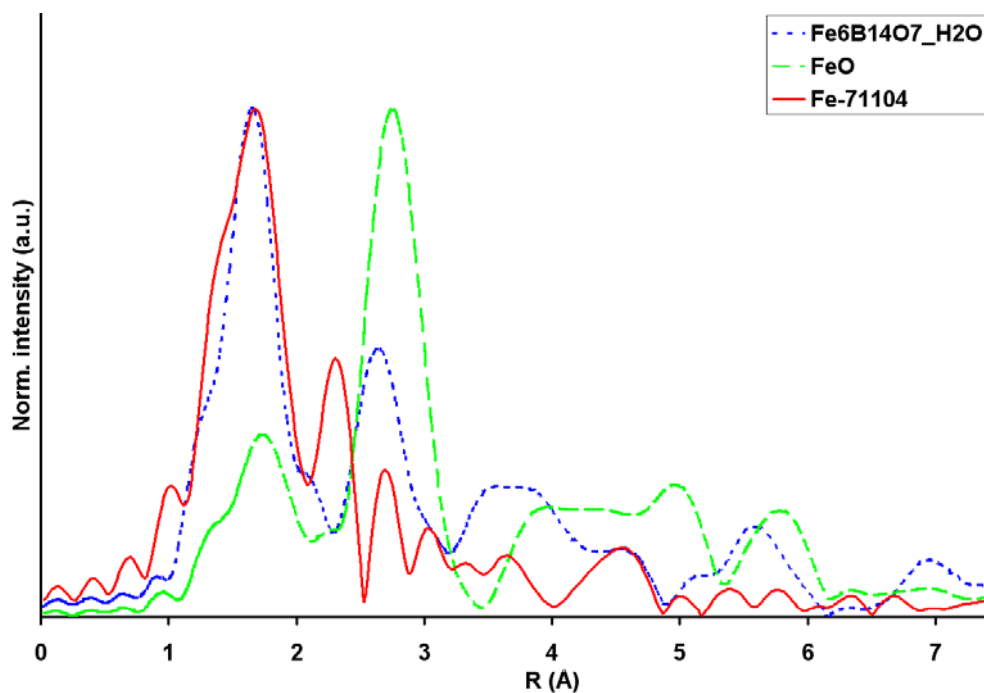
With IR spectroscopy, a quite weak broad band from 1100 to 1300 cm^{-1} and a more sharp one at 700 cm^{-1} was detected for the samples of the first group, and only traces of them for the

second group. Both observable absorptions were assigned to iron borate (most probably to the group BO_3) [27-28] (Fig. 3.2.4.14) .
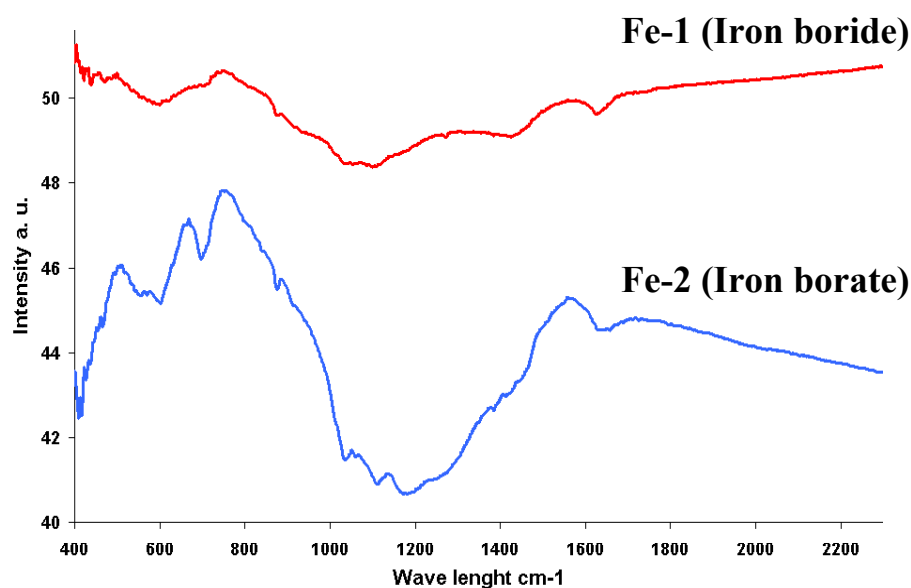
Fig. 3.2.4.14 Infrared spectra of group 1 (sample Fe-2) and group 2 (sample Fe-1)

So, according to EDX, EELS, IR, XANES and EXAFS investigations, the product of the reduction with sodium borohydride is amorphous iron borate, when the iron ion concentration was less than 0.3 mol during the synthesis. The XRD pattern of an annealed (in vacuum, 400 ºC, 12 h) sample from this group can be good fitted with several theoretical patterns of iron and iron borates [148 - 150] as can be seen on the Fig. 3.2.4.15, the presence of iron can be explained through possible reducing effect of annealing and transfer of boron oxide group in gas form under high temperature.
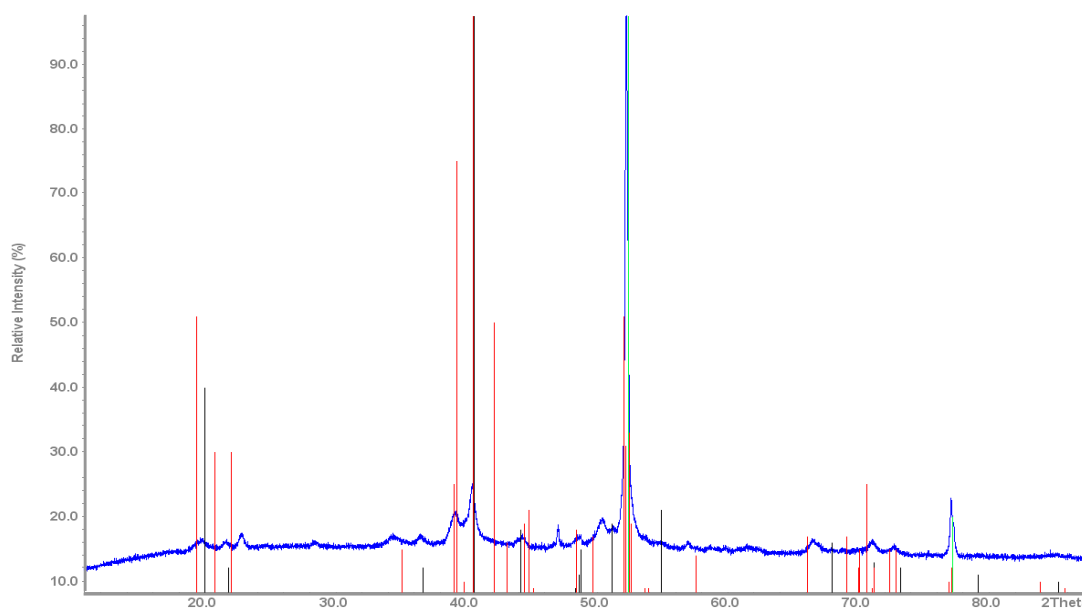
Fig. 3.2.4.15 XRD pattern (blue) of Fe-2 with the theoretical patterns of Fe [148] (green lines), $Fe_3(BO_3)O_2$ [149] (rot lines) and Fe_3BO_5 [150] (black lines)

For the second group of samples prepared from solutions of an iron ion concentration of more than 0.3 mol, it was deduced from various measurements, that boron atoms form the first coordination shell around iron atom. After annealing (in vacuum, 400 ºC, 12 h) these samples, the XRD patterns show reflections of Fe_2B besides elemental Fe (Fig. 3.2.4.8). From these findings we conclude to have mainly amorphous iron borides obtained in the experiments mentioned above. The results resemble to those (similar chemical composition $Fe_{100-x}B_x$ with $20 \leq x \leq 38$, mixture of Fe and Fe_2B phases after annealing detected by XRD and Moessbauer spectroscopy, similar EXAFS spectra) reported in the literature [75, 76], where amorphous iron borides produced by chemical reduction of iron salts by alkaline-metal borohydrides are reported.

The XANES spectra of sample Fe-3 is almost identical to that of the crystalline iron borides, as shown in Fig. 3.2.4.15.
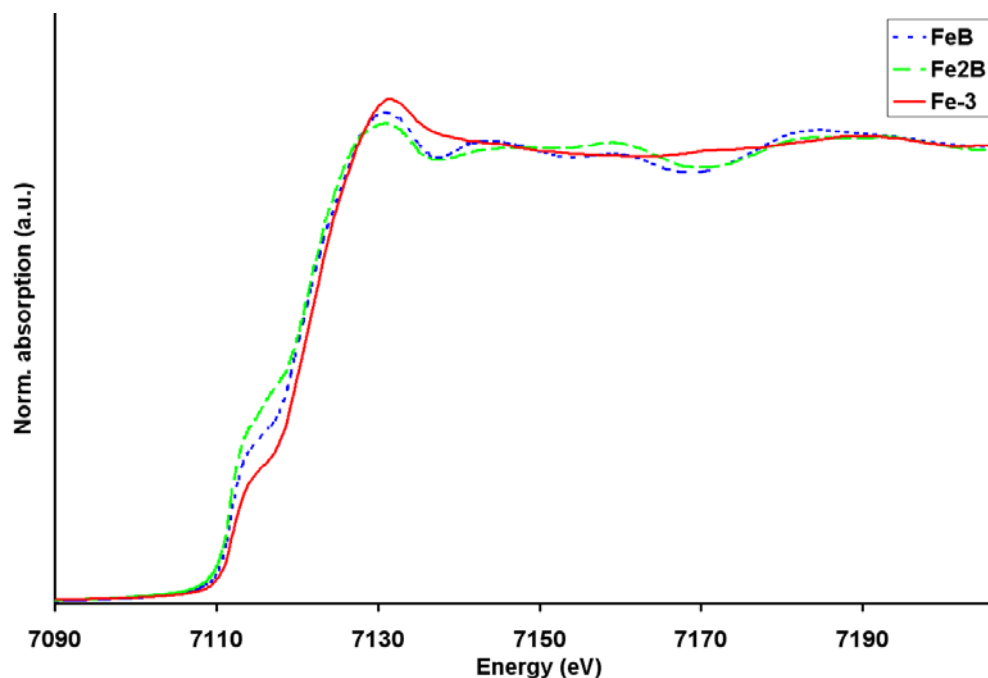
Fig. 3.2.4.15 K-edges (XANES) of the sample Fe-3 (second group) and reference iron borides

The EXAFS spectra are similar to those of iron borides [77, 78], as shown in Fig 3.2.4.16 below. The main peak has a shoulder on the left side and is located between 1 and 3 Å with a maximum at about 2.3 Å. All peaks are shifted to lower distances compared to Fe_2B. This phenomena is probably caused by the amorphous state of the samples, where the average distances are slightly shorter than in the crystalline state, or by a smaller amount of boron (25-35 % as detected in EDX measurements), which is in good agreement with formerly reported results [71, 75, 76, 77, 116, 117]. Also the same positions are given for amorphous borides of the compositions $Fe_{1-x}B_x$ with x=0.15, 0.2, 0.25 [77].
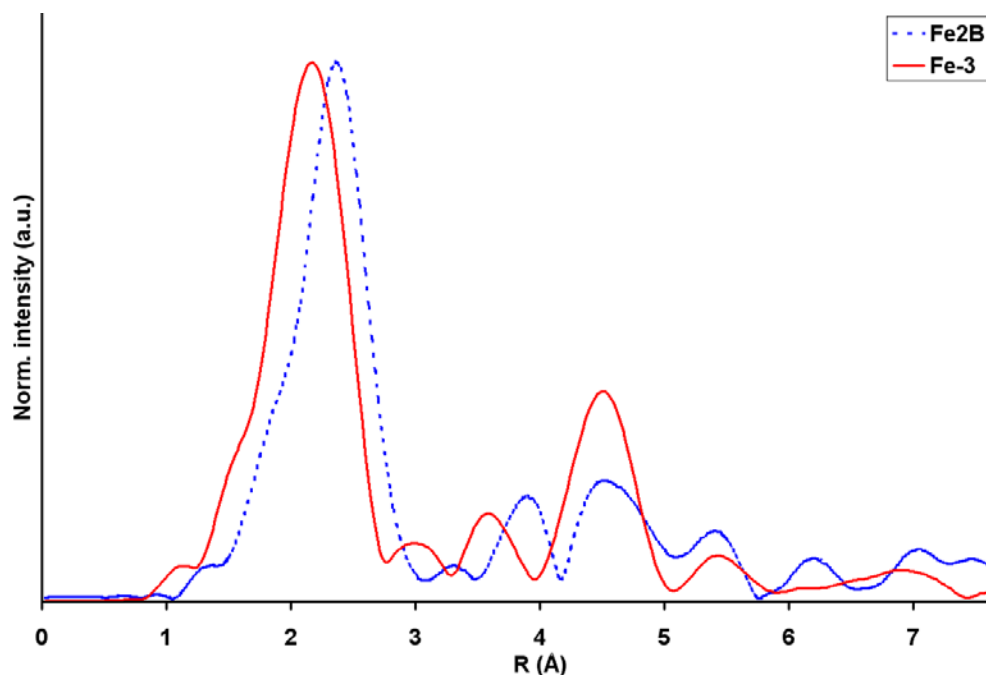
Fig. 3.2.4.16 EXAFS spectra of the sample Fe-3 and reference Fe_2B

The atomic bonds (R) for the first two shells were estimated also comparing FT peaks positions (they are proportional atomic bonds) with reference (FeB and Fe_2B) with known bonds. The coordination numbers (CN) could be estimated also from the structure of this results (CN and R) are in Table 3.2.4.1.

Sample	CN	Fe-B R, Å	Fe-Fe R, Å
Fe-1	7.3	2.06	2.44
Fe-3	6.6	1.91	2.41

Table 3.2.4.1 Estimated values of coordination numbers and atomic distances for the samples Fe-1, Fe-3

EXAFS profile fits were made using FEFF-7 files for Fe_2B, which has the most similar element ratio from available crystalline iron borides according to EDX measurements, and estimated coordination numbers (CN) and atomic distances shown in Table 3.2.4.2 above. EXAFS fits were carried out in real space with simultaneously observable k-space, for more consistency. Both magnitude and imagine parts of Fourier transformed k^2-weighted experimental absorption function were fitted, for more reliability in obtained distances [70]. The results are listed in Tables 3.2.4.2 and 3.2.4.3, the example of EXAFS fit for sample Fe-1 is shown in Fig 3.2.4.17.
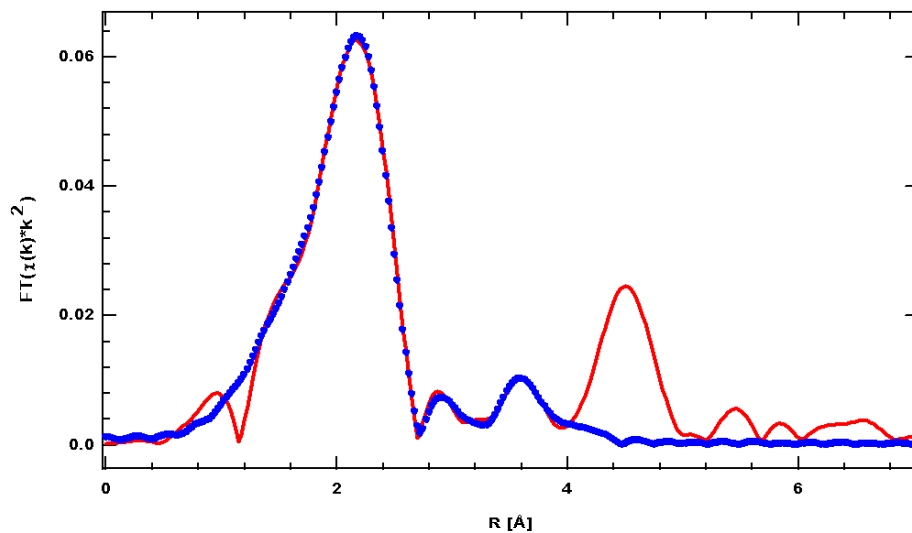
Fig. 3.2.4.17 EXAFS fit (blue dashed line) for sample Fe-1 (red line)

N	Bond	CN	R, Å	σ^2, Å^2	ΔE_0, eV
1	Fe-B	7.32	2.05	0.022	-0.995
2	Fe-Fe	1.06	2.41	0.013	0.877
3	Fe-Fe	1.96	2.47	0.008	-0.953
4	Fe-Fe	2.95	2.66	0.028	1.023
5	Fe-Fe	3.90	2.78	0.019	-1.920
6	Fe-B	2.00	3.56	0.030	5.051
7	Fe-B	3.12	3.80	0.010	-3.008
8	Fe-Fe	2.36	3.81	0.014	0.778
9	Fe-Fe	3.99	4.03	0.009	2.994
10	Fe-Fe	7.00	4.19	0.030	5.060

Table 3.2.4.2 Results of EXAFS fit for the sample Fe-1

N	Bond	CN	R, Å	σ^2, Å^2	ΔE_0, eV
1	Fe-B	6.30	2.11	0.013	2.419
2	Fe-Fe	0.78	2.24	0.011	7.293
3	Fe-Fe	3.90	2.47	0.010	8.348
4	Fe-Fe	2.40	2.50	0.015	8.000
5	Fe-B	4.20	3.60	0.028	5.422
6	Fe-B	2.10	3.75	0.002	7.198
7	Fe-Fe	0.20	3.75	0.010	0.148
8	Fe-Fe	8.50	4.00	0.030	7.071
9	Fe-Fe	5.42	4.01	0.030	3.023
10	Fe-Fe	3.30	4.10	0.028	4.751

Table 3.2.4.3 Results of EXAFS fit for sample Fe-3

According to SEM investigation, products of borohydride reduction of iron salts in aqueous solution consist of agglomerated nanoparticles of size from 20 to 150 nm.

From IR, XANES and EXAFS can be concluded that samples Fe-1 and Fe-3 are mainly iron borides, while samples Fe-2 and Fe-4 contain mainly iron borates. The experiment was reiterated (Table 3.2.3.1) giving exactly the same results. The products of borohydride reduction are not only iron as it was reported in [71] and not only amorphous Fe-B [75, 76]. We have found that it is a mixture of iron boride, iron borate and maybe iron. The formation of products is crucially determined by the Fe^{2+} concentration, another important parameter is the reaction time [67]. The possible mechanism of the reduction transition metals ions by sodium borohydride under formation of transition metals borides and borates have been described by Glavee et al. for Co^{2+} ions [71].

3.2.5 Synthesis in reverse micelles

In principle the reverse micelles method is a modification of the method reported above. Metal salts are reduced with $NaBH_4$ in water, but now the reaction volume is limited. The reaction takes place in small water droplets which are dispersed in isooctane and stabilized with a layer of a surfactant consisting of molecules which are hydrophilic at one end and hydrophobic at the other. The schematic view of the molecule of the surfactant sodium bis(2-ethylhexyl)sulfosuccinate (NaAOT) is shown below (Fig. 3.2.5.1 [82]).
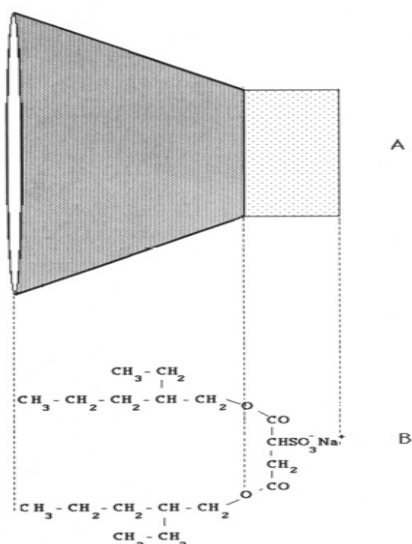
Fig. 3.2.5.1 Schematic view of the surfactant molecule (NaAOT) forming reverse micelles [82]

The size of the product depends strictly on the size of the reaction volume (of the water droplet). If σ is an area of a polar (hydrophilic) surfactant molecule's head, the radius of the water droplets can be described as [82]:

$$R_w = 3V_{aq}[H_2O]/\sigma[S]$$

where V_{aq} is the volume of water molecules.

Various experiments [82] showed that the water pool radius depends linearly on the water molar content, and does not depend (at a given water molar content) on the polar volume fraction. When the surfactant is sodium bis(2-ethylhexyl)sulfosuccinate the water pool radius can be described as:

$$R_w(\text{Å}) = 1.5w$$

where w is a molar ratio water to surfactant.

In a some range of R_w the size of the particles also depends linearly on w. The example for Cu metallic particles can be seen on the next picture (Fig. 3.2.5.2 [82]).
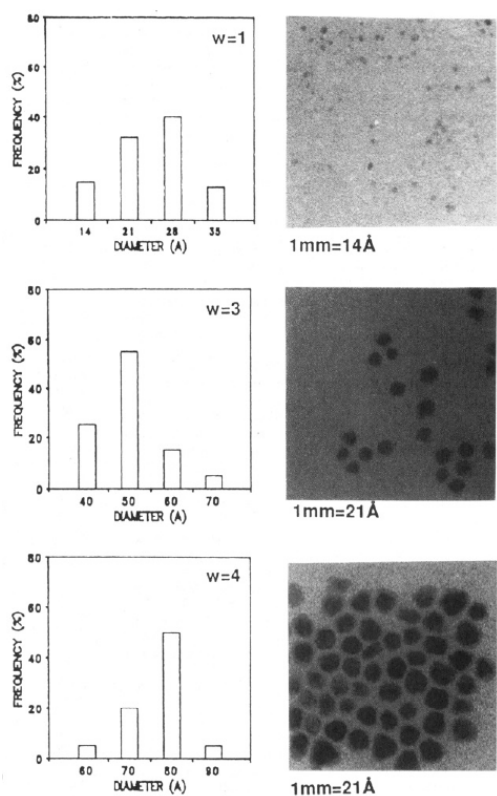
Fig. 3.2.5.2 Size histogram and electron microscopy picture of copper particles at various water contents in AOT-water-isooctane solution [82]

To induce the reaction usually two reverse micelles solutions, with different reactants and the same water pool radii, are prepared and mixed; the mechanism of exchanging reactants between two micelles of different solutions is illustrated in the next figure (Fig. 3.2.5.3 [83]).
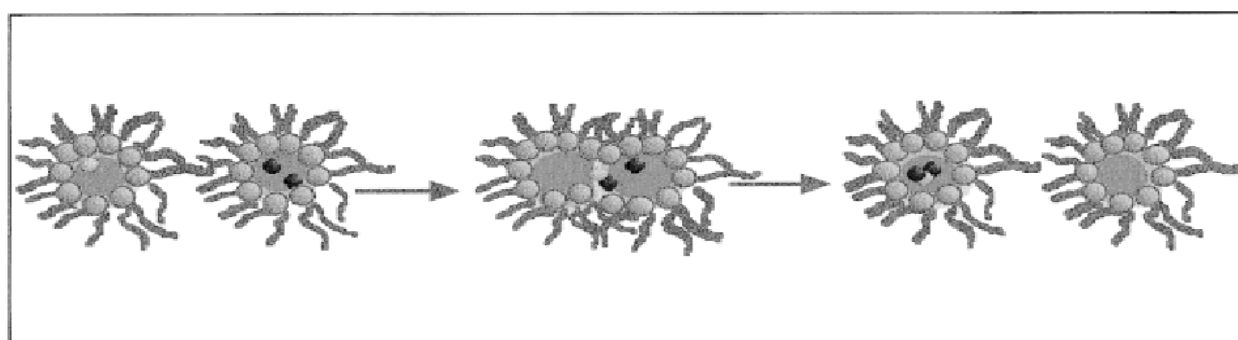
Fig. 3.2.5.3 Mechanism of interaction between two reactants in reverse micelles solutions [83]

After mixing the solutions accidental collisions between the reverse micelles take place, and after an exchange of the micelle content the reaction starts.

The whole synthesis procedure was performed in argon atmosphere. All solvents used in the synthesis (water, isooctane, ethanol) had been degassed before. In the first five reactions Fe(AOT)$_2$ and NaAOT (0.006 mol) were solved in 25 ml of isooctane in a 100-ml flask

attached to a vacuum-argon line. Then the calculated amount of water depending on the [H$_2$O]/[AOT] ratio was added. The reducing agent (NaBH$_4$ or LiBH$_4$) was solved in the same amount of water and added to another solution of NaAOT (0.006 mol) in 25 ml of isooctane in a 100-ml flask attached to a vacuum-argon line. Both solutions were mixed under vigorous stirring, then the stirring was continued for one hour. Then trioctylphospine (TOP) was added (4 µl/ml) and the precipitations were washed three times with ethanol, and then were redispersed in a non-polar solvent (toluene, chloroform).

The first experiments yielded in amounts to small to analyze.

To increase the amount of product, in the next three syntheses (samples Fe-B-2, Fe-B-3, Fe-B-4) the concentration of starting materials were increased ten times, and different ratios [H$_2$O]/[AOT] were tested. The synthesis of Fe(AOT)$_2$ is quite complex and expensive in money and time, so it was replaced by FeSO$_4$·7H$_2$O and FeCl$_2$·4H$_2$O.

Now FeSO$_4$·7H$_2$O or FeCl$_2$·4H$_2$O were solved in the necessary amount of water depending on the [H$_2$O]/[AOT] ratio and added to a solution of NaAOT (0.006 mol) in 25 ml of isooctane in a 100-ml flask attached to a vacuum-argon line.

Another improvement was the substitution of NaBH$_4$ by LiBH$_4$, because all lithium salts are soluble in ethanol and can easily be removed by washing.

Sample	Iron salt	Conc. of iron salt, mol	Red. agent	Conc. of red. agent, mol	$[H_2O]/[AOT]$
Fe-B-0	$Fe(AOT)_2$	0.001	$NaBH_4$	0.002	10
Fe-B-1	$Fe(AOT)_2$	0.001	$NaBH_4$	0.002	10
Fe-B-2	$Fe(AOT)_2$	0.01	$NaBH_4$	0.02	5
Fe-B-3	$Fe(AOT)_2$	0.01	$NaBH_4$	0.02	10
Fe-B-4	$Fe(AOT)_2$	0.01	$NaBH_4$	0.02	20
Fe-B-5	$FeSO_4 \cdot 7H_2O$	0.01	$NaBH_4$	0.02	5
Fe-B-6	$FeSO_4 \cdot 7H_2O$	0.01	$NaBH_4$	0.02	10
Fe-B-7	$FeSO_4 \cdot 7H_2O$	0.01	$NaBH_4$	0.02	20
Fe-B-8	$FeCl_2 \cdot 4H_2O$	0.01	$NaBH_4$	0.02	5
Fe-B-9	$FeCl_2 \cdot 4H_2O$	0.01	$NaBH_4$	0.02	10
Fe-B-10	$FeCl_2 \cdot 4H_2O$	0.01	$NaBH_4$	0.02	20
Fe-B-11	$FeCl_2 \cdot 4H_2O$	0.01	$LiBH_4$	0.02	5
Fe-B-12	$FeCl_2 \cdot 4H_2O$	0.01	$LiBH_4$	0.02	10
Fe-B-13	$FeCl_2 \cdot 4H_2O$	0.01	$LiBH_4$	0.02	20
Fe-B-12-1	$FeCl_2 \cdot 4H_2O$	0.01	$LiBH_4$	0.02	10
Fe-B-13-1	$FeCl_2 \cdot 4H_2O$	0.01	$LiBH_4$	0.02	20

Table 3.2.5.1 Reaction conditions

3.2.6 Characterization of products of synthesis in reverce micelles

An example of the produced nanoparticles produced is shown in Fig. 3.2.6.1-2.
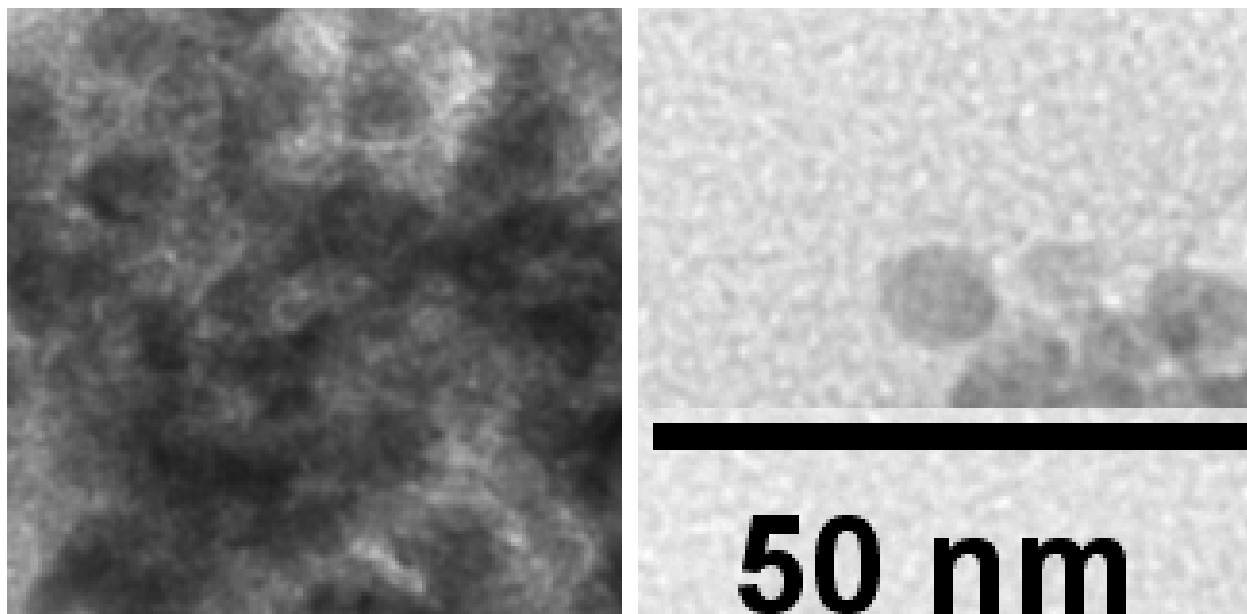
Fig. 3.2.6.1 TEM image of the sample Fe-B-9
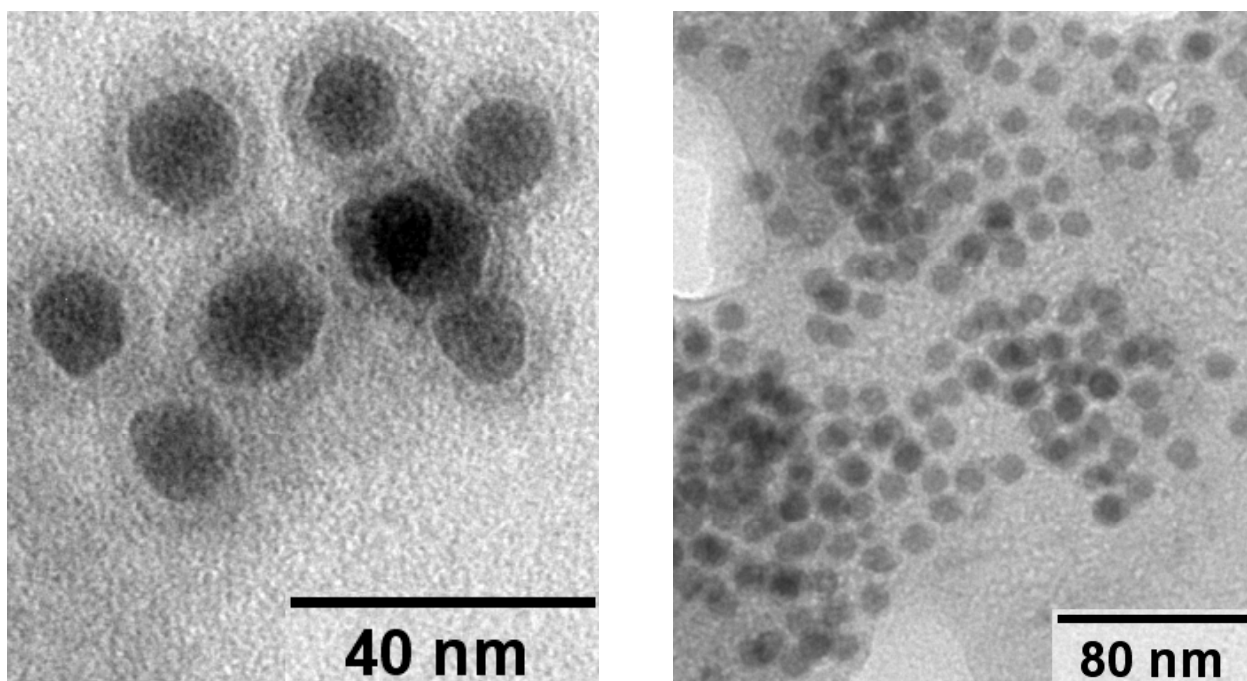
Fig. 3.2.6.2 TEM image of the sample Fe-B-13

The size of the nanoparticles can be controlled by the $[H_2O]/[AOT]$ ratio and was measured by TEM (Table 3.2.6.1).

[H$_2$O]/[AOT]	Size, nm
5	3
10	10
20	18

Table 3.2.6.1 Correlation between particle size and [H$_2$O]/[AOT] ratio

According to electron diffraction and XRD investigations the nanoparticles are amorphous. Sample Fe-B-12 was heated at 300 ºC in TOP for 30 minutes in order to enhance crystallinity, the results are shown below (Fig. 3.2.6.2). The electron diffraction pattern as seen in Fig. 3.2.6.3 looks similar to the metastable crystalline phases Fe$_3$B and Fe$_{23}$B$_6$ (Table 3.2.6.2). The semiquantitative ICP OES measurement for samples Fe-B-12 and Fe-B-13 showed a boron content relative to iron between 25 and 60 percent.
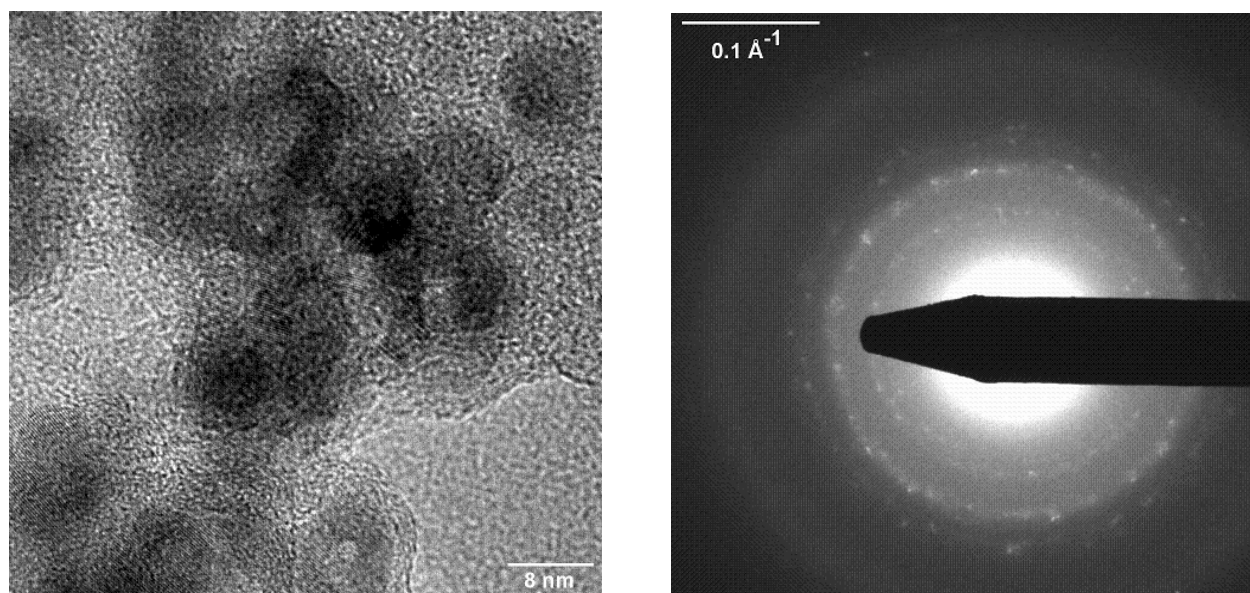
Fig. 3.2.6.3 TEM image and electron diffraction pattern of sample Fe-B-12 after annealing in TOP

Sample Fe-B-12		FeB		Fe$_2$B		Fe$_3$B		Fe$_{23}$B$_6$	
d(Å)	Int	d(Å)	Int	d(Å)	Int	d(Å)	Int	d(Å)	Int
2.69	10	2.59	100	2.55	82	2.68	25	2.69	8
2.41	50	2.27	45	2.12	100	2.38	100	2.41	39
1.84	100	1.80	35	1.62	99	1.80	75	1.82	46

Table 3.2.6.2 Comparing d values and intensities (from electron diffraction) of the annealed sample Fe-B-12 with those of crystalline iron borides (from ICSD [86, 125-127])

With EDX (all samples) and EELS (Fe-B-12) Fe, B, C, O, P and Na were detected. C, O, P and Na belong to the ligand agents.

According to ICP-OES the composition of samples Fe-B-12 and Fe-B-13 is $Fe_{100-x}B_x$ ($25 \leq x \leq 60$).

The fine structure of the B K-edge of sample Fe-B-12 is very similar to those of crystalline Fe_2B and $FeBO_3$ (Fig. 3.2.6.4). Therefore it is not possible to assign Fe-B-12 as iron boride or iron borate only by EELS. Iron has different oxidation states in iron borides and iron borates (0 and 2+/3+ respectively). The oxidation state can be measured with different kinds of spectroscopy, for example XANES or XPS.
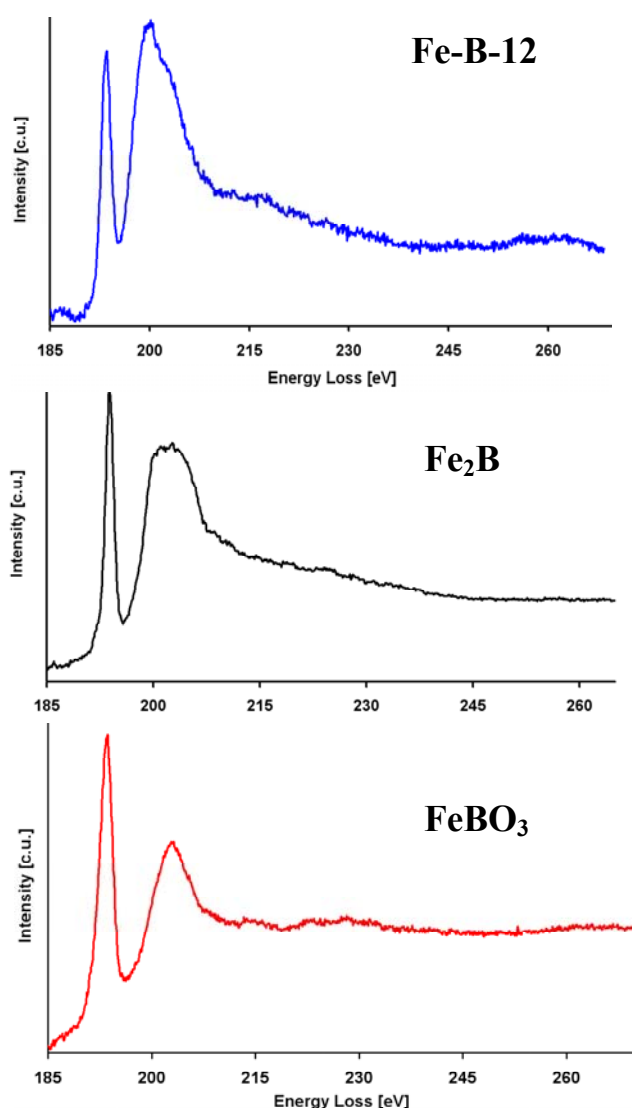
Fig. 3.2.6.4 Fine structure of the boron K-edge for Fe-B-12, Fe_2B and $FeBO_3$

From XANES investigations of sample Fe-B-12 the iron K-edge is located very similar to those of Fe_3BO_6 and $FeBO_3$, indicating the same oxidation state (3+). Also the fine structure

of the K-edge of the sample is like that of Fe_3BO_6 (Fig. 3.2.6.5). Obviously the synthesised nanoparticles are not air-stable and oxidized with time.
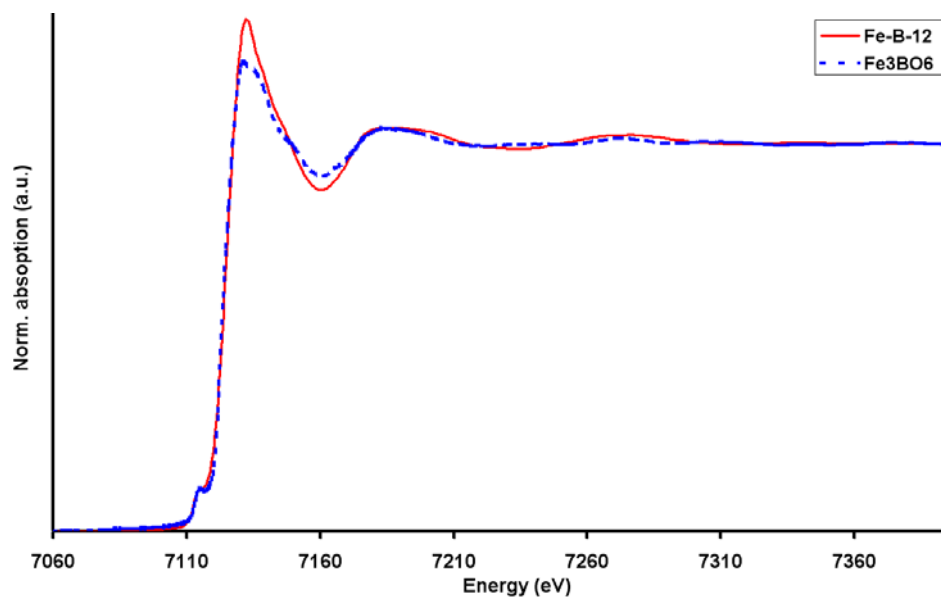
Fig. 3.2.6.5 K-edges (XANES) of sample Fe-B-12 and reference Fe_3BO_6

Amorphous nanoparticles of different sizes and with composition $Fe_{100-x}B_xO_?$ ($25 \leq x \leq 60$) can be synthesised they should be stored in inert atmosphere.

3.2.7 Synthesis in coordinating solutions

A general approach [94] of preparing monodisperse nanoparticles with < 5% standard deviation in size is a single, very short-term nucleation followed by slower growth of existing nuclei. It can be made by rapid addition of reagents into a reaction vessel containing a hot, coordinating solvent.

A suitable apparatus and dependences of nanoparticle size on the time of reaction are illustrated below (Fig 3.2.7.1 [94]).
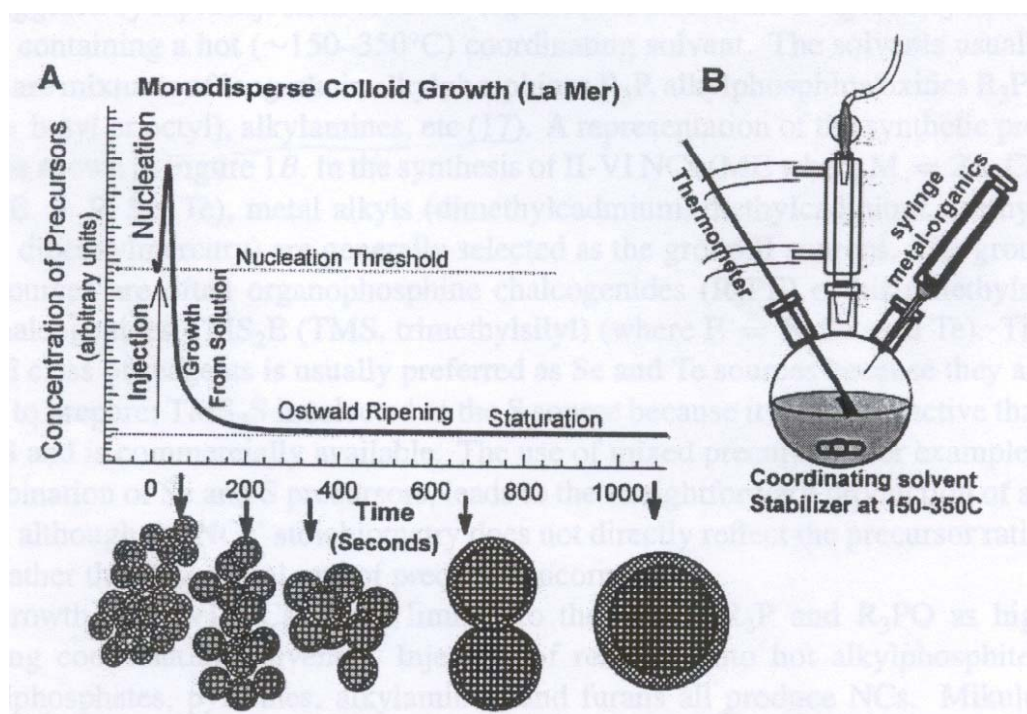
Fig 3.2.7.1 A) Stages of nucleation and growth, of nanoparticles

B) Representation of the synthetic apparatus employed in the preparation of monodisperse nanosized samples [94]

The temperature of the solution should be high enough either to decompose the reagents (e.g., when iron nanoparticles are synthesized from iron carbonyl [119]) or to start reaction between different reactants, depending on the respective synthesis. The nucleation of nanoparticles takes place immediately. After that the concentration of these species in the solution drops below the critical concentration necessary for nucleation, and further material can only add to already existing nuclei [94].

Another, alternative method of synthesis involves mixing reagents in the vessel at low temperature (low enough to prevent any appreciable reaction). A controlled increase in the solution temperature accelerates the chemical reaction and produces the necessary supersaturation with a following nucleation. When the temperature is adjusted to keep the rate at which the reagents react less than or equal to the rate at which material adds to already existing nuclei, the supersaturated state is never reached again and no new nuclei form. In both approaches, the size distribution of the nanoparticles is limited primarily by the short time interval in which the nuclei form and begin to grow [95].

By systematically adjusting the various parameters - time, temperature, concentrations and chemistry of starting materials, surfactants and solvents - it is possible to control the size of the nanoparticles. This offers possibilities to prepare a series of nanoparticles with the same

chemical composition but with different sizes and consequently with different physical properties. In general, the size of the nanoparticles increases with longer reaction time, addition of more materials to the surface of the nanoparticles and with increasing the reaction temperature as the rate of addition of materials to already existing nuclei increases. In many systems, a second, distinct growth stage known as Ostwald ripening, also takes place, in which the high surface energy of the smaller nanoparticles induces their dissolution while material is redeposited on the larger nanoparticles. This means that the average size of the nanoparticles increases with time, and their number decreases. The higher the temperature of the reaction solution, the stronger is the effect of Ostwald ripening, with consequently larger average nanoparticle size [95].

Another way of controlling nanoparticle size is to adapt the ratio of the concentrations of reagents, since higher stabilizer/reagent concentrations initially favor the formation of smaller nuclei and thus smaller nanoparticles [95].

The chemistry of the surface agents (stabilizers) can also be chosen to control the size of the nanoparticles. During the growth of nanoparticles, the stabilizer molecules in the solution adsorb reversibly to the surfaces of the nanoparticles, providing a dynamic organic shell (or capping layer) that stabilizes nanoparticles in the solution and mediates their growth. Stabilizing agents that bind more tightly to the surface of nanoparticles or have larger molecules providing greater steric hindrance (bulkier stabilizing agents) slow the rate of addition of materials to nanoparticles, reducing their average size. For example, using bulkier trioctylphosphines with a larger steric hindrance than more compact tributylphosphines slows down the growth of the particles [95].

A very effective strategy is to use a pair of stabilizers, one that binds tightly to the surface of nanoparticles, thus hindering growth, and another which is less tightly bound and permits rapid growth. For example, the accurate adjustment of the ratio of carboxylic acid (tightly bound) and alkylphosphine (weakly bound) surface agents permits the control of the growth rate and therefore the size of nanoparticles [95].

Another possibility of increasing the average size of nanoparticles is by supplying additional starting materials to a solution of growing nanoparticles. As long as the rate of addition of reagents does not exceed the rate of material addition to the nanoparticles, they continue to grow without creating new nuclei. This controlled addition of materials should be optimized in order to narrow down (focus) the size distribution of nanoparticles as material is added to all particles at nearly the same rate and makes for an initial variation in nanoparticle size that is small compared with the larger, final size of the particles [95].

After that, as nuclei reach the desired size, further growth can be prevented by cooling the reaction solution. The dispersions of nanoparticles are stable in the solution if the interaction between the capping groups and the solvent is favorable, providing an energetic barrier to neutralize the van der Waals and possible magnetic attractions between particles. The nanoparticles are then isolated from their reaction solutions by adding a non-solvent. The non-solvent should be miscible with the first, but because of its unfavorable interaction with the capping groups (hence "non-solvent"), it reduces the barrier to aggregation and destabilizes the dispersion of particles, causing their flocculation. Then it is centrifugued, resulting in a suspension which allows to decant the solvent and to isolate thus the powder of the nanoparticles. These powders consist of desired nanoparticles and their intimate organic capping layer and can be redispersed in a variety of solvents [95].

This general synthetic route, described above, can be optimized to yield distributions of sizes $\sigma<10\%$, which can then be further narrowed to $\sigma<5\%$ through size-selective precipitation. Size selective precipitation is a slow titration of a non-solvent into a dispersion of nanoparticles in order to bring part of them to flocculation. Because the largest particles experience the greatest attractive forces, they aggregate first. If the dispersed solution of particles is allowed to flocculate only partially, filtering or centrifuguing of the dispersion isolates precipitations enriched in the larger particles and leaves the smaller particles dispersed in the supernatant, which is then decanted. Additional non-solvent can be added to the supernatant in order to isolate a second fraction of smaller particles. The precipitates resulting after isolation can in turn be redispersed in a solvent and again be exposed recursively to this gentle destabilization/redispersion procedure to further narrow the sample size distribution [95]. The size selective precipitation procedure allows to receive a several fractions of nanoparticles of different size with a very small σ, for the further investigations of their physical properties depending on size.

The monolayer of organic stabilizing agents bound to the surface of nanoparticles can be exchanged with other competing stabilizing agents. Repeated exposure of the particles to an excess of the competing surface agents, followed by precipitation and redispersion in fresh solvent, isolates cap-exchanged particles. This process allows to adjust precisely the length and chemical functionality of the organic stabilizing agents [95], for example, to change the solubility of nanoparticles from non-polar solvents (toluene, chloroform and etc.) to water [121].

A two-neck 100 ml flask with argon output, a thermometer, a water cooler and overpressure valve was connected to a standard vacuum-argon line. It was evacuated three times by heating

(with a natural gas burner) up to approximately 70°C with argon rinses between, after this procedure it was always kept under argon overpressure.

Then 30 ml of a high boiling solvent (diphenylether, dioctylether or trioctylphosphine (TOP), boiling point 259°C, 287°C or 290°C, respectively) were filled into the flask and heated to boiling point with a heat mantel, accompanied by vigorous stirring, in a slow argon flow, for 10 minutes, in order to remove the water and other liquids with a low boiling point and dissolved gases (oxygen, nitrogen, hydrogen) from the solvent. It was cooled down to 30 °C, then 1 mmol of iron precursor (iron(II)chlorid-tetrahydrate or iron(II)acetylacetonate) and two of stabilizing agents (TOP and oleic acid, hexadecylamine and oleic acid etc.) in different ratios and concentrations were added. It was re-heated to boiling point, and in case of use of $FeCl_2 \cdot 4H_2O$ the hydrate water was evaporated in an argon flow at 200 °C.

At the same time the second reagent the oxygen-free solution of 2 mmol of $LiBH_4$ in 2 ml (of distillated) THF has to be dried thoroughly to exclude reaction of $LiBH_4$ with water was prepared in a different vessel. $LiBH_4$ serves both as a reduction agent and a boron precursor. $LiBH_4$ was chosen instead of $NaBH_4$, because the by-products of reaction with iron salts are well soluble in the organic solvents, which is not the case for $NaBH_4$.

The solution of $LiBH_4$ in THF is injected with a syringe into the reaction vessel through a plastic septum, the color of the solution changes immediately from light yellow (iron precursor-iron(II)chlorid-tetrahydrat) or light red (iron precursor-iron(II)acetylacetonat) to black. The solution was kept in a slow argon flow for 5 minutes in order to remove the THF. Then it was kept boiling and vigorously stirred in a slight argon overpressure for another 20 to 100 minutes.

After that it was cooled down to room temperature, by removing the heating.

The reaction solution was diluted with the same amount of chloroform, homogenized in an ultrasonic bath and centrifugued at 4000 rotations/minute for 5 minutes. The supernatant with nanoparticles was isolated. Then the black precipitation from the supernatant was isolated by adding a nonsolvent (ethanol or methanol) and centrifuguing, washed with ethanol and redispersed in one of the non-polar solvents (chloroform or toluene).

The other type of synthesis tried was, in principle, the same route but with trioctylphosphine both as solvent and stabilizing agent. In this case, the dried flask was filled with 30 ml of trioctylphosphine (boiling point 290° C) and heated under vigorous stirring, by a heat mantle to boiling point in a slow argon flow for 10 minutes in order to remove the water and other easely boiling liquids and dissolved gases. Then it was cooled down to 30 °C, and 1 mmol of iron precursor ($FeCl_2 \cdot 4H_2O$ or $Fe(acac)_2$) was added. It was re-heated to the boiling point.

When $FeCl_2 \cdot 4H_2O$ was used, the water was removed via distillation in an argon flow at 200 °C. The parameters of example syntheses are shown below:

Sample	Iron salt	LiBH$_4$	1-stabilizer	2-stabilizer	Solvent	Synthesis temperature	Duration of reaction
Fe-B-0402	$FeCl_2 \cdot 4H_2O$, 1 mmol	2 mmol	TOP, 30 ml			288 – 290 °C	30 min
Fe-B-1103	$FeCl_2$ 1 mmol	2 mmol	HDA, 2 mmol	Oleic acid, 1 mmol	Diphenylether	257 – 259 °C	30 min
Fe-B-0505	$Fe(acac)_2$, 1 mmol	2 mmol	TOP, 30 ml			288 – 290 °C	40 min
Fe-B-3006	$Fe(acac)_2$, 1 mmol	2 mmol	HDA, 2 mmol	Oleic acid, 2 mmol	Dioctylether	286 – 287 °C	20 min
Fe-B-0507	$Fe(acac)_2$, 1 mmol	2 mmol	HDA, 2 mmol	Oleic acid, 2 mmol	Diphenylether	257 – 259 °C	20 min
Fe-B-0607	$Fe(acac)_2$, 1 mmol	2 mmol	HDA, 2 mmol	Oleic acid, 2 mmol	Diphenylether	257 – 259 °C	20 min
Fe-B-1307	$Fe(acac)_2$, 1 mmol	2 mmol	HDA, 2 mmol	Oleic acid, 2 mmol	Diphenylether	257 – 259 °C	20 min
Fe-B-1707	$Fe(acac)_2$, 1 mmol	2 mmol	HDA, 2 mmol	Oleic acid, 2 mmol	Dioctylether	286 – 287 °C	45 min
Fe-B-2807	$Fe(acac)_2$, 1 mmol	2 mmol	HDA, 1 mmol	Oleic acid, 1 mmol	Dioctylether	286 – 287 °C	20 min
Fe-B-0708	$FeCl_2 \cdot 4H_2O$, 1 mmol	2 mmol	HDA, 4 mmol	Oleic acid, 2 mmol	Diphenylether	257 – 259 °C	25 min
Fe-B-0808	$FeCl_2 \cdot 4H_2O$, 1 mmol	2 mmol	HDA, 4 mmol	Oleic acid, 4 mmol	Diphenylether	257 – 259 °C	20 min
Fe-B-1511	$Fe(acac)_2$, 1 mmol	2 mmol	HDA, 2 mmol	Oleic acid, 2 mmol	Dioctylether	286 – 287 °C	45 min
Fe-B-2011	$Fe(acac)_2$, 1 mmol	2 mmol	HDA, 2 mmol	Oleic acid, 2 mmol	Dioctylether	286 – 287 °C	45 min

Table 3.2.7.1 Reaction conditions

The samples Fe-B-1511 and Fe-B-2011 were synthesized exactly the same way as sample Fe-B-1707 but stored after the synthesis in inert gas atmosphere.

3.2.8 Characterization of products after synthesis in coordinating solvents

The methods which were used for the characterization of the samples are listed below (Table 3.2.8.1).

Sample\Method	ICP-OES	EELS	EDX	XPS	XAS	TEM	SEM	Magn. meas.
Fe-B-0402	X		X		X	X	X	
Fe-B-1103			X		X	X		
Fe-B-0505	X		X			X		
Fe-B-3006		X		X	X			
Fe-B-0507		X	X	X	X	X		
Fe-B-0607		X	X	X	X	X		
Fe-B-1307			X	X		X		
Fe-B-1707		X	X	X		X	X	X
Fe-B-2807			X	X		X		
Fe-B-0708			X	X		X		
Fe-B-0808			X	X		X		
Fe-B-1511			X	X			X	X
Fe-B-2011			X	X			X	X

Table 3.2.8.1 Characterization methods and samples for that they were applied

The results were black precipitates, which could be redispersed in non-polar solvents to obtain transparent solutions. This proves the unambiguous presence of nanoparticles.
According to ICP-OES, EELS (only for the samples prepared without trioctylphosphine) and XPS they contain iron, boron and elements which belong to the stabilizing agents.

TEM investigations provide the information that the nanoparticles are mainly round and sized between 4 and 12 nm.

The following illustrations (Fig 13.4.1-6) show examples of nanoparticles. No correlation between the concentration of stabilizing agents, their ratio (in the investigated range, 0.5-4 mmol), duration of reaction and size of the particles was found. For the sample Fe-B-1103 a very wide particle size distribution, from 4 to 12 nm, was found (Fig 13.4.1). The reason was that $FeCl_2$ used as iron precursor is a very bad soluble material and it was not solved completely before the start of the reaction. Later, only $Fe(acac)_2$ and $FeCl_2 \cdot 4H_2O$ were used. Unfortunately, it is impossible to gain much information from spectroscopic methods like EELS and XPS applied to samples prepared with trioctylphosphine as surface agent (Fe-B-0402, Fe-B-0505), because TOP contains phosphorous which has an energy edge very close to the K-edge of boron (Chapters 2.5.2 and 2.7.4).
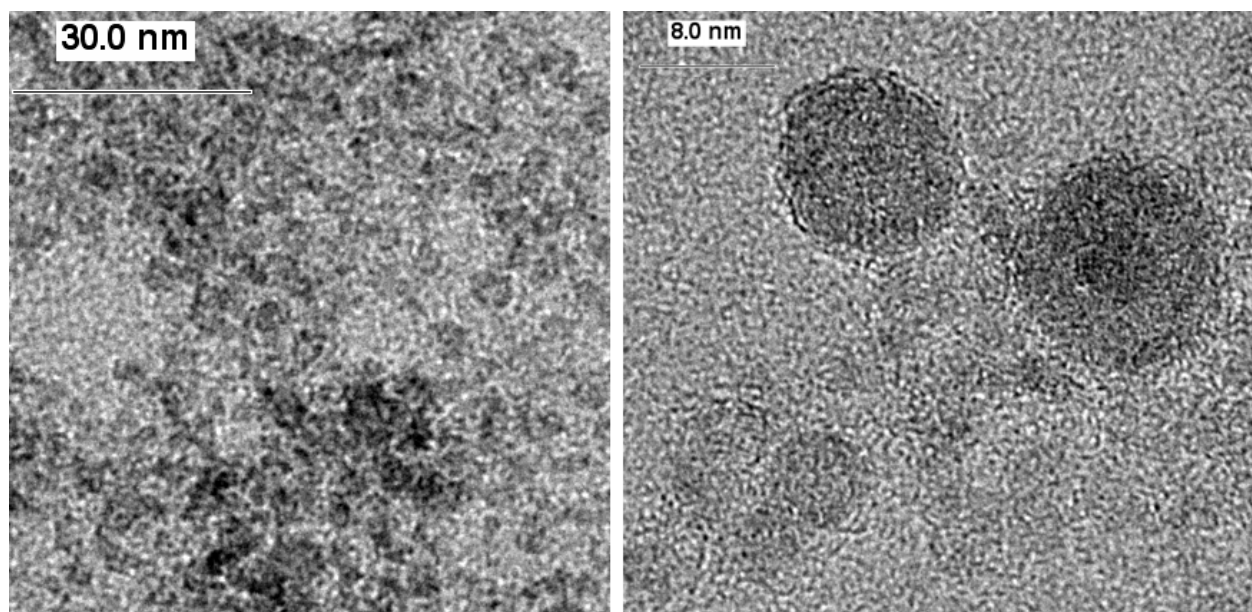
Fig 3.2.8.1 TEM image of sample Fe-B-1103
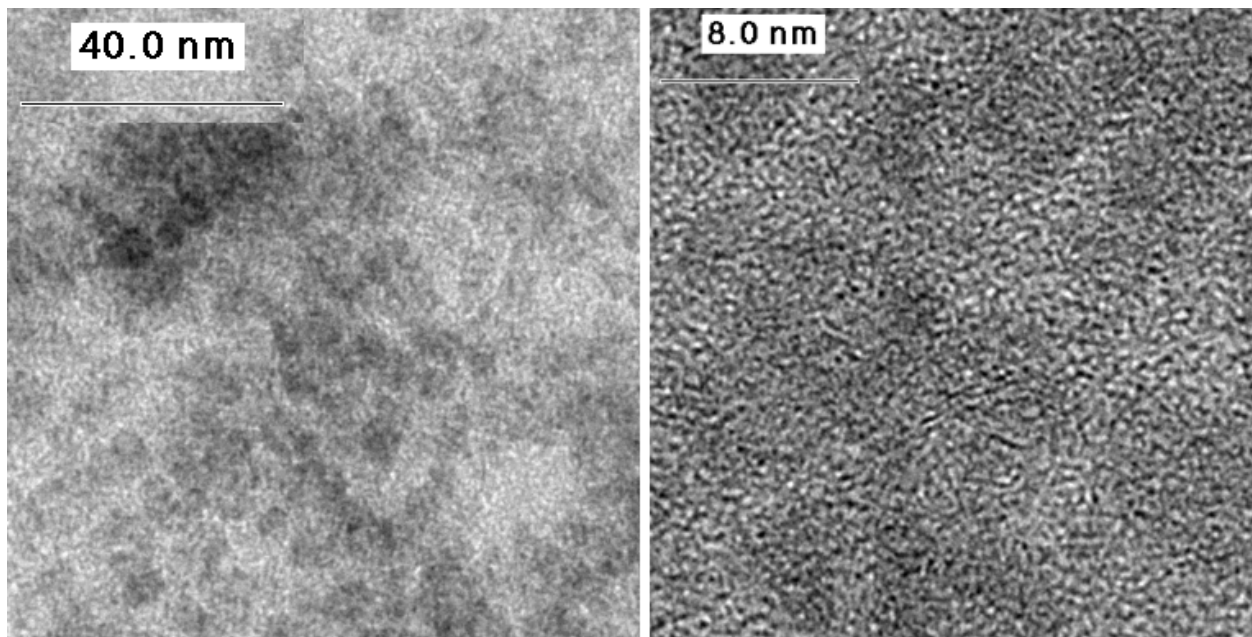
Fig. 3.2.8.2 TEM image of sample Fe-B-0507
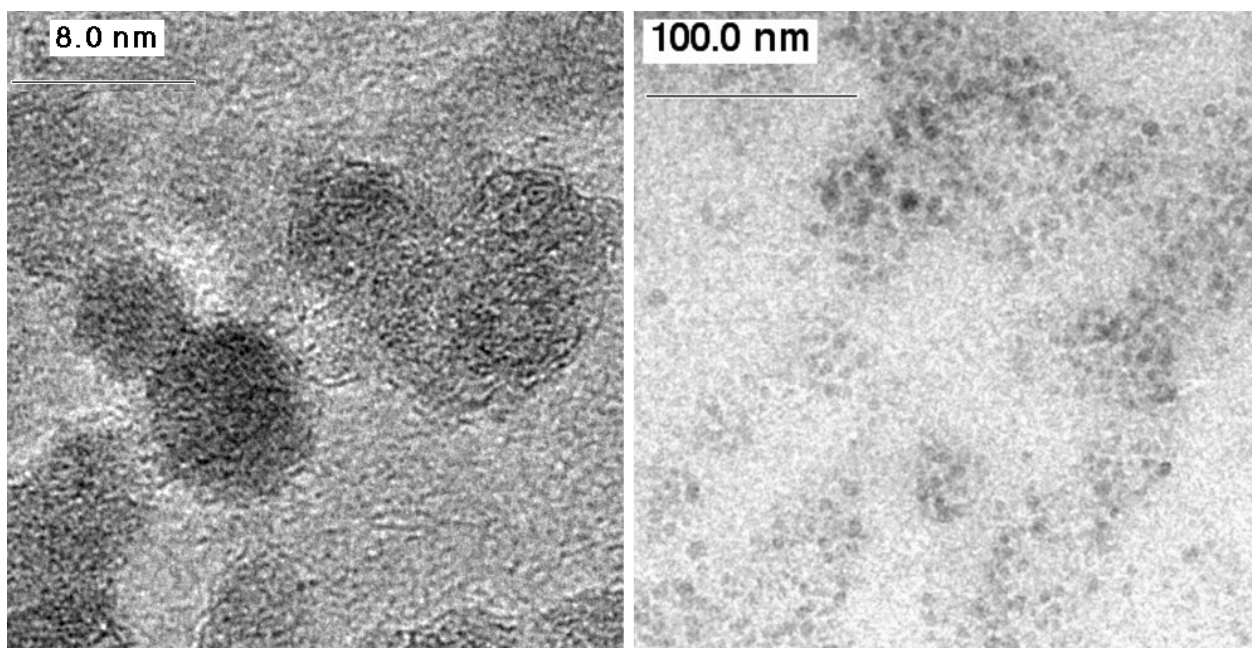
Fig 3.2.8.3 TEM image of samples Fe-B-0607 (left) and Fe-B-0808 (right)
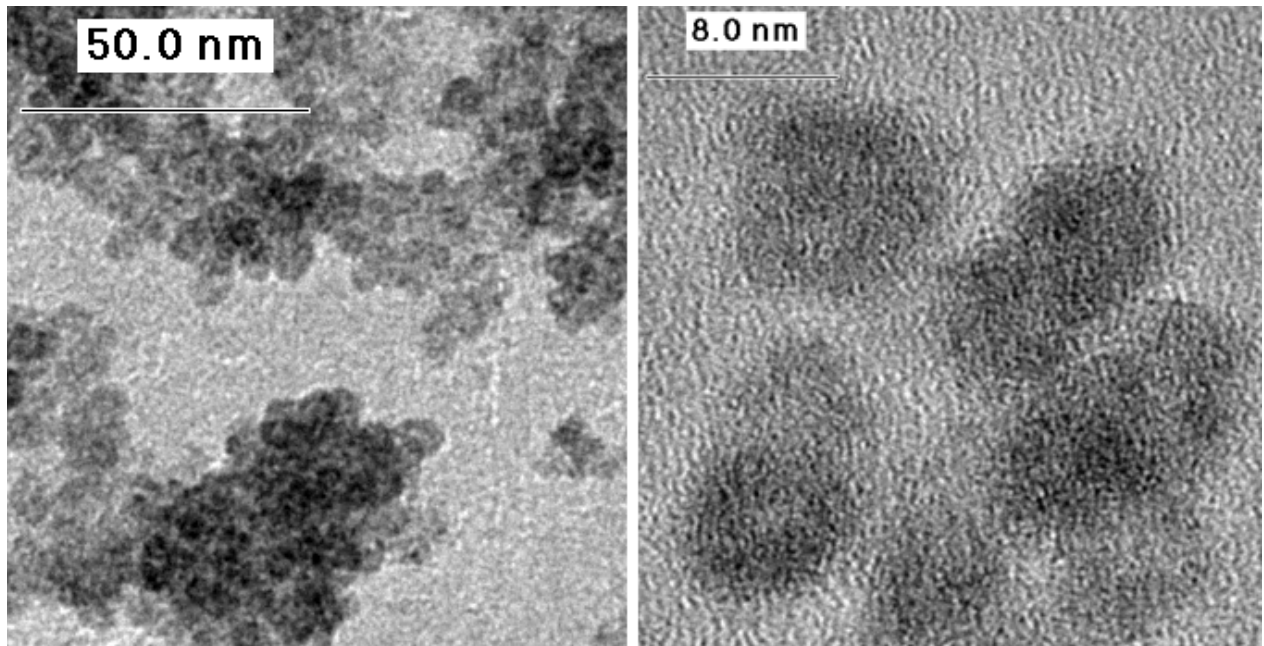
Fig 3.2.8.4 TEM image of samples Fe-B-1307 (left) and Fe-B-2807 (right)
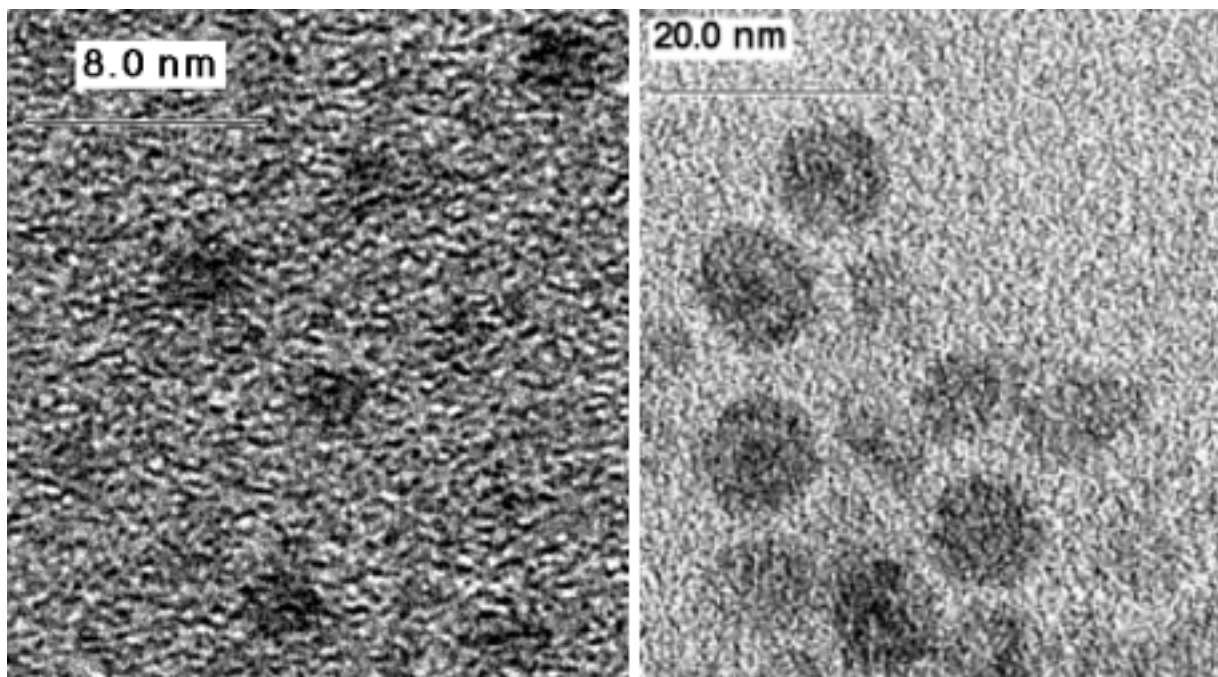
Fig 3.2.8.5 TEM image of samples Fe-B-1707 (left) and Fe-B-0708 (right)
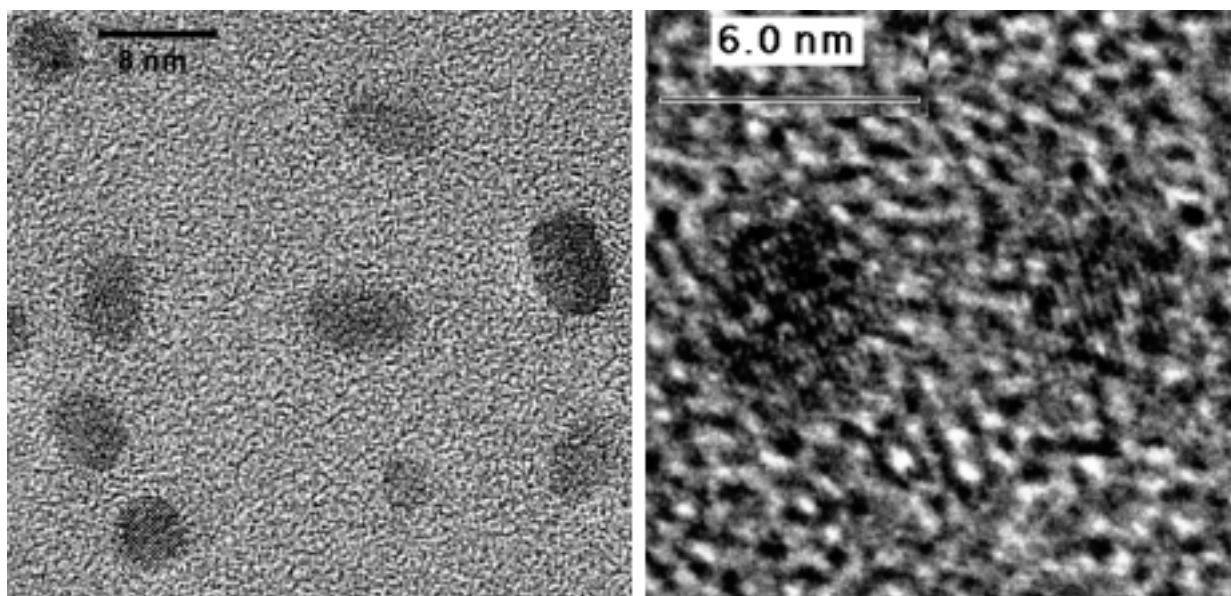
Fig 3.2.8.6 TEM image of sample Fe-B-0402 (left) and Fe-B-0505 (right)

The next illustration (Fig 3.2.8.7) shows the fine structure of the boron EELS K-edge of crystalline iron boride in comparison with one of the samples. As was described earlier in Chapter 2.7.4, structural similarity of the ionization edges of two compounds can be an indication of similar boron environments in these compounds. Unfortunately, the fine structure of the boron K-edge in borates also looks very similar to that of the borides and the sample.
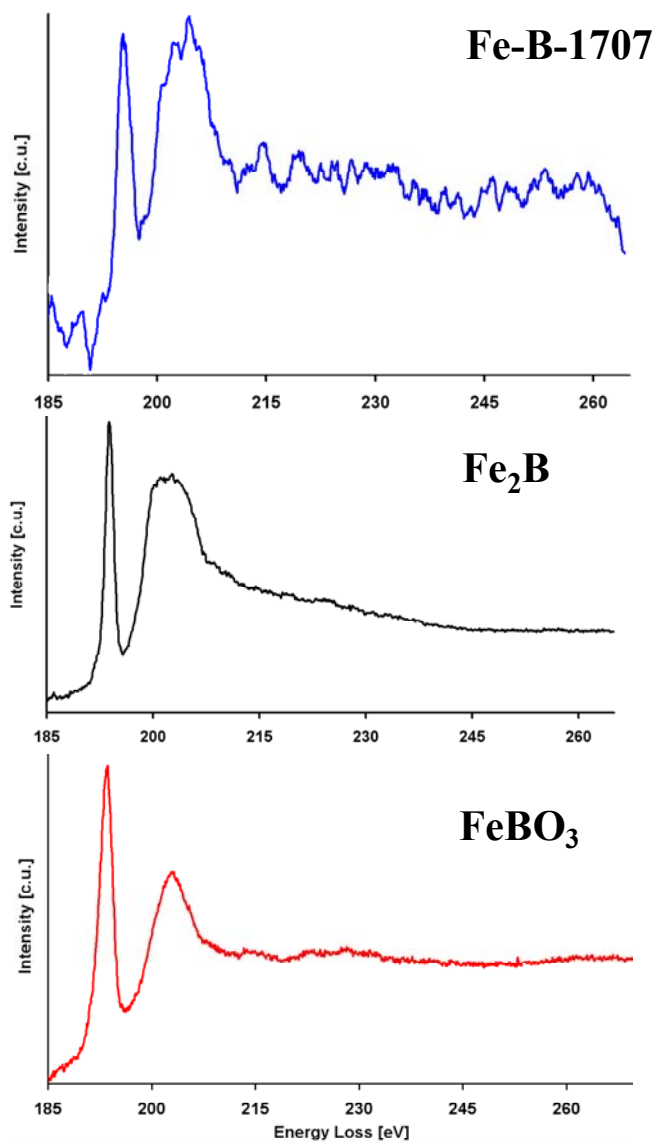
Fig. 3.2.8.7 Boron K-edge fine structure of sample Fe-B-1707 (above) and crystalline Fe_2B and $FeBO_3$ (below)

Due to this, it is impossible to distinguish between iron borides and iron borates with the exclusive use of EELS. However the presence of boron in the sample is proven.

One of the differences between borides and borates is, for example, the oxidation state of iron. Borides are formally metallic, and the oxidation states for both, Fe and B, are regarded as ±0 [133]. In the case of borates Fe is +2 ($Fe(BO_2)_2$) or +3 (e.g. $FeBO_3$, Fe_3BO_6).

Spectroscopic methods offer a reliable way to measure oxidation states. In this work XAS and XPS were used for this purpose, where the position of the iron edges depends on their oxidation state as it was mentioned above (Chapter 2.5.2 and 2.6.2).
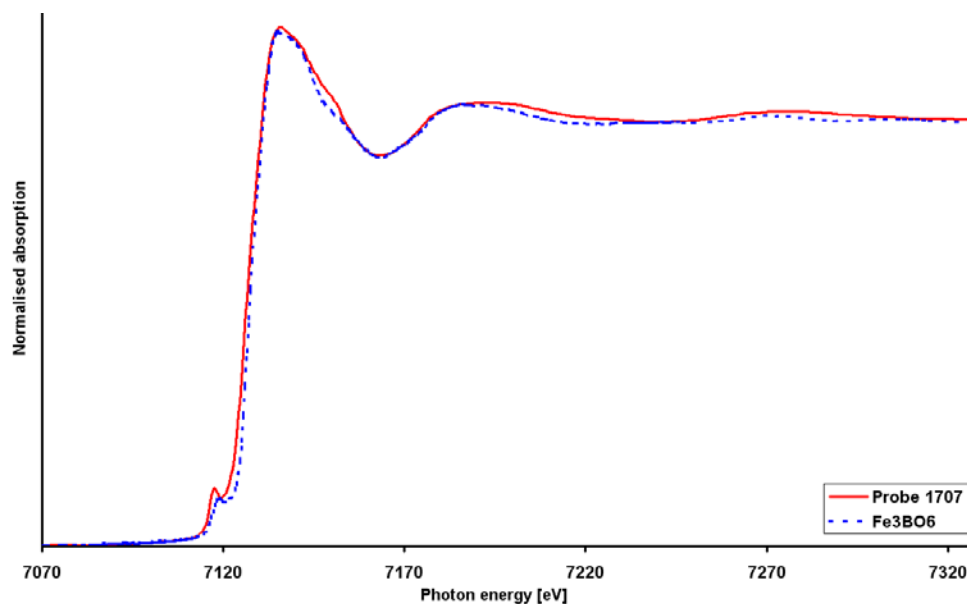
Fig. 3.2.8.8 Iron k-edge (XANES) fine structure of sample Fe-B-1707 and crystalline Fe_3BO_6

This illustration (Fig 3.2.8.8) shows an example of a XAS iron K-edge of one of the samples (Fe-B-1707 more than three days after the synthesis) and one of the reference compounds (Fe_3BO_6). It can be seen that the structure and position of the K-edges are almost identical. The next picture (Fig 3.2.8.9) shows the iron peaks (2p 3/2 and 2p 1/2) of the same sample (Fe-B-1707 more than three days after the synthesis) and of Fe_3BO_6; their positions correlate to the oxidation state of iron so both samples should contain iron as Fe^{3+}.
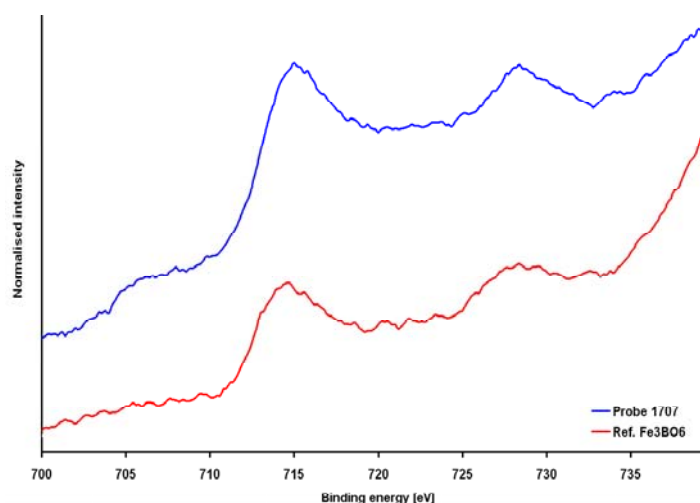
Fig. 3.2.8.9 XPS iron p-edge fine structure of sample Fe-B-1707 and crystalline Fe_3BO_6, the position of iron 2p 3/2 peak of the sample is 715 eV exactly as for Fe_3BO_6 indicating the same oxidation state

XPS measurements performed just one or two days after synthesis, indicate the same iron oxidation states for iron borides and sample 1707 (Fig 3.2.8.10). So the layer of stabilizing

126

ligands preserves the sample against immediate oxidation but oxidation takes place within three days.
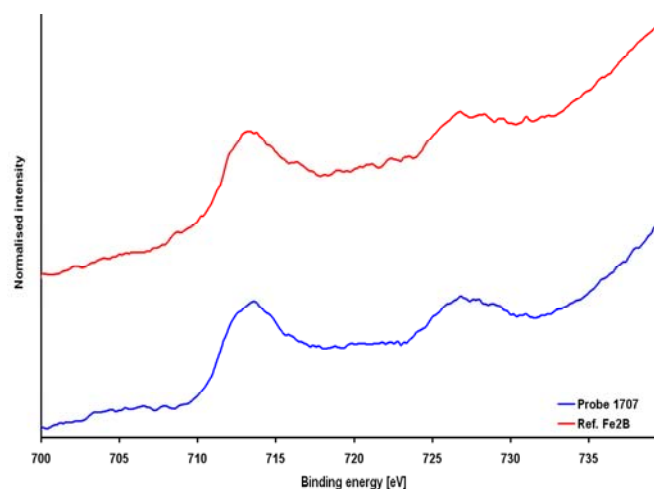
Fig. 3.2.8.10 XPS iron p-edge fine structure of sample 1707 (immediately after synthesis) and crystalline Fe_2B, the position of iron 2p 3/2 peak of the sample is 713 eV exactly as for Fe_2B indicating the same oxidation state

It was assumed that in the air samples are slowly oxidized, producing amorphous iron borates with a local structure very close to Fe_3BO_6. The parameters of the local structure were fitted from EXAFS spectra using the Fe_3BO_6 parameters as a first approximation. The EXAFS fit is shown in the next illustration (Fig 3.2.8.11).
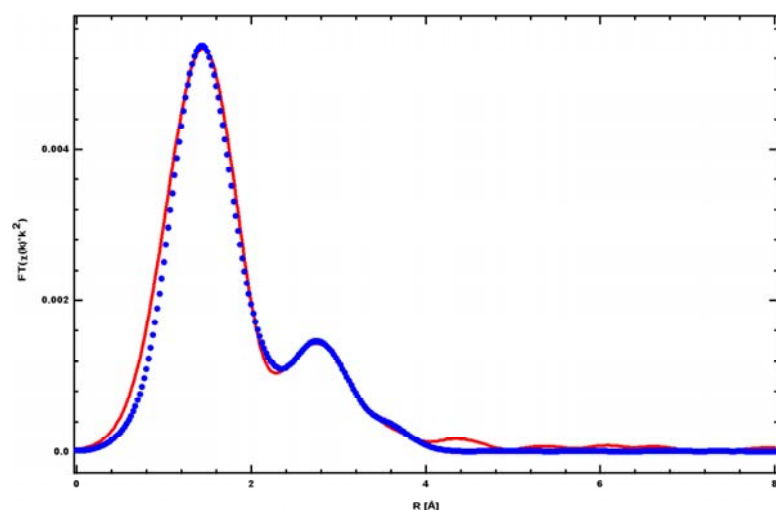
Fig. 3.2.8.11 EXAFS fit (blue dashed line) for sample Fe-B-1707 (more than three days after the synthesis, red line).

N	Bond	CN	R, Å	σ^2, Å^2	ΔE_0, eV
1	Fe-O	1.12	1.86	0.004	2.736

2	Fe-O	0.81	1.89	0.003	2.736
3	Fe-O	1.10	1.93	0.007	0.800
4	Fe-O	1.44	2.02	0.007	0.800
5	Fe-O	3.68	2.08	0.023	-7.000
6	Fe-B	1.56	2.58	0.001	5.948
7	Fe-Fe	1.40	2.74	0.010	-5.308
8	Fe-B	1.38	3.04	0.002	0.802
9	Fe-B	2.33	3.05	0.002	0.802
10	Fe-Fe	6.00	3.08	0.034	2.354

Table 3.2.8.2 Results of EXAFS fit for the sample Fe-B-1707

The parameters of the local structure for the first 10 coordination shells are listed in table 3.2.8.2.

Iron borates are weak ferromagnetic materials [96-98]. Until now there are no works investigating the magnetic behavior of iron borates of nano-scale size. Sample Fe-B-1707 which was identified to be amorphous Fe_3BO_6 by XPS and XANES experiments, was now investigated concerning its magnetic properties. Two fractions of the sample were precipitated, one with particles of 6 nm in diameter, the other with particles of 8 nm in diameter according to SEM, using the standard size selective precipitation procedure (Fig. 3.2.8.12).
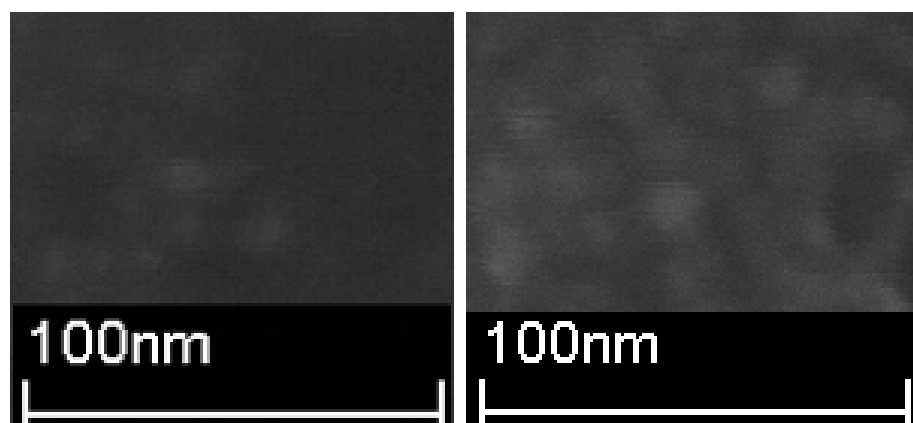
Fig. 3.2.8.12 SEM images of sample Fe-B-1707, fraction 6 nm (left) and fraction 8 nm (right)

In Fig. 3.2.8.13-3.2.8.14 the magnetic moment as function of applied field for both the fractions is shown. There can be seen the values of magnetization and the temperatures of the transition from super-paramagnetic state to the ferromagnetic one (blocking temperature).
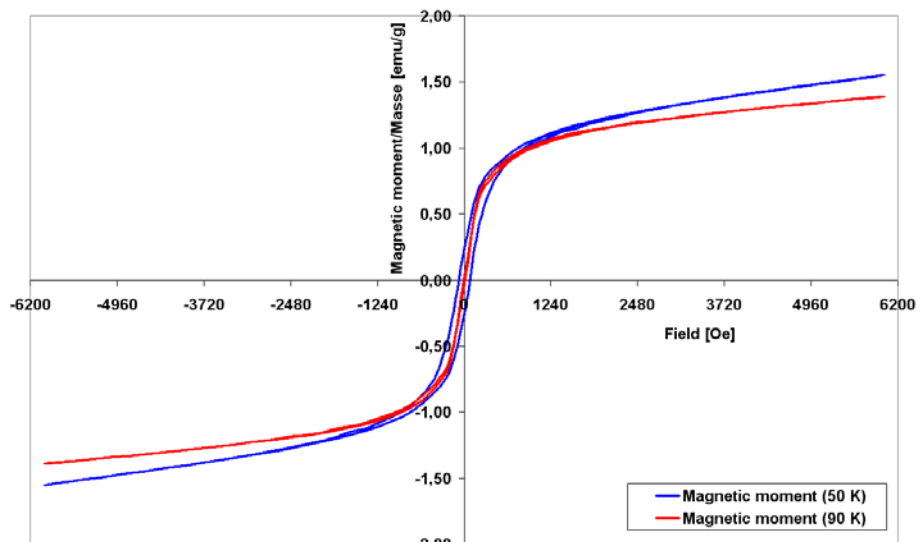
Fig. 3.2.8.13 Magnetic moment as function of applied field for the sample Fe-B-1707 (6 nm)
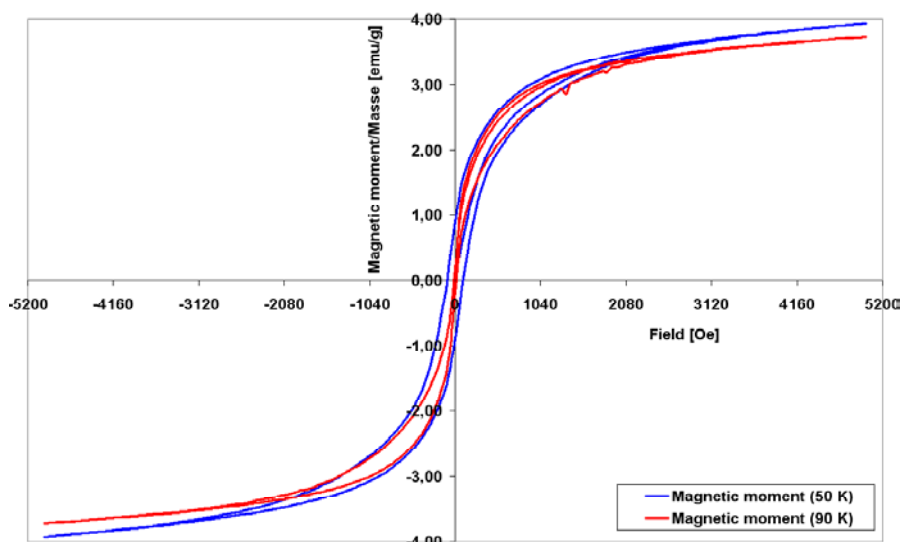
Fig. 3.2.8.14 Magnetic moment as function of applied field for the sample Fe-B-1707 (8 nm)

The value of the magnetic moment increases with the size of the particles and is relatively small (4 emu/g) compared with, e.g., nanoparticles of iron oxides of the same size [99, 100], where it is almost six times bigger (15 emu/g). On the other hand, the blocking temperature of iron borate nanoparticles is about five times higher compared to iron oxides of 7 nm in size [99]. Other XPS measurements were carried out under air-free conditions on an iron boride (samples 2011 and 1511).

Using the standard size selective precipitation procedure, the particles were divided into 8, 10, and 12 nm parts. The size of the particles was determined by SEM (Fig. 3.2.8.9).
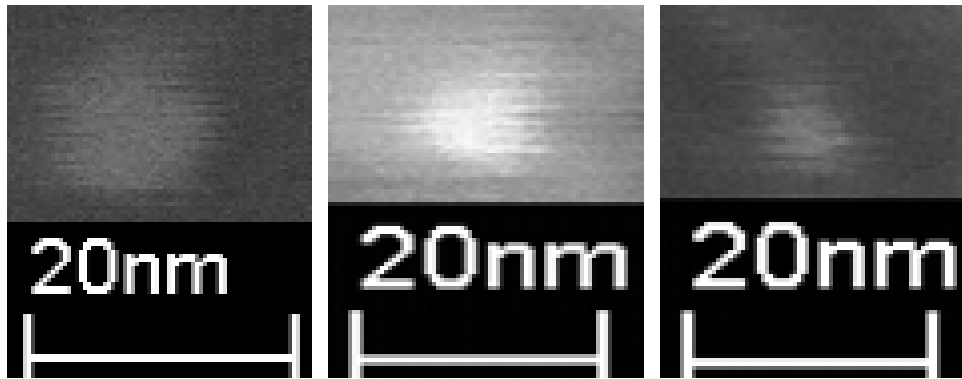
Fig. 3.2.8.15 SEM images of samples Fe-B-1511 and Fe-B-2011, fraction 12 nm (left), 10 nm (middle) and fraction 8 nm (right)

The values of magnetization and the blocking temperatures can be seen in Fig. 3.2.8.16-3.2.8.18.
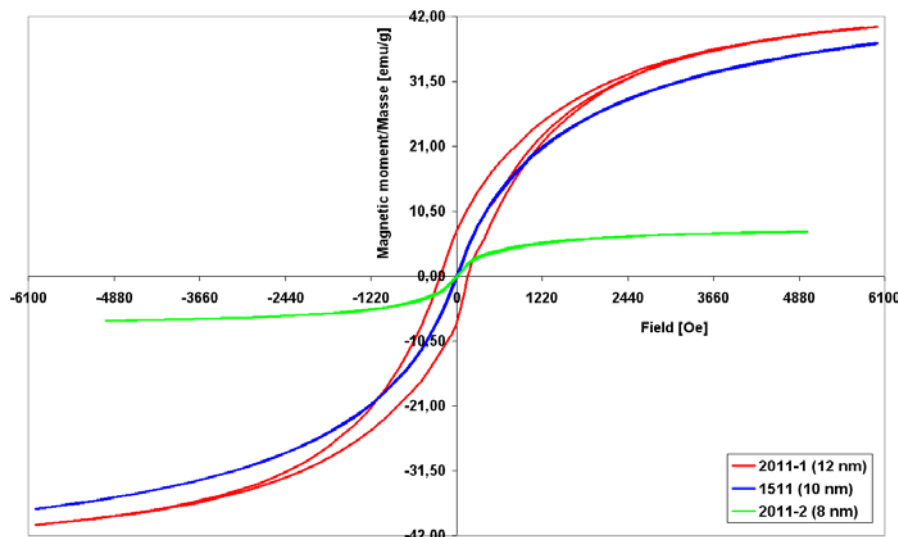
Fig. 3.2.8.16 Magnetic moment as function of applied field for the samples of 8, 10 and 12 nm size at room temperature

As seen in the illustration above, for this iron boride the value of the magnetic moment is already of the same order as for iron oxide particles [99, 100]. The most remarkable result is that 12 nm particles are ferromagnetic at room temperature.
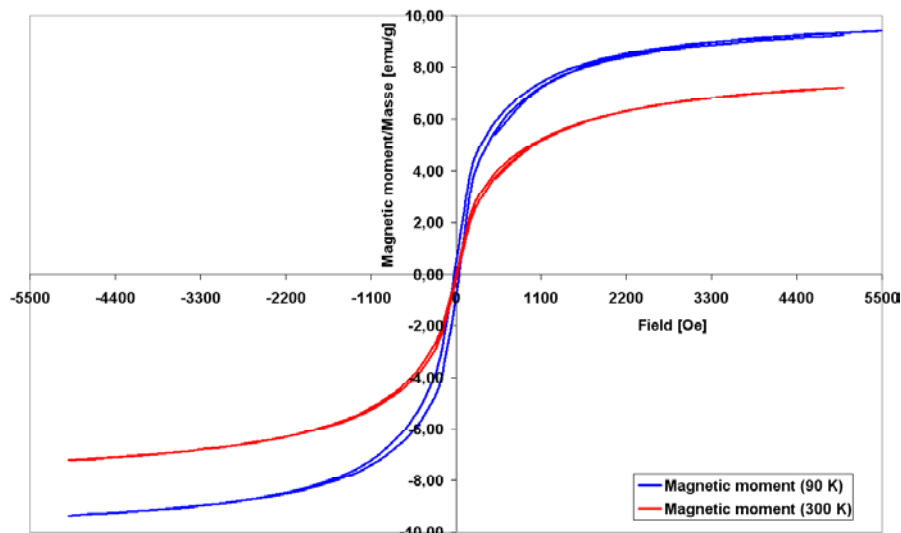
Fig 3.2.8.17 Magnetic moment as function of applied field for the sample Fe-B-2011-2 (the particles of 8 nm size)
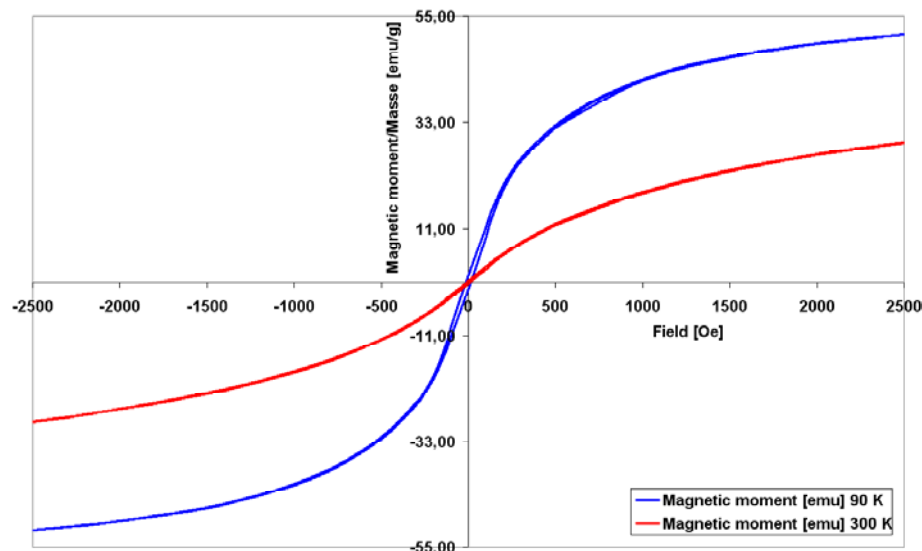
Fig 3.2.8.18 Magnetic moment as a function of applied field for the sample Fe-B-1511 (the particles of 10 nm size)

Fig. 13.4.13-14 indicate that the blocking temperature of 8 and 10 nm particles size lies between 90 and 300 K, which is considerably higher than for iron oxides of 7 nm size [99] and for iron nanoparticles of 7 nm size [119]. Actually, the term "blocking temperature" is not completely correct in the context of these samples; both (1511 and 2011-2) are also ferromagnetic at room temperature, but coercivity (B_c) is negligible in the range of 10 emu/g.

3.2.9 Summary

The products of synthesis in water were always fine, black, pyrophoric powders. They were characterized by XRD, IR, XAS, EDX and SEM. According to XRD and SEM showed that they consisted of amorphous agglomerated nanoparticles of an average size of about 50 nm. It was found that in the case of synthesis in water, the products of chemical reduction could be either iron borides or iron borates. Which product is formed depends on the iron concentration in the solution: if the concentrations is less than 0.3 mol the final product is iron borate, if it is higher mainly iron boride is obtained. Another very important parameter is the reaction time. When limiting the reaction time to 30-120 s., only pure iron was shown to have been formed according to XRD and EDX, no traces of boron were visible. No dependence on the ratio of starting materials was found.

From EDX measurements the chemical composition of the synthesised iron borides was found to be approximately $Fe_{100-x}B_x$ ($25 \leq x \leq 35$) which is in good agreement with results reported in [71, 75, 76, 77, 116, 117]. Their local structure was characterized via XAS.

In the case of synthesis in reverse micelles it can be concluded that it is possible to produce amorphous iron boride nanoparticles of the composition $Fe_{100-x}B_x$ ($25 \leq x \leq 35$) and diameter 3-18 nm. The diameter can be controlled via the $[H_2O]/[AOT]$ ratio. The particles were characterized using XRD, XAS, EDX, EELS, XPS and TEM.

The XANES method showed that the particles are not air-stable: stored under air they were oxidized slowly to Fe^{3+}-containing borates. Other preparative routes to obtain crystalline iron boride nanoparticles were investigated to be able to use the diffraction methods for characterization.

The most interesting results were obtained from the synthesis in coordinating solvents. By this method it is possible to synthesize crystalline iron boride nanoparticles with a diameter ranging from 3 to 12 nm. The samples were characterized via XAS, EDX, EELS, XPS and TEM. Their magnetic properties were investigated, and as expected the value of magnetization was found to be lower than for iron nanoparticles [119] but of the same order as in iron oxides [99, 100]. An unexpectedly high blocking temperature was observed, which is considerably higher than that of iron oxides of 7 nm size [99] and iron nanoparticles of the same size [119]. Iron boride nanoparticles are a very promising material for applications in magnetic storage systems. When exposed to air for a long time they are oxidized to iron borates with a lower blocking temperature und a much lower magnetic moment.

4 Conclusion

In the first part of this work, high purity samples of CaB_6 and SrB_6 were synthesized from the elements. The synthesis was optimized by using freshly distilled alkaline earth metals as starting materials. Identity was established by XRD. According to ICP-OES measurements the concentrations of impurities (except for Ba and Ca or Sr, respectively) are reduced to 0.1 - 0.01 weight percent, which is confirmed by EDX and EELS. The boron K-edge fine structure as detected in EELS measurements was found to be characteristic of an octahedral boron framework, and can be used to characterize other compounds with similar boron structure units. From XANES spectroscopy the oxidation state of the alkaline earth metals was found to be +2 in CaB_6 and SrB_6. TGA measurements in different atmospheres revealed the uptake of oxygen at elevated temperatures. Oxidation starts at 670 °C independently from the percentage of oxygen.

For conductivity measurements, an instrument was constructed and built. Conductivity above RT was characterized using the low-frequence AC four-probe method. In addition, for the first synthesized samples of CaB_6 and SrB_6 the collinear DC four probe method was applied below RT. All samples showed semiconducting behaviour. For SrB_6, the band gap normally increases with decreasing dopant concentration. The only element to have a positive effect on the value of the band gap was found to be Ba. The highest measured value for one of the purest samples of SrB_6 was 0.13 eV. For ideal SrB_6, the band gap was extrapolated, using multi-linear regression, to be about 0.073 eV.

In the second part, nanoscale iron borides were synthesized and characterized.

Using different methods of synthesis, the following kinds of particles were obtained:

- agglomerated iron borides sized from 20 to 150 nm with free active surfaces for catalytic experiments, were synthesized via chemical reduction of Fe^{2+} with $NaBH_4$ in aqueous solutions.

- amorphous separate nanoparticles of iron borides ranging in size from 5 to 20 nm, for magnetic applications, were synthesized via chemical reduction of Fe^{2+} with $NaBH_4$ which takes place in reverse micelles, small water droplets which are dispersed in isooctane and stabilized with a layer of a surfactant consisting of molecules which are hydrophilic at one end and hydrophobic at the other.

- crystalline separate nanoparticles of iron borides from 3 to 12 nm in size, for magnetic applications, were synthesized via chemical reduction of Fe^{2+} with $NaBH_4$ in hot (257-290 °C) non-polar solvent containing the surface agents (stabilizers).

The form, size, crystallinity, oxidation state and chemical composition were characterized via ICP-OES, XAS, EDX, EELS, XPS, SEM and TEM.

All boride nanoparticles were found to be air-sensitive; in the case of separate nanoparticles the oxidation is slower because of a protecting shell of organic ligands.

The magnetic properties of crystalline nanoparticles of different sizes, which had either oxidized or not, were investigated. They were found to be either super-paramagnetic or ferromagnetic depending on the size. The non-oxidized particles (iron borides) look much more promising because their blocking temperature (between 90 and 300 K) and magnetic moment (about 40 emu/g) are higher than for oxidized samples like iron borates (between 50 and 90 K and 4 emu/g). The blocking temperature of synthesized samples is also higher than that of normally used iron oxides or iron nanoparticles (17 K [100] and 70 K [119], respectively).

This makes them very useful for applications in magnetic storage systems at temperatures higher than that of iron oxide or iron nanoparticles, but because of their air sensitivity a technology has to be developed to provide them with an air-protective coating (e.g. with polymers).

The oxidized particles, which are super-paramagnetic at room temperature, could be used in medicine where super-paramagnetism is more important than ferromagnetism.

5 References

[1] N. N. Greenwood, A. Earnshaw, *Chemie der Elemente*, VCH Weinheim*, (**1988**)

[2] R. Telle, *Chemie in unserer Zeit*, 3, 94, (**1988**)

[3] K. Schmitt, Dissertation, University of Gießen, (**2000**)

[4] M. Pompetzki, Dissertation, University of Bonn, (**2003**)

[5] R. Pöttgen, T. Gulden, et al., *GIT Labor-Fachzeitschrift*, 43, 2, 133, (**1999**)

[6] R. Pöttgen, H. Borrmann, et al., *J. Alloys. Compd.*, 235, 170, (**1996**)

[7] R. Pöttgen, *Z. Naturforsch.*, 49, B, 1309, (**1994**)

[8] T. H. Gulden, R. W. Henn, et al., *Phys. Rev. B*, 56, 9021, (**1997**)

[9] A. R. West, *Solid State Chemistry and its Applications*, John Wiley & Sons, (**1984**)

[10] R. J. Hill, I. C. Madsen, *J. Appl. Cryst.*, 17, 297, (**1984**)

[11] W. Bronger, *Röntgenographische Untersuchungen nach der Pulvermethode*, Aachen, (**1985**)

[12] Huber: *Diffraktometer Guinier System 600*, Benutzerhandbuch

[13] A. R. West, *Basic Solid State Chemistry*, John Wiley & Sons, (**1999**)

[14] M. S. Adam, Dissertation, University of Hamburg, (**2004**)

[15] F. Settle, *Handbook of Instrumental Techniques for Analytical Chemistry*, Prentice Hall PTR, (**1997**)

[16] A. Kodre, I. Arcon, et al., *Acta. Chim. Slov*. 51, 1, (**2004**)

[17] M. Croft, D Sills, et al., *Phys. Rev. B*, 55, 14, 8726, (**1997**)

[18] O. Leynaud, M. T. Caldes, *Chem. Mater. B*, 1, (**2003**)

[19] M. Wilke, *American Mineralogist*, 86, 714, (**2001**)

[20] P. Behrens, *Trends in anal. chem.*, 11, 7, 237, (**1992**)

[21] B.K. Teo, *EXAFS : Basic Principles and Data Analysis*, Inorganic Chemistry Concepts Vol 9., Springer-Verlag, (**1986**)

[22] O. Wilkin, *J. Chem. Soc.*, Dalton Trans., 2405, (**1999**)

[23] R. F. Egerton, *Electron Energy-Loss Spectroscopy in the Electron Microscope*, Plenum Press New York, (**1996**)

[24] Gatan: *Modell 666 Parallel Detection Electron Spectrometer-Instruction Manual*, (**1988**)

[25] D. B. Williams, C. B. Carter, *Transmission electron microscopy: a textbook for material science*, 4 Plenum Press New York, (**1996**)

[26] P. R. Buseck, *Minerals and Reactions at the atomic scale: Transmission Electron Microscopy*, Reviews in Mineralogy, Mineralogical Society of America, Vol. 27, (**1994**)

[27] J. Joubert, T. Shirk, *Mat. Res. Bull.*, 3, 671, (**1968**)

[28] I. Avaeva, V. Kravchenko, *Izvestija Akad. Nauk SSSR*, 8, N 7, 1330, (**1972**)

[29] D.Maniu, T. Iliescu, et al., *Studia Universitatis Babes-Bolyai, Physica*, Special Issue, (**2001**)

[30] H. L. Tuller, P. K. Moon, *Mat. Sci. Eng. B*, 1, 171, (**1988**)

[31] G. Schmid, *Nanoparticles: From Theory to Application*, Willey-VCH Verlag, 199, (**2004**)

[32] C. M. Sorensen, K. J. Klabunde, *Nanoscale Materials in Chemistry*, John Wiley, 162, (**2001**)

[33] C. B. Murray, S. Sun, et al., *MRS Bullletin*, 985, (**2001**)

[34] D. L. Leslie-Pelecky, R. D. Rieke, *Chem. Mater.*, 8, 1770, (**1996**)

[35] H. Moissan, P. Williams, *Compt. Rend.*, 125, 629, (**1897**)

[36] C. Geelmuyden, *Compt. Rend.*, 130, 1026, (**1900**)

[37] E. Juengst, R. Mewes, *Chem. Ztrblt.*, 1, 195, (**1905**)

[38] A. Stock, W. Holle, *Ber. Dtsch. Chem. Ges.*, 41, 2095, (**1908**)

[39] L. Andrieux, *Compt. Rend.*, 182, 126, (**1926**)

[40] G. Allard, *Compt. Rend.*, 189, 108, (**1929**)

[41] M. von Stackelberg, F. Neumann, *Z. Physik. Chem. B*, 19, 314, (**1932**)

[42] L. Pauling, S. Weinbaum, *Z. Kristallogr.*, 87, 181, (**1934**)

[43] S. Muranaka, S. Kawai, *J. Crystal Growth*, 26, 165, (**1974**)

[44] T. Ito, I. Higashi, *JJAP Series*, 10, 11, (**1994**)

[45] S. Otani, *J. Crystal. Growth*, 192, 346, (**1998**)

[46] H. R. Ott, M. Chernikov, et al. *Z. Phys. B*, 102, 337, (**1997**)

[47] A. V. Blinder, S. P. Gordienko, et al., *Powder Met. and Met. Ceram.*, 36, 409, (**1997**)

[48] G. G. Tsebulya, G. K. Kozina, et al., *Powder Met. and Met. Ceram.*, 36, 413, (**1997**)

[49] H. C. Longuet-Higgins, M. de V. Roberts, *Proc. R. Soc. London Ser. A*, 224, 336, (**1954**)

[50] P. G. Perkins, D. R. Armstrong, et al., *J. Phys. C : Solid State Phys.*, 8, 3558, (**1975**)

[51] A. Hasegawa, A. Yanasa, *J. Phys. C*, 12, 5431, (**1979**)

[52] S. Massidda, A. Continenza, et al., *Z. Phys. B*, 102, 83, (**1997**)

[53] R. Naslain, J. Etourneau, et al., *Alkali Metal Borides, in Boron and Refractory Borides*, V. I. Matkovich (Hrsg.) Springer, (**1977**)

[54] M. C. Nichols, R. W. Mar, *J. Less-Common Met.*, 33, 317, (**1973**)

[55] D. P. Young, et al., *Nature*, 397, 412, (**1999**)

[56] P. G. Perkins, *The electronic structure of the hexaborides and the diborides*, *in Boron and Refractory Borides*, V. I. Matkovich (Hrsg.) Springer, (**1977**)

[57] R. W. Johnson, A. H. Daane, *J. Chem. Phys*, 38, 425, (**1963**)

[58] D. P. Young, et al., *Phys. Rev. B*, 62, 10076, (**2000**)

[59] K. Matsubayashi, et al., *Nature*, 420, 143, (**2002**)

[60] J. Rhyee, B. H. Oh, et al., *Cond. Matter*, 15, 6285, (**2003**)

[61] J. D. Denlinger, J. A. Crack, *Phys. Rev. Lett.*, 89, 15, 157601, (**2002**)

[62] K. Schmitt, B. Albert, et al., *Solid State Sci.*, 3, 321, (**2001**)

[63] J. Matsushita, K. Mori, et al., *J. Mat. Synth. Proc.*, 6, 6, 407, (**1998**)

[64] K. Hofmann, B. Albert, et al., *Z. Anorg. Allg. Chem.*, 628, 12, 2691, (**2002**)

[65] K. Hofmann, B. Albert, *Chem. Phys. Chem.*, 3, 10, 896, (**2002**)

[66] L. Wang, Z. C. Tan, *J. Therm. Analysis & Calorimetry*, Vol. 66, 409, (**2001**)

[67] G. N. Glavee, K. J. Klabunde, *Langmuir*, 8, 771, (**1992**)

[68] G. N. Glavee, K. J. Klabunde, *Langmuir*, 9, 162, (**1993**)

[69] V. G. Harris, S. A. Oliver, *Appl. Phys. Lett.*, 68, 15, 2073, (**1996**)

[70] T. Ressler, S. L. Brock, *J. Phys. Chem. B*, 103, 6407, (**1999**)

[71] G. N. Glavee, K. J. Klabunde, *Inorg. Chem.*, 34, 28, (**1995**)

[72] V. I. Matkovich (Ed.), *Boron and Refractory Borides*, Springer, (**1977**)

[73] T. Bjurström, H. Arnfelt, *Z. Phys. Chem. B*, 4, 469, (**1929**)

[74] D. J. Joyner, O. Johnson, *Phys. Rev. B: Cond. Mat. & Mat. Phys.*, 24, 6, 3122, (**1981**)

[75] L. Fashen, X. Desheng, et al., *Hyperfine Interactions*, 69, 651, (**1992**)

[76] S. Linderoth, S. Moerup, et al., *J. of Magn. & Magn. Mat.*, 81, 138, (**1989**)

[77] F. Schmueckle, P. Lamparter, et al., *Zeitschrift fuer Naturforschung*, 37, A, 6, 572, (**1982**)

[78] J. Budnick, F. Sanchez, *IEEE Transactions on Magnetics*, MAG-23, 4, 1937, (**1987**)

[79] J. Nagy, *Colloids and Surfaces*, 35, 201, (**1989**)

[80] J. Chen, C. Sorensen, et al., *Applied Sciences*, 260, 613, (**1994**)

[81] J. Chen, C. Sorensen, et al., *Physical Review B: Condensed Matter*, 51, 17, 11527, (**1995**)

[82] M. Pileni, *J. Phys. Chem.*, 97, 27, 6961, (**1993**)

[83] J. Tanori, N. Duxin, et al., *Colloid and Polymer Science*, 273, 9, 886, (**1995**)

[84] C. Petit, M. Pileni, et al., *J. Magn. & Magn. Materials*, 166, 82, (**1997**)

[85] J. Legrand, A. Taleb, et al., *Langmuir*, 18, 10, 4131, (**2002**)

[86] Y. Khan, H. Wibbeke, *Z. Metallkd.*, 82, 703, (**1991**)

[87] H. Gleiter, *Adv. Mater.*, 4, 474, (**1992**)

[88] R. L. Whetten, M. N. Shafigullin, et al., *Acc. Chem. Res.*, 32, 5, 397, (**1999**)

[89] Y. Shengwen, W. Guanghou, et al., *Phys. Lett. A*, 268, 442, (**2000**)

[90] Y. Zhou, Z. Zhang, et al., *Materials Letters*, 59, 27, 3375, (**2005**)

[91] J. Balogh, L. Bujdoso, et al., *J. Phys.: Condens. Matter*, 9, L, 503, (**1997**)

[92] J. Balogh, Z. Horvath, et al., *Phys. Rev.*, 1, 57, 29, (**1998**)

[93] C. Murray, D. Norris, et al., *J. Am. Chem. Soc.*, 115, 8706, (**1993**)

[94] C. Murray, C. Kagan, et al., *Annu. Rev. Mater. Sci.*, 30, 545, (**2000**)

[95] C. Murray, S. Shouheng, et al., *IBM. J. Res. & Dev.*, 45, 1, 1, (**2001**)

[96] E. U. Muellerwiebus, K. A. Hempel, *Phys. B: Phys. of Condensed Matter*, 86, Pt. 3, 1261, (**1977**)

[97] C. Voigt, *Physics Letters A*, 53, A, 3, 223, (**1975**)

[98] C. Voigt, D. Bonnenberg, *Phys. B: Phys. of Condensed Matter*, 80, 439, (**1975**)

[99] A. Latham, R. Freitas, et al., *Anal. Chem.*, 77, 5055, (**2005**)

[100] L. Wang, J. Luo, et al., *J. Phys. Chem. B.*, 109, 21593, (**2005**)

[101] T. Ito, T. Kasukawa, et al., *JJAP Ser.*, 10, 11, (**1994**)

[102] C. Kapfenberger, B. Allbert, et al., *Z. Kristallogr.* 221, 477, (**2006**)

[103] M. Cadeville, E. Daniel, *J. Phys.*, 27, 449, (**1966**)

[104] C. L. Chien, *Phys. Rev. B*, 18, 1003, (**1978**)

[105] R. Fruchart, A. Michel, *Mem. Soc. Chim.*, 11, 422, (**1959**)

[106] C. L. Chien, D. Musser, *Phys. Rev. B*, 20, 283, (**1979**)

[107] J. L. Walter, S. F. Bartram, et al., *Mat. Trans.*, A, 9, 803, (**1978**)

[108] C. L. Chien, K. M. Unruh, *Phys. Rev. B*, 24, 1556, (**1981**)

[109] T. Kemeny, I. Vincze, et al., *Phys. Rev. B*, 20, 476, (**1979**)

[110] C. L. Chien, K. M. Unruh, *Phys. Rev. B*, 25, 9, 5790, (**1982**)

[111] M. L. Fdez-Gubieda, A. Garcia-Arribas, et al., *Phys. Rev.* B, 62, 9, 5746, (**2000**)

[112] J. van Worterghem, S. Morup, et al., *Nature*, 322, 622, (**1986**)

[113] D. Buchkow, S. Nikolov, et al., *J. Magn. Magn. Mater.*, 62, 87, (**1986**)

[114] I. Dragieva, M. Slavcheva, et al., *J. Less-Common Met.*, 117, 311, (**1986**)

[115] S. Morup, J. van Worterghem, et al., *IEEE. Trans. Magn.*, MAG-23, 2978, (**1987**)

[116] S. Wells, S. W. Charles, et al., *J. Phys.: Condens. Matter.*, 1, 8199, (**1989**)

[117] M. X. Mao, F. S. Li, et al., *J. Appl. Phys.*, 73, 10, 6983, (**1993**)

[118] A. Corrias, G. Ennas, et al., *Chem. Mater.*, 5, 1722, (**1993**)

[119] P. Poddar, J. L. Wilson, et al., *Phys. Rev. B*, 68, 214409, (**2003**)

[120] G. Kataby, A. Ulman, et al., *Langmuir*, 14, 1512, (**1998**)

[121] V. Kravchuk, A. Lazebnik, et al., *Russ. J. Inorg. Chem.*, 12, 21, (**1967**)

[122] C. Petit, P. Lixon, et al., *Langmuir*, 7, 2620, (**1991**)

[123] L. Guo, Q. Huang, et al., *Phys. Chem. Chem. Phys.*, 3, 1661, (**2001**)

[124] N. Gaponik, D. Talapin, et al., *J. Phys. Chem.*, B, 106, 7177, (**2002**)

[125] S. B. Hendricks, P. R. Kosting, *Z. Krystallogr. Krystallgeom.*, 74, 511, (**1930**)

[126] T. Bjurström, *Ark. Kemi, Min. Geol.*, 11, 1, (**1933**)

[127] U. Herold, *Z. Metallkd.*, 69, 326, (**1978**)

[128] F. Farges, *Amer. Miner.*, 82, 36, (**1997**)

[129] B. Lengeler, P. Eisenberger, *Amer. Miner.*, 21, 10, 4507, (**1980**)

[130] Z. Qin, W. Wang, et al., *Acta Phys. Sinica*, 36, 769, (**1987**)

[131] B. Callmer, T. Lundstroem, *J. Solid State Chem.*, 17, 165, (**1976**)

[132] F. Wever, A. Mueller, *Z. Anorg. Allg. Chem.*, 192, 317, (**1930**)

[133] D. J. Joyner, O. Johnson, et al., *J. Amer. Chem. Soc.*, 102, 6, 1910, (**1980**)

[134] T. Ressler, *WinXAS 3.10*, (**2004**)

[135] B. Ravel, *ATOMS 2.46b*, Univ. of Washington (**1994**)

[136] B. Ravel, *FEFF 7.02*, Univ. of Washington (**1994**)

[137] K. V. Klementiev, *XAFS mass*, HASYLAB (**2003**)

[138] F. E. Luborsky, *Appl. Phys. Lett.*, 33, 233, (**1978**)

[139] G. J. Fan, M. X. Quan, et al., *Appl. Phys. Lett.*, 68, 3, 319, (**1996**)

[140] P. Vavassori, F. Ronconi, et al., *J. Appl. Phys.*, 82, 12, 6177, (**1997**)

[141] H. Bunzel, E. Kreber, et al., *J. de Phys.*, 6, 609, (**1974**)

[142] E. P. Wohlfarth, *J. Magn. Magn. Mater.*, 7, 113, (**1978**)

[143] Y. Kong, F. Li, *Phys. Rev.*, 56, 3153, (**1997**)

[144] C. L. Chien, K. M. Unruh, *Phys. Rev. B*, 25, 9, 5790, (**1984**)

[145] B. T. M. Willis, H. P. Rooksby, *Acta. Crystallogr.*, 6, 827, (**1953**)

[146] ICSD 3-186, *Dow chemical company*, Midland Michigan, USA, private communication

[147] R. Diehl, G. Brandt, *Acta Cryst., Sec. B*, 31, 1662, (**1975**)

[148] H. E. Swanson, et al., *Natl. Bur. Stand.*, 539, IV, 3, (**1955**)

[149] N. A. Yamnova, M. A. Simonov, et al., *Kristallografiya*, 20, 156, (**1975**)

[150] J. S. Swinnea, H. Steinfink, *Am. Mineral.*, 68, 827, (**1983**)

[151] L. Walter-Levy, E. Quemeneur, *Bull. Soc. Chim.*, 22, 495, (**1968**)

[152] S. V. Berger, *Acta Chem. Scand.*, 7, 611, (**1953**)

[153] C. Greaves, *Solid State Chem.*, 49, 325, (**1983**)

6 Safety precaution information on the used chemicals

Substance	R-phrases	S-phrases	Hazard signs
acetone	11-36-66-67	9-16-26	[F] [Xi]
boron	11-22	16	[F] [Xn]
calcium	15	8-24/25-43	[F]
CaB_6	-	-	[A]
$CaBr_2$	38	-	[Xi]
CaC_2	15	8-43	[F]
$CaCl_2 \cdot 6H_2O$	36	-	[Xi]
$CaCO_3$	36/37/38	-	[Xi]
CaF_2	20/21	-	[Xn]
chloroform	22-38-40-48/20-22	36/37	[Xn]
diphenylether	36/37/38-51/53	-	[Xi] [N]
dioctylether	-	-	[A]
ethanol	11-20/21/22-68/20/21/22	16-36/37	[F] [Xn]
$Fe(acac)_2$	22-36/37/38	-	[Xn]
$Fe(AOT)_2$	Not fully examined compound		
FeB	-	-	[A]
Fe_2B	-	-	[A]
$Fe_6B_{14}O_{27} \cdot H_2O$	Not fully examined compound		
$Fe(BO_2)_2$	Not fully examined compound		
$FeBO_3$	Not fully examined compound		
Fe_3BO_6	Not fully examined compound		
$FeCl_2$	36/38	-	[Xi]
$FeCl_2 \cdot 4H_2O$	22-36/37/38	-	[Xn]
$FeCl_3$	22-34-36/38	-	[Xn] [C]
FeO	-	-	[A]
Fe_2O_3	-	-	[A]
Fe_3O_4	-	-	[A]
$FeSO_4 \cdot 7H_2O$	22	-	[Xn]
hexadecylamine	36/37/38	-	[Xi]
1,2-hexandiole	36/37/38	-	[Xi]
hydrochloric acid	34-37	26-36/37/39-45	[C]
iron	11	-	[F]

isooctane	11-38-50/53-65-67	9-16-29-33-60-61-62	[F] [N] [Xn]
lithiumborhydrid	11-15-19-34	-	[F] [C]
methanol	11-23/24/25-39/23/24/25	7-16-36/37-45	[F] [T]
natriumborhydrid	15-24/25-26-34	22-26-36/37/39-43.13-45	[F] [T+]
NaAOT	22-36/38	-	[Xn]
oleic acid	-	-	[A]
oleylamine	22-34	-	[Xn] [C]
polyethylene	-	22	-
SrB_6	-	-	[A]
$SrBr_2$	-	-	[A]
$SrCl_2 \cdot 6H_2O$	-	-	[A]
strontium	15	-	[F]
sulphuric acid	35	26-30-45	[C]
tetrahydrofuran	11-19-36/37	16-29-33	[F] [Xi]
trioctylphosphine	36/38	-	[Xi]
trioctylphosphine oxide	34-50/53	26-36/37/39-45-60-61	[C] [N]
toluene	11-38-48/20-63-65-67	36/37-46-62	[F] [Xn]

Risk (R-) and safety precaution (S-) phrases used in the classification, packaging, labelling and provision of information on dangerous substances

Risk phrases (R-Phrases)
R1: Explosive when dry
R2: Risk of explosion by shock, friction fire or other sources of ignition
R3: Extreme risk of explosion by shock friction, fire or other sources of ignition
R4: Forms very sensitive explosive metallic compounds
R5: Heating may cause an explosion
R6: Explosive with or without contact with air
R7: May cause fire
R8: Contact with combustible material may cause fire
R9: Explosive when mixed with combustible material
R10: Flammable
R11: Highly flammable
R12 : Extremely flammable
R13: Extremely flammable liquefied gas
R14: Reacts violently with water
R15: Contact with water liberates highly flammable gases
R16: Explosive when mixed with oxidising substances
R17: Spontaneously flammable in air
R18: In use, may form flammable/explosive vapour-air mixture
R19: May form explosive peroxides
R20: Harmful by inhalation

R21: Harmful in contact with skin
R22: Harmful if swallowed
R23: Toxic by inhalation
R24: Toxic in contact with skin
R25: Toxic if swallowed
R26: Very toxic by inhalation
R27: Very toxic in contact with skin
R28: Very toxic if swallowed
R29: Contact with water liberates toxic gas
R30: Can become highly flammable in use
R31: Contact with acids liberates toxic gas
R32: Contact with acids liberates very toxic gas
R33: Danger of cumulative effects
R34: Causes burns
R35: Causes severe burns
R36: Irritating to eyes
R37: Irritating to respiratory system
R38: Irritating to skin
R39: Danger of very serious irreversible effects
R40: Possible risk of irreversible effects
R41: Risk of serious damage to eyes
R42: May cause sensitisation by inhalation
R43: May cause sensitisation by skin contact
R44: Risk of explosion if heated under confinement
R45: May cause cancer
R46: May cause heritable genetic damage
R47: May cause birth defects
R48: Danger of serious damage to health by prolonged exposure
R49: May cause cancer by inhalation
R50: Very toxic to aquatic organisms
R51: Toxic to aquatic organisms
R52: Harmful to aquatic organisms
R53: May cause long-term adverse effects in the aquatic environment
R54: Toxic to flora
R55: Toxic to fauna
R56: Toxic to soil organisms
R57: Toxic to bees
R58: May cause long-term adverse effects in the environment
R59: Dangerous to the ozone layer
R60: May impair fertility
R61: May cause harm to the unborn child
R62: Possible risk of impaired fertility
R63: Possible risk of harm to the unborn child
R64: May cause harm to breastfed babies

Combination of risks
R14/15: Reacts violently with water, liberating highly flammable gases
R15/29: Contact with water liberates toxic, highly flammable gas
R20/21: Harmful by inhalation and in contact with skin
R20/21/22: Harmful by inhalation, in contact with skin and if swallowed
R20/22: Harmful by inhalation and if swallowed

R21/22: Harmful in contact with skin and if swallowed
R23/24: Toxic by inhalation and in contact with skin
R23/24/25: Toxic by inhalation, in contact with skin and if swallowed
R23/25: Toxic by inhalation and if swallowed
R24/25: Toxic in contact with skin and if swallowed
R26/27: Very toxic by inhalation and in contact with skin
R26/27/28: Very toxic by inhalation, in contact with skin and if swallowed
R26/28: Very toxic by inhalation and if swallowed
R27/28: Very toxic in contact with skin and if swallowed
R36/37: Irritating to eyes and respiratory system
R36/37138: Irritating to eyes, respiratory system and skin
R36/38: Irritating to eyes and skin
R37/38: Irritating to respiratory system and skin
R42/43: May cause sensitisation by inhalation and skin contact.
R48/20: Harmful: danger of serious damage to health by prolonged exposure
R48/20/21: Harmful: danger of serious damage to health by prolonged exposure through inhalation and in contact with the skin
R48/20/21/22: Harmful: danger of serious damage to health by prolonged exposure through inhalation, in contact with skin and if swallowed
R48/20/22: Harmful: danger of serious damage to health by prolonged exposure through inhalation, and if swallowed
R48/21: Harmful: danger of serious damage to health by prolonged exposure in contact with skin
R48/21/22: Harmful: danger of serious damage to health by prolonged exposure in contact with skin and if swallowed
R48/22: Harmful: danger of serious damage to health by prolonged exposure if swallowed
R48/23: Toxic: danger of serious damage to health by prolonged exposure through inhalation
R48/23/24: Toxic: danger of serious damage to health by prolonged exposure through inhalation and in contact with skin
R48/23/24/25: Toxic: danger of serious damage to health by prolonged exposure through inhalation, in contact with skin and if swallowed
R48/23/25: Toxic: danger of serious damage to health by prolonged exposure through inhalation and if swallowed
R48/24: Toxic: danger of serious damage to health by prolonged exposure in contact with skin
R48/24/25: Toxic: danger of serious damage to health by prolonged exposure in contact with skin and if swallowed
R48/25: Toxic: danger of serious damage to health by prolonged exposure if swallowed
R50/53: Very toxic to aquatic organisms, may cause long term adverse effects in the aquatic environment
R51/53: Toxic to aquatic organisms, may cause long term adverse effects in the aquatic environment
R52/53: Harmful to aquatic organisms, may cause long-term adverse effects in the aquatic environment

Safety precaution phrases (S-Phrases)
S1: Keep locked up
S2: Keep out of reach of children
S3: Keep in a cool place
S4: Keep away from living quarters
S5: Keep contents under . . . (appropriate liquid to be specified by the manufacturer)

S6: Keep under . . . (inert gas to be specified by the manufacturer)
S7: Keep container tightly closed
S8: Keep container dry
S9: Keep container in a well ventilated place
S12: Do not keep the container sealed
S13: Keep away from food, drink and animal feeding stuffs
S14: Keep away from . . . (incompatible materials to be indicated by the manufacturer)
S15: Keep away from heat
S16: Keep away from sources of ignition-No Smoking
S17: Keep away from combustible material
S18: Handle and open container with care
S20: When using do not eat or drink
S21: When using do not smoke
S22: Do not breathe dust
S23: Do not breathe gas/fumes/vapour/spray (appropriate wording to be specified by manufacturer)
S24: Avoid contact with skin
S25: Avoid contact with eyes
S26: In case of contact with eyes, rinse immediately with plenty of water and seek medical advice
S27: Take off immediately all contaminated clothing
S28: After contact with skin, wash immediately with plenty of . . (to be specified by the manufacturer)
S29: Do not empty into drains
S30: Never add water to this product
S33: Take precautionary measures against static discharges
S34: Avoid shock and friction
S35: This material and its container must be disposed of in a safe way
S36: Wear suitable protective clothing
S37: Wear suitable gloves
S38: In case of insufficient ventilation, wear suitable respiratory equipment
S39: Wear eye/face protection
S40: To clean the floor and all objects contaminated by this material use (to be specified by the manufacturer)
S41: In case of fire and/or explosion do not breath fumes
S42: During fumigation/spraying wear suitable respiratory equipment (appropriate wording to be
specified by the manufacturer)
S43: In case of fire, use ... (indicate in the space the precise type of fire fighting equipment. If water
increases the risk, add "never use water")
S44: If you feel unwell, seek medical advice (show the label where possible)
S45: In case of accident or if you feel unwell, seek medical advice immediately (show the label where possible)
S46: If swallowed, seek medical advice immediately and show the container or label
S47: Keep at temperature not exceeding ... °C (to be specified by the manufacturer)
S48: Keep wetted with ... (appropriate material to be specified by the manufacturer)
S49: Keep only in the original container
S50: Do not mix with ... (to be specified by the manufacturer)
S51: Use only in well ventilated areas
S52: Not recommended for interior use on large surface areas

S53: Avoid exposure - obtain special instructions before use
S54: Obtain the consent of pollution control authorities before discharging to waste-water treatment plants
S55: Treat using the best available techniques before discharge into drains or the aquatic environment
S56: Do not discharge into drains or the environment, disposwe to an authorised waste collection point
S57: Use appropriate containment to avoid environmental contamination
S58: To be disposed of as hazardous waste
S59: Refer to manufacturer/supplier for information on recovery/recycling
S60: This material and/or its container must be disposed of as hazardous waste
S61: Avoid release to the environment. Refer to special instructions / safety data sheet
S62: If swallowed, do not induce vomiting: seek medical advice immediately and show the containeror label

Combined safety phrases
S1/2: Keep locked up and out of reach of children
S3/9: Keep in a cool, well ventilated place
S3/7/9: Keep container tightly closed in a cool, well ventilated place
S3/14: Keep in a cool place away from ... (incompatible materials to be indicated by the manufacturer)
S3/9/14: Keep in a cool, well ventilated place away from ... (incompatible materials to be indicated by the manufacturer)
S3/9/49: Keep only in the original container in a cool, well ventilated place
S3/9/14/49: Keep only in the original container in a cool, well ventilated place away from (incompatible materials to be indicated by the manufacturer)
S3/9/49: Keep only in the original container in a cool, well ventilated place
S3/14: Keep in a cool place away from...(incompatible materials to be indicated by the manufacturer)
S7/8: Keep container tightly closed and dry
S7/9: Keep container tightly closed and in a well ventilated place
S7/47: Keep container tightly closed and at a temperature not exceeding...°C (to be specified by manufacturer
S20/21: When using do not eat, drink or smoke
S24/25: Avoid contact with skin and eyes
S29/56: Do not empty into drains, dispose of this material and its container to hazardous or special waste collection point
S36/37: Wear suitable protective clothing and gloves
S36/37/39: Wear suitable protective clothing, gloves and eye/face protection
S36/39: Wear suitable protective clothing, and eye/face protection
S37/39: Wear suitable gloves and eye/face protection
S47/49: Keep only in the original container at temperature not exceeding...°C (to be specified by the manufacturer)

DENIS FOFANOV

E-Mail: fofanov@chemie.uni-hamburg.de

Geburtsdatum/Ort: 02 Juni 1976, Voloma, Russland

Familienstand: ledig

Nationalität   Russische Föderation

Studium und Doktorarbeit

2002-2006	Universität Hamburg, Institut für anorganische und angewandte Chemie, Arbeitsgruppe von Prof. Albert **Dr**. rer. nat. voraussichtlich Juli 2006

„Synthese und Charakterisierung von nanoskaligen Eisenboriden"
- Synthese von Nanopartikeln in koordinierenden Lösungsmittel
- Untersuchung der magnetischen Eigenschaften

„Synthese und Untersuchung der elektronischen Eigenschaften von Erdalkalimetallboriden"
- Hochtemperatursynthese unter Inertbedingungen
- Entwicklung und Aufbau der Leitfähigkeitmessanlage, Service- und Forschungsmessungen

1995-2001   Polytechnische Universität St.-Petersburg, Russland, „Physik der Metallen" und „Computertechnologien in der Materialwissenschaft"

Magister der Naturwissenschaften in Physik der Metalle, 2001

„Experimentelle Optimierung der thermo-mechanischen Bearbeitung von Konstruktionsstahl"
- Nachbildung von industriellen Bedingungen thermo-mechanischer Stahlbearbeitung
- Analyse der Zusammenhänge zwischen Körnerstrukturen und mechanischen Eigenschaften
- Optimierung des Produktionsprozesses

Bachelor der Naturwissenschaften in technischer Physik, 1999

„Modellierung plastischer Metalldeformation"
- Computermodellierung der Textur, die durch plastische Deformation verursacht wurde

Berufstätigkeit

2002-2006	Universität Hamburg, Institut für anorganische und angewandte Chemie, Arbeitsgruppe von Prof. Albert **Wissenschaftlicher Mitarbeiter** *„Design und Charakterisierung funktionalisierter Materialien"* (DFG, in Kooperation mit sieben anderen Instituten) - Nanoskalierung, Modifizierung und Funktionalisierung von Oberflächen und Teilchen, um die besonderen elektrischen, magnetischen und katalytischen Eigenschaften zu bestimmen
2000-2002	GAG „METTEK" St.-Petersburg, Russland **Leiter der wissenschaftlich-technischen Gruppe**, August 2001-September 2002 *„Analyse von Uranisotopen"*, *„Gasanalyse in Erdölindustrie"* Mitglied der wissenschaftlich-technischen Gruppe, 2000 *„Gasanalyse in Metallurgie"*, *„Gasanalyse in Erdölindustrie"*
1999-2000	GAG „Ceylon", Bratsk, Russland Kaufmanager (Teilzeit)
1998-1999	GAG „Special materials" St.-Petersburg, Russland **Praktikum**, November 1998-Februar 1999 „Schutzausrüstung für Polizei und Armee" - Computergestütztes Design, Entwicklung von neuen Modellen

Referenten

Professor Dr. Barbara Albert	Tel.: 06151/162392 Fax: 06151/166029 E-Mail: albert@ac.chemie.tu-darmstadt.de
Professor Dr. Jürgen Kopf	Tel: 040 / 42838 - 2897, Fax: 040 / 42838 - 6348 E-Mail: kopf@xray.chemie.uni-hamburg.de

Publications:

1) D. N. Fofanov, N. J. Zolotarevskij, "Physical models of the plastic deformation in polycrystals.", Materials of student's scientific conference. XXVII week of science in St.-Petersburg State Technical University, -St.-Petersburg, 1999. -vol.3, pp.26 (in Russian)

2) G. E. Kodjaspirov, V. F. Bogomolov, M. A. Gordov, D. N. Fofanov, "Structure and mechanical properties HTMP treated ST52.3 steel.", International Scientific and Engineering Conference "High technologies in advanced metal science and engineering», - St.-Petersburg, 2001. -p.112-116 (in Russian)

3) D. N. Fofanov, A. G. Ershov, A. O. Piskunov, "Methods of gas analysis for hydrocarbons determination.", Russian Scientific and Practical Conference "Students to hi-tech entrepreneurship", September 4-6th, 2001, - Kazan, 2001. -pp.115-116 (in Russian)

4) D. N. Fofanov, A. G. Ershov, A. O. Piskunov, "Development of calibration method of gas-analyzer for analysis of hydrocarbons mixture.", Book of students scientific and technical reports "Students to hi-tech entrepreneurship", 2000-2001, -St.-Petersburg, 2001. – pp. 163-170 (in Russian)

5) D. Fofanov, E. Welter and B. Albert, "XAS Identification of Nanoparticles of Iron, Iron borides, and Iron borates", *http://www-hasylab.desy.de/science/annual_reports/2004_report/part1/*

6) D. Fofanov, B. Albert, Participated Norddeutsches Doktoranden Kolloquium, held at Hamburg, Germany, Sep 25-26, 2003. Poster titled: "Investigation of the conductivity of CaB_6 microcrystallites".

7) D. Fofanov, B. Albert, Participated Norddeutsches Doktoranden Kolloquium, held at Hamburg, Germany, Sep 30- Oct 01, 2004. Talk titled: "Synthesis and Characterization of iron boride nanoparticles".

8) D. Fofanov, B. Albert, Participated in the Interdisciplinary Graduate School 611-Design and Characterization of Functional Materials held at Hamburg, Germany, Jan 18, 2005 Poster titled: "Iron boride particles of different length scales".

9) D. Fofanov, M. Bauer, B. Albert, J. A. C. Broekaert, Participated in the Interdisciplinary Graduate School 611- Design and Characterization of Functional Materials held at Hamburg, Germany, Jan 18, 2005 Poster titled: "Conductivity measurements for boron-rich compaunds".

10) M. Bauer, D. Fofanov, B. Albert, J. A. C. Broekaert, Participated in the Interdisciplinary Graduate School 611- Design and Characterization of Functional Materials held at Hamburg, Germany, Jan 18, 2005 Poster titled: "Investigations on the improvement of precision and accuracy in ICP-OES for the analysis of advanced refractory materials".

11) D. Fofanov, B. Albert, Participated 15th International Symposium Boron, Borides and Related Compounds, held at Hamburg, Germany, Aug 21-26, 2005 Talk titled: " Synthesis and Characterization of iron boride nanoparticles".

12) D. Fofanov, M. Bauer, B. Albert, J. A. C. Broekaert, Participated 15th International Symposium Boron, Borides and Related Compounds, held at Hamburg, Germany, Aug 21-26, 2005 Poster titled: "Physical properties of alkaline earth hexaborides".

13) M. Bauer, D. Fofanov, B. Albert, J. A. C. Broekaert, Participated in the Colloquium Analytische Atomspectroscopie, CANAS'05, held at Freiburg, Germany, March 6-10, 2005 Poster titled: "High-precision analysis of refractory materials by CCD-ICP-OES subsequent to microwave-assisted sample dissolution".

14) M. Bauer, M. Amberger, D. Fofanov, B. Albert, J. A. C. Broekaert, Participated in the Colloquium Spectroscopicum Internationale, CSI XXXIV, held at Antwerp, Belgium, Sept. 4-9, 2005 Poster titled: "Investigations on the improvement of precision and accuracy in ICP-OES for the analysis of advanced refractory materials".